Syntheses, Characterizations and Applications of Zinc Peroxide Nanoparticles

Von der Fakultät für Mathematik, Informatik und Naturwissenschaften der RWTH Aachen University zur Erlangung des akademischen Grades eines Doktors der Naturwissenschaften genehmigte Dissertation.

vorgelegt von

Master of Science

Christian Thomas Bergs

aus Aachen, Deutschland

Berichter: Universitätsprofessor Prof. Dr. Andrij Pich
Universitätsprofessor Prof. Dr. Lothar Elling

Tag der mündlichen Prüfung: 14.07.2017

The great tragedy of science:

The slaying of a beautiful hypothesis by an ugly fact.

Thomas Henry Huxley, 1870

The presented thesis was performed at the DWI-Leibniz Institute for Interactive Materials e.V. at the RWTH Aachen University. I hereby confirm that this thesis was self-penned and that no other sources and tools were used beside the stated ones. All quotations were marked and listed.

Aachen, 17.07.2017

I would like to thank Prof. Pich for the possibility of this work and the helpfulness in all matters. Additionally my thank goes to Prof. Elling and Prof. Albrecht for assuming the second and third report of this thesis.

My thanks goes also to all my colleagues and group members who made the four dissertation years always enriching, instructive and especially pleasant and funny.

Further I would like to thank Dr. Walter Tillmann for performing numerous FTIR and Raman measurements, Prof. Dan Demco for implementation of the ^{31}P solid state NMR measurements, Prof. Georg Conrads and his team for the development and execution of the antibacterial testing and Thomas Fischöder for performing the electrophoresis measurements. Further I especially thank Dennis Berg for performing the extrusion experiments, the viscosimetry and color measurements.

Additionally I have to thank all my bachelor and research students (Luc, Lisa, Hannah Andre, Pia, Christoph, Johannes and Klaus) who performed a big part of the practical work of this thesis.

I also want to thank my family and all my friends who supported me always and without hesitation.

And finally and mostly I want to thank Marina for just being there for me all the time.

Abbreviations

A	Hamaker constant
AAc	Acrylic acid
AAEM	Acetoacetoxyethyl methacrylate
ACMA	2, 2'-azobis(N-(2-carboxyethyl)-2-methyl-propionamidine)
AMPA	2, 2'-azobis(2-methylpropionamidine) dihydrochloride
AOT	Dioctyl sulfosuccinate
APM	Auxiliary processing module
ARS	Alizarin red S
β	Mass concentration
BMEP	Bis[2-(methacryloyloxy)ethyl] phosphate
BIS	N, N'-methylenebisacrylamide
c	Volume phase concentration
C_a	Capillary number
c_i	Diffusions boundary layer concentration
c*	Phase interface concentration
CHO	Chinese hamster ovary
D	Distance
DIN	German Industry Norm
DLVO	Derjaguin, Verwey, Landau and Overbeek theory
DNA	Desoxyribonucleic acid
DOX	Doxorubicin
Con A	Concanavalin A
CTAB	Hexadecyltrimethylammonium bromide
D_e	Deborah number
e	Electronic charge
E_e	Elasticity number
E. coli.	Escherichia coli
EDTA	Ethylene diaminetetraacetic acid
EP	Effex pumps
ε_r	Relative permittivity
ε_0	Vacuum permittivity
FA	Fumaric acid

FESEM	Field Emission Scanning Electron Microscopy
FFT	Fast Fourier Transformation
FTIR	Fourier transform infrared spectroscopy
FWHM	Full width at half maximum
G_r	Grashof number
Glc-1P	Glucose-1-phosphate
h	Height
HEPES	4-(2-hydroxyethyl)-1-piperazineethanesulfonic acid
HFIP	1,1,1,3,3,3-hexafluoropropane-2-ol
HR-TEM	High resolution transmission electron microscopy
ICP-OES	Inductively coupled plasma atom emission spectroscopy
IUPAC	International Union of Pure and Applied Chemistry
K^{-1}	Debye screening length
k_B	Boltzmann constant
LCAO	Linear combination of atomic orbitals
LCST	Lower critical solution temperature
l	Length
L_0	Length scale
MAA	Methacrylic acid
MAS	Magic angle spinning
MIC	Minimum inhibitory concentration
mM	Millimol
MRT	Microfluidic Reaction Technology
NADPH	Nicotinamide adenine dinucleotide phosphate
η	Viscosity
η_0	Characteristic viscosity
η_{inh}	Inherent viscosity
η_{rel}	Relative viscosity
Θ	Diffraction angle
OGM	Octaethylene glycol monododecyl
o-PEA	*o*-phosphoryl etanol amine
^{31}P-NMR	31-phosporous nuclear magnetic resonance
PABA	4-amino-benzoeic acid
PAPA	4-amino-phtalic acid

P_e	Péclet number
PEG 200	Polyethylene glycol 200
PEGMA	Poly(ethylenglycol)-methylethermethacrylate
PET	Poly(ethylene terephthalate)
PDI	Polydispersity index
PBS	Phosphate-buffered saline
PIP3	Phosphatidylinositol-3,4,5-triphospate
PMEA	Poly(2-methoxyethyl acrylate)
PNIPAm	Poly(N-isopropylacrylamide)
PVC	Polyvinyl chloride
PVCL	Poly(N-vinylcaprolactam)
r	Radius
R_a	Rayleigh number
R_e	Reynolds number
r_H	Hydrodynamic radius
rhGH	Recombinant human growth hormone
ROS	Reactive oxygen species
r-PET	recycled Poly(ethylene terephthalate)
S. aureus	Staphylococcus aureus
SDS	Sodium dodecyl sulfate
SSP	Solid-state polycondensation process
Suma	N-succinimidyl methacrylate
t	PET solution flow time
t_0	Solvent flow time
T	Temperature
TEM	Transmission electron microscopy
TGA	Thermogravimetric analysis
TGA-MS	Thermogravimetry combined spectroscopy
Tween 20	Polysorbate 20
THF	Tetrahydrofurane
U_0	Flow velocity
UDP-Glc	Uridine 5'-diphosphoglucose
UV	Ultraviolett
V_a	Attractive forces

VAA	Vinylacetic acid
VCL	N-vinylcaprolactam
VIm	Vinylimidazole
VPPT	Volume phase transition temperature
V_r	Repulsive forces
V_t	Total potential energy
w	Width
W_i	Weissenberg number
XNBR	Carboxylated nitrile butadiene rubber
XRD	X-Ray diffraction
y	Surface potential
Z	Charge number
λ	Wavelength
ρ	Density
ξ	Zeta potential

1 Aim and Motivation

The aim of this Thesis was the synthesis, characterization and application of small and uniform zinc peroxide (ZnO_2) nanoparticles. Common zinc peroxide synthesis approaches are precipitation reactions, laser ablation methods, hydrothermal processes and sol-gel syntheses. However all these synthesis methods led to aggregation of the nanoparticles resulting in high polydispersities and non uniform products. Therefore a new synthesis pathway had to be established. A high pressure impinging jet reactor (Microfluidizer, Microfluidics©) was used for the synthesis of zinc peroxide nanoparticles for the first time. The device is capable of generating high process pressures (up to 1400 bar) and high shear forces (up to $7 \cdot 10^6$ s^{-1}) which guaranteed small and uniform nanoparticles.

Furthermore several stabilizer agents (BMEP, *o*-PEA, citrate, Glc-1P, UDP-Glc and AOT) were used to increase the nanoparticle stability even further and to introduce new functionalities to the zinc peroxide nanoparticle surface. Phosphates, carboxylates and sulfonates with different additional functional groups were applied for the nanoparticle syntheses. Thereby the phosphate, carboxylate and sulfonate groups interacted with the nanoparticle surface while the remaining groups (amides, methacrylates, glucose rings and carboxylates) introduced new functionalities and were accessible for further modifications (Figure 1.1).

Additionally the promising oxygen release properties of the synthesized nanoparticles were intensively investigated. It was proven that the oxygen release could be triggered through elevated temperatures (>190.0 °C, dry state) or decreased pH values (<7.5, aqueous phase). This property makes the zinc peroxide nanoparticles suitable for applications like polymer bleaching or as antibacterial agent. For example are new bleaching agents needed for the recycling of poly(ethylene terephthalate) (PET). A discoloration (greying) of the PET occurs during the recycling process (T = 290.0 °C) caused through the formation of elementary antimony. Zinc peroxide nanoparticles present in the PET melt can oxidize the antimony through released oxygen and act simultaneously as white pigments which both increases the whitening of the polymer. Furthermore the pH induced oxygen release allows the use of the synthesized nanoparticles in biological systems. Oxygen can act as an antibacterial agent against bacteria like *aggregatibacter actinomycetemcomitans* or *prevotella*

intermedia which makes the zinc peroxide nanoparticles suitable for antibacterial wound dressings or the protective coating of implants, teeth or catheters.

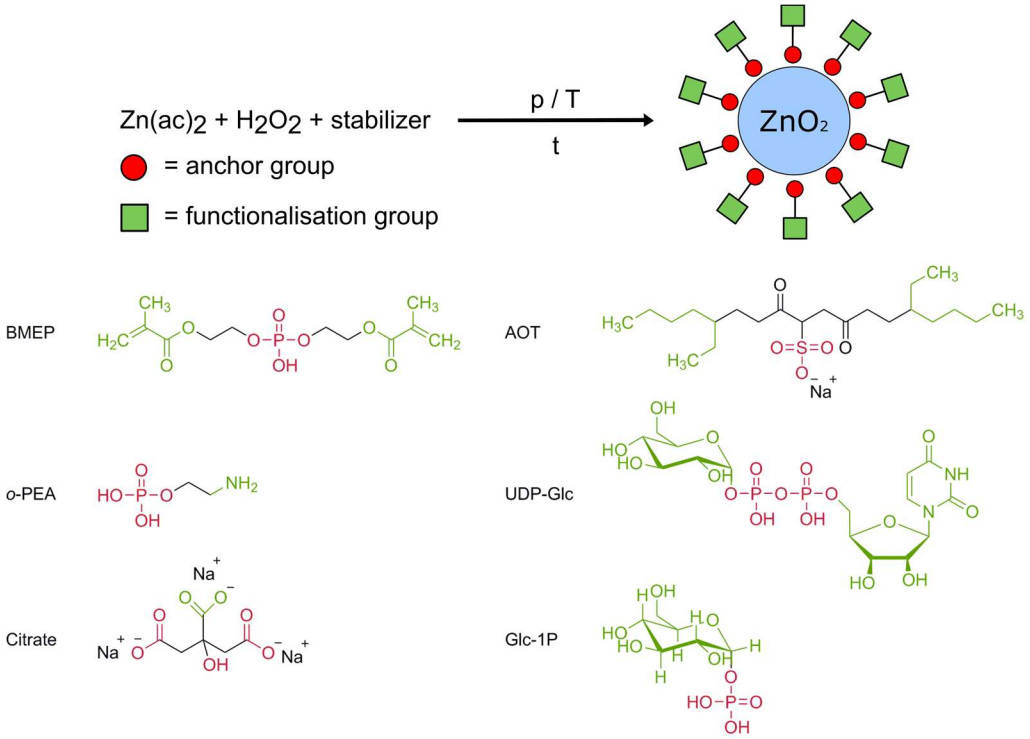

Figure 1.1: *Schematic illustration of the zinc peroxide nanoparticle synthesis approach with the different stabilizer molecules BMEP, o-PEA, Citrate, Glc-1P, UDP-Glc and AOT (anchor groups: Phosphate, carboxylate and sulfonate functions of the corresponding stabilizer molecules).*

The immobilization of zinc peroxide nanoparticles onto such scaffolds or implants can be facilitated through nanoparticle incorporation into polymeric structures like microgels. Therefore a proof of principle procedure was introduced for the incorporation of different functionalized nanoparticles into PCVL and PNIPAm based microgels.

2 Synthesis of Zinc Peroxide Nanoparticles

2.1 Introduction

2.1.1 Nanoparticles and their Applications

The prefix “nano” originates from the greek word “*nános*” for dwarf and describes orders of magnitude of 10^{-9}.[1] According to the definition of the International Union of Pure and Applied Chemistry (IUPAC) nanomaterials and nanoparticles must at least possess one nanoscale dimension to be called “nano”.[2] Those objects can be distinguished into nanoparticles (three nanoscale dimensions), nanofibres (two nanoscale dimensions) and nanoplatelets (one nanoscale dimension), while the nanoscale dimensions are normally in a range between 1 and 100 nm.[3,4]

The generation of new and unique properties by reducing the size of well known bulk materials made the nanomaterials highly interesting and valuable for research and industry in the last years. For example 1000 to 2000 tons nanomaterials were produced in 2004 while already 9600 tons nanomaterials (including only the 10 most used nanomaterials) were produced in 2012. Experts even predict an increase to 58000 tons in 2020 and valued the volume of the global nanotechnology market to 2.5 trillion US-$ in 2015.[5–8] Hereby the most common nanomaterials are metal oxide nanoparticles or silver and carbon based nanoparticles.[9]

The dimensional reductions cause a significant change of the behavior and the properties of the nanomaterials compared to their bulk equivalents. For example the ratio between surface atoms and core atoms increases drastically when the size of a nano object undergoes a certain limit. Thereby the contribution of the surface energy to the total energy of the object increases strongly which influences several properties like for example the melting point. The melting point becomes size dependent and is no longer a material constant as for bulk materials. A classical example for this phenomena is the decrease of the melting point of gold from 1336 K in the bulk phase to 600 K for gold nanoparticles with a diameter of approximately 20 Å.[10] Also the reactivity of the nanomaterials is influenced positively through the increased surface atoms. More surface atoms cause more accessible centers which could increase for example the catalytic activity of nanomaterials.[1,11] An example are cerium dioxide nanoparticles supported on aluminium oxide in exhaust gas catalytic

converters. It is cheaper than platinum and can still oxidize carbon monoxide to carbon dioxide or reduce NO_x in a redox reaction.[12]

Beside the changes in the surface to volume ratio also the number of atom orbitals of nanomaterials becomes finite. Through this change the properties of conducting and semi conducting materials like color or electronic conductivity become size dependent. This dependence can be explained via the “linear combination of atomic orbitals” model (LCAO). It is assumed that an infinite crystal structure is present in bulk materials and that all atomic orbitals can be summed up to bands (valence and conduction band) through their linear combination. Electrons can be excited via irradiation or temperature and be elevated from the valance band to the conduction band. Simultaneously a positively charged electron hole is formed in the valance band. The movement of these two species then causes the conductivity of the material. Contrary the formation of discrete energy levels for nanomaterials limits the excitation of the electrons and induces more specific properties. The energy levels become discrete when the size of the nanomaterial is nearly the same or smaller than the size of the charge carriers (electrons and electron holes). Therefore, the electron hole pairs have to reduce their size to still fit inside the nanomaterial. This phenomena is called the quantum size effect or quantum confinement and leads beside the formation of discrete energy levels also to an increase of the energy barrier.[13,14] One major advantage of this molecular electronic structure is the switchability of the light absorption through the sizes of the nanoparticles. For example this effect is being leveraged for the calibration of photoacoustic imaging. A laser diode system with wavelength between 650 nm and 905 nm was calibrated using gold nanoparticles with different sizes from 1 nm to 85 nm.[15] Another light dependent application is the use of titanium oxide and zinc oxide in sunblockers. The size of the nanoparticles is tuned in the way that they absorb the UV spectrum of the sun light which causes the UV protection of the sunblockers.[1,5]

For example showed metallic nanoparticles an increase in toughness and stiffness compared to their bulk compounds. The increase could be explained through the limitation of the dislocation motion influenced through the nanoparticle size.[1,16] This property is for example useful for the automobile industry. New composite materials including nanoparticles were developed for bumpers resulting in enhanced mechanical properties.[17]

Also ferromagnetic nanoparticles with superparamagnetic properties could be synthesized. The diameter of these nanoparticles should be smaller than the size of their Weiss'sche domains which are small domains (10-100 nm) in which all atomic dipols have the same orientation. A dipolarity could be introduced to the particles by this size limitation resulting in an alignment of the nanoparticles in an external magnetic field. Such particles are for example used for ferrofluids which are utilized for speaker cooling systems or the low-friction sealing of rotary arbors. A future application could be the magnetic hyperthermy therapy against cancer.[1,18]

2.1.2 Common Nanoparticle Synthesis Approaches

Nanoparticles can be synthesized generally in two different ways. Via a top-down or bottom-up approach. Top-down approaches are accomplished through mechanical crushing of macroscopic materials down to a specific scale while bottom-up methods form colloidal structures starting from the molecular level.

High energy ball mills are normally used for the mechanical crushing processes (top-down). These processes are fast, cost-efficient and allow the conversion of bigger sample amounts. The used grinding balls can for example consist of high density steel or tungsten carbide which both provide a very high toughness which ensures the grinding of many different materials. Nevertheless a contamination of the resulting products can always occur through abrasive effects on the grinding balls. Additionally a precise control of the nanoparticle sizes and uniformity is difficult to achieve which makes this method unsuitable for the synthesis of very small and uniform nanoparticles.[19–21]

Contrary bottom-up methods provide an excellent control over the nanoparticle sizes and their uniformity via a controlled growth from the molecular level. The control can be achieved through different parameters like temperature, pH value, educt concentration and process management and the particles are formed by chemical reactions and physical bonding forces. Bottom-up methods can be distinguished into gas phase and liquid phase reactions (Figure 2.1.1).

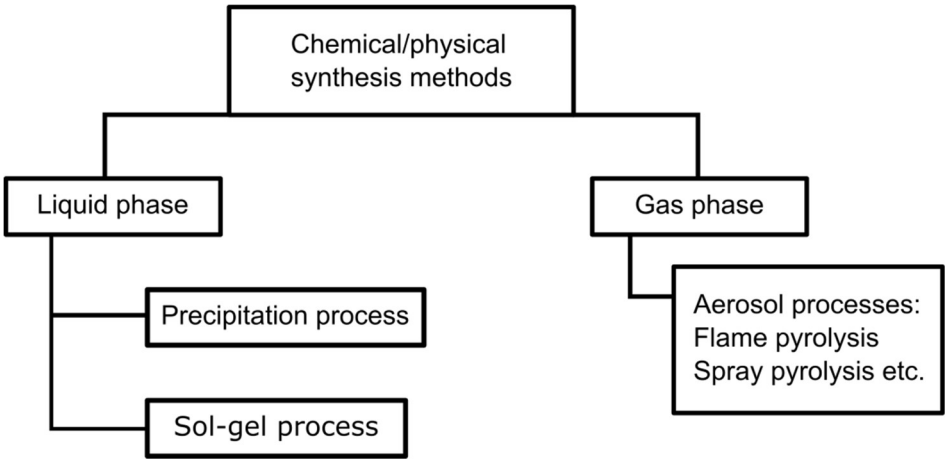

Figure 2.1.1: *Schematic illustration of the different bottom up synthesis approaches for nanoparticles.*[20]

Gas phase reactions start with the formation of an aerosol which can either consist of solid precursor particles or liquid droplets which are dispersed in the gas phase. The particle growth can take place through condensation, coagulation or coalescence and the most reactions are thermodynamically controlled due to the high reaction temperatures (>500 °C).[20–22] Common gas phase reactions are performed in flame-, plasma- or hot wall reactors or take place in inert gas condensation processes or overcritical expansion reactions. One of the most common synthesis approaches is the flame reactor. A sublimator or evaporator produces the educt aerosol which then is procured to the flame (inside the reaction chamber) via a dry carrier gas. The gaseous combustibles like hydrogen or methane and air or pure oxygen are introduced via the burner itself into the reaction chamber. The thermal energy of the flame then induces the coagulation or sintering of the educts resulting in the desired product. The reaction is completed when the flame temperature reached a critical minimum which does not suffice to initiate further reactions or when the particle collision became negligible caused through a significantly decreased particle concentration. Especially the flame temperature and the delay time give control over the product and it's properties like size an morphology. This synthesis approach is mostly used for the synthesis of metal oxide nanoparticles, but it is also possible to use reducing flames to obtain non-oxide or metallic nanoparticles.[23,24]

Liquid phase reactions can be performed at much lower reaction temperatures compared to the gas phase reactions and allow a more precise control over the particle sizes and morphologies. The control can be achieved through immediate stabilization of the particles during the synthesis or through a precise reaction

management. The two most common liquid phase synthesis approaches are the sol-gel reaction and the precipitation reaction. Sol-gel reactions are mostly used for the synthesis of porous nanomaterials like ceramic nanostructured polymers and precipitation reactions are most suitable for the synthesis of very small (few nanometers) nanoparticles.[25,26]

Depending on the reaction conditions a sol (dispersion of small solid particles) or a gel can be formed during a sol-gel synthesis. The reaction takes place through the hydrolysis and/or condensation of the used precursor and can be controlled by the ratio of these two mechanisms. If the hydrolysis rate is higher than the condensation rate a polymer network is formed, while a sol can be synthesized when the condensation rate is higher than the hydrolysis rate (Figure 2.1.2).

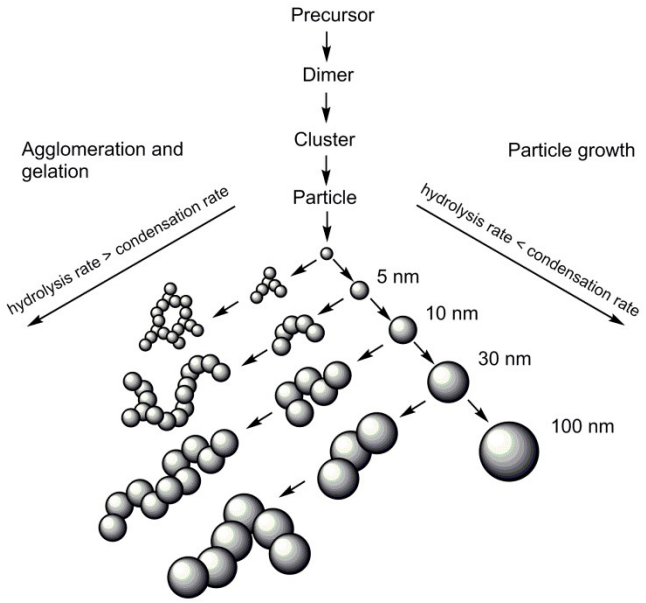

Figure 2.1.2: *Schematic illustration of the sol-gel process; for the formation of a gel (left) and the formation of a sol (right).*[27]

Which reaction rate is higher can be controlled through parameters like temperature, concentration of the reaction solution, type and amount of catalyst (bases or acids) or the used reactor. Mostly water is used as the reaction media, but organic solvents are also applicable. Typical precursors for a sol-gel synthesis are inorganic metal salts (chlorides, nitrates, sulfates etc.) or alkoxides of for example silicon, titanium or aluminium. However alkoxides are used more often due their more predictable reactivity. The use of inorganic metal salts often leads to the formation of different oligomers which causes the formation of different counter ions. These can complex the metal ions leading to a non-predictable reactivity. Contrary alkoxides react with

water molecules under elimination of the alkoxide group (-OR) forming alcohols and metal hydroxides. A combination of two hydroxides then leads to the formation of M-O-M bonds under water elimination.[27–29]

One of the disadvantages of the sol-gel synthesis is the precise adjustment of the reaction rates of the hydrolysis and the condensation. Most of the transition metal precursor possess a to high reaction rate which prevents the adjustment of the particle sizes and morphologies. Additionally the reactiveness of different metal alkoxide can differ strongly which complicates the synthesis of more complex multioxide compounds. A great advantage of this method is the possible synthesis of composite materials through filling of the porous structures during the gel formation or the loading with drugs enabled through the low synthesis temperatures.[29,30]

The precipitation reaction is the second main liquid phase approach for the synthesis of nanomaterials. Normally metal salts are dissolved in aqueous or organic media and are precipitated by adding a corresponding agent. After addition of the precipitating agent the desired product enriches in the mixture until the equilibrium solubility is exceeded and a supersaturated solution is formed which induces the nucleation. Two different types of nucleation are possible. The heterogeneous nucleation takes place on solid surfaces for example on flask or reactor walls while the homogeneous nucleation takes place in solution. For a homogeneous nucleation it is necessary that enough elementary blocks with sufficient kinetic energy are present in the reaction media thereby that three blocks can collide with each other. During this process one of the shock-partners absorbs most of the kinetic energy of all three shock-partners while the remaining two start the nucleation (Figure 2.1.3).

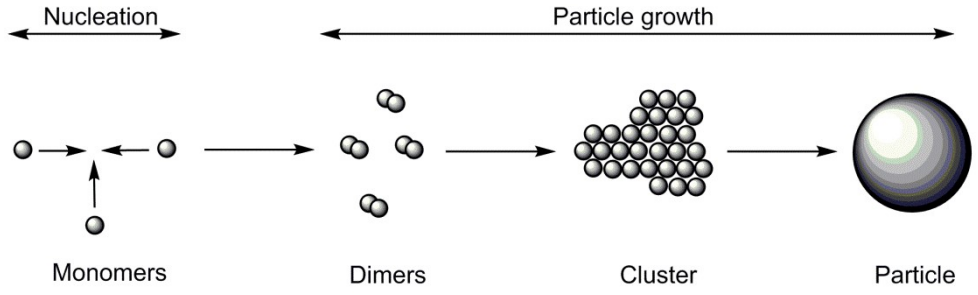

Figure 2.1.3: *Schematic illustration of the nucleation and particle growth during homogeneous particle formation.*

The probability for the collision of three elementary blocks increases with increasing supersaturation of the reaction medium. Additionally smaller particles are formed at

higher supersaturations due to the disproportional increase of the seed formation velocity compared to the growth velocity of the particles. The formed seed particle grows through diffusion, Ostwald ripening or aggregation/agglomeration which can be controlled through the educt concentration, pH value or the reaction temperature.[31,32] The growth through diffusion takes place in three steps:

- Convective transport of educt molecules to the diffusion boundary layer of the particle (laminar or turbulent)
- Diffusion step: Volume diffusion of the molecules through the diffusion boundary layer to the phase interface of the particle
- Incorporation step: Incorporation of the molecules onto the particle surface inside the phase interface

The growth of the particles is diffusion- or incorporation-limited depending on which of the last two steps is the more slowly one. If the growth of the particles is diffusion-limited then the concentration gradient inside the diffusion boundary layer between the volume phase and the phase interface ($c-c_i$) is much higher than the concentration gradient between the phase interface and the particle surface (c_i-c^*). Contrary for the incorporation-limited particle growth the concentration gradient inside the phase interface is much more higher than the concentration gradient inside the diffusion boundary layer ($c_i-c^* >> c-c_i$) (Figure 2.1.4).[33]

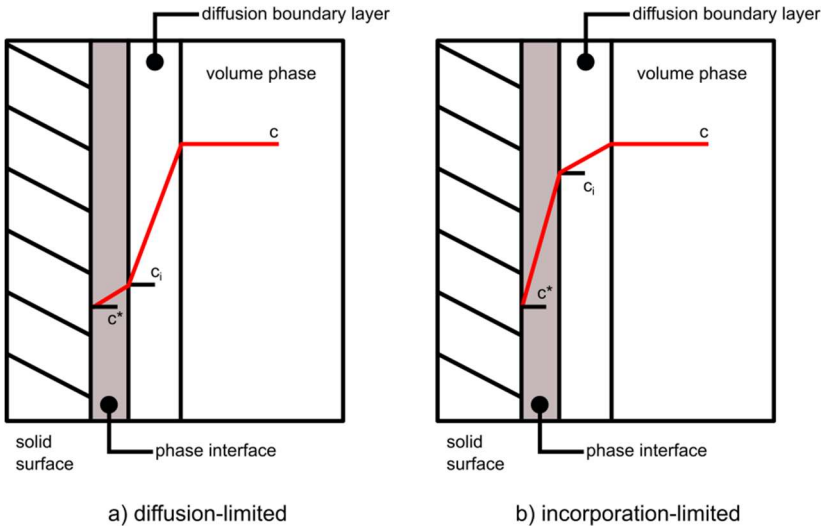

Figure 2.1.4: *Schematic illustration of the two different growth limitation processes during nanoparticle formation.*[33]

The growth through Ostwald ripening takes place through the dissolution of smaller particles and the simultaneously growth of bigger particles. New particle seeds are

formed when the critical supersaturation of the reaction solution is reached. At this state the solubility of even the smallest particles is extremely low causing their dispersion stability. But the supersaturation decreases with increasing reaction time due to the conversion of the used educts which causes an increase of the solubility of the smaller particles. This process continues until only bigger particles with an equally solubility are present in the reaction solution.[33]

The occurrence of aggregation/agglomeration is in most cases undesirable. The particle growth through this micro processes are uncontrollable and are caused mostly through van-der-Waals attractions between particles. This attractions can be prevented through different stabilization methods which are discussed in detail in section 2.1.3.

Precipitation reactions are mostly used for the synthesis of metal oxide, non oxide or metallic nanoparticles but also more special compounds like multi-metal nanoparticles can be synthesized through co-precipitations.[31,34]

2.1.3 Methods of Nanoparticle Stabilization in Solution

Aggregation and agglomeration are micro processes which can always occur during the synthesis of nanoparticles and have a significant influence on the morphology and properties of the particles. These processes emerge due to the free surface energy reduction during the formation of bigger particles and clusters from smaller particles. Aggregation describes the collision of two or more separate particles and the subsequent formation of a solid cluster which can’t be separated anymore. Contrary agglomerates are loosely clusters which consists of separate particles held together mostly by van-der-Waals interactions. This means that aggregation is an irreversible process while the agglomeration is reversible.[35] The two processes are initiated through mechanical transport mechanisms (diffusion, flow controlled transport), followed by particle-particle collision and the adhesion of the particles. The adhesion takes place through the formation of crystalline bridges between the particles induced through molecular kinetic processes. The aggregation/agglomeration can be distinguished into the peri-kinetic (diffusion controlled) and the ortho-kinetic (convection controlled) aggregation/agglomeration depending on the nature of the particle collision.

The aggregation/agglomeration velocity of the peri-kinetic mechanism is determined by the rate and intensity of the collisions influenced through the Brownian molecular motion (collision probability) and the adhesion probability of two particles. In contrast the ortho-kinetic aggregation/agglomeration arises through the hydrodynamic motion caused through external forces like convection or sedimentation.[33]

Therefore nanoparticles have to be stabilized to prevent aggregation/agglomeration. The stabilization can be achieved through electrostatic stabilization, introducing of surface active substances (surfactants/stabilizer) or the incorporation in polymeric structures for example microgels (Figure 2.1.5).

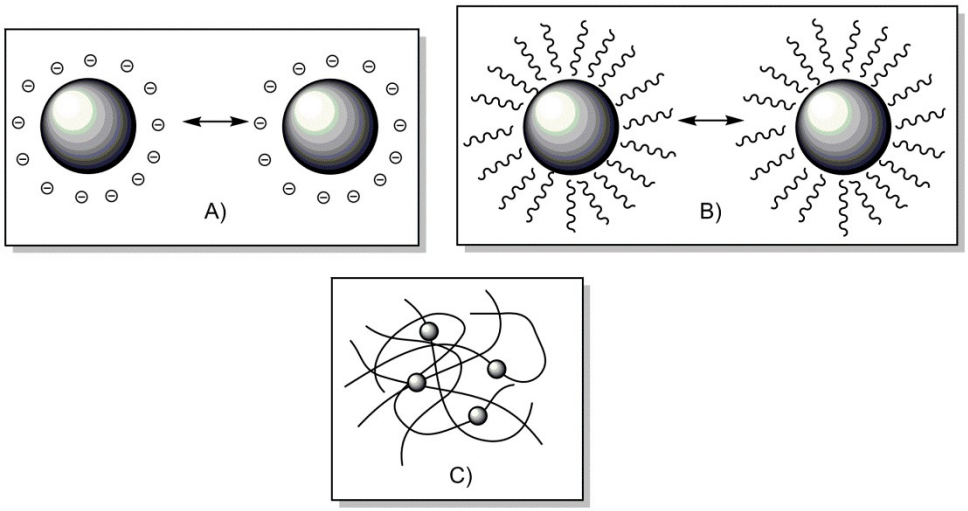

Figure 2.1.5: *Schematic illustration of the different nanoparticle stabilizing methods: electrostatic stabilization (a); steric stabilization (b); incorporation in polymeric structures (c).*

The electrostatic stabilization of nanoparticles is based on the repulsion of equally charged particles. The DLVO theory named after Derjaguin, Verwey, Landau and Overbeek describes the behavior of particles in solution considering attractive (V_a) and repulsive (V_r) forces which add up to the total potential energy (V_t) of the particles as a function for the stability of the particles:

$$V_t = V_a + V_r \qquad [1]$$

The attracting forces are predominantly determined by-van-der-Waals interactions depending on the distance (D) of the particles. The function can be simplified by the Derjaguin approximation and the introduction of the Hamaker constant (A) to give:

$$V_a(D) = -\frac{A}{12\,\pi\,D^2} \qquad [2]$$

The counterforces which cause the repulsion are composed of several effects but can be mainly attributed to the formation of a charge double layer around the particles and the according Coulomb interactions, respectively (Figure 2.1.6).

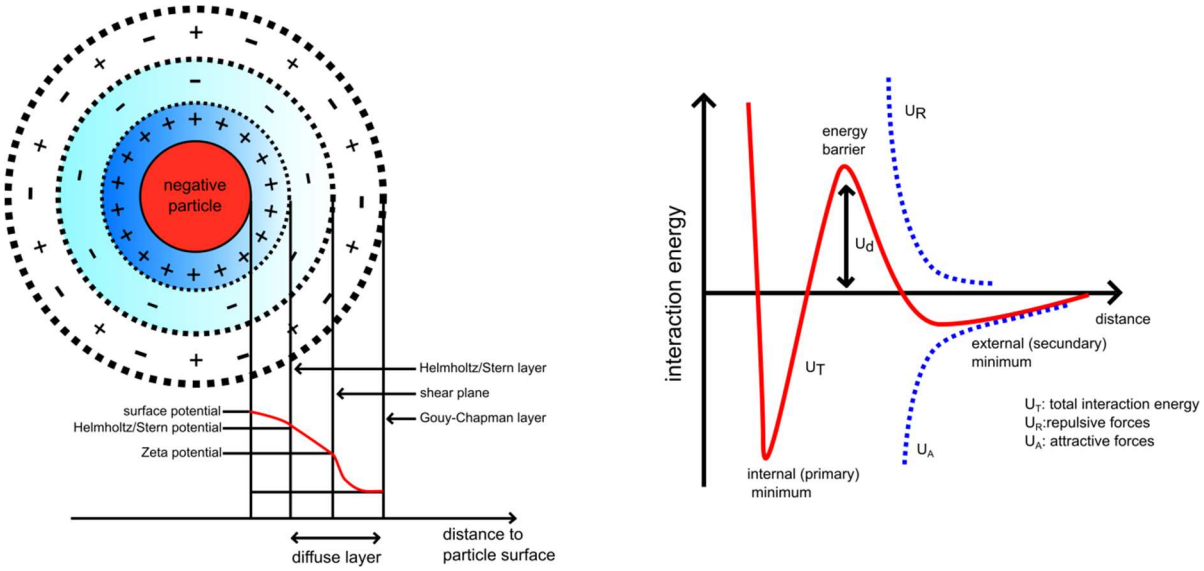

Figure 2.1.6: *Schematic illustration of the electrostatic stabilization of a nanoparticle through formation of charge double layer (left); illustration of the formation of an energy barrier causing the electrostatic stabilization.*[36]

Due to the charged particle surface in a solution, counterions adsorb strongly at the surface forming the Helmholtz layer. With increasing distance (D) further ions with opposite charge are attracted and the layer of surrounding ions becomes more diffuse resulting in an exponential decrease in the surface potential (Gouy-Chapman layer). Furthermore the Debye-Hückel model for counterion clouds is used for the description of ion distribution as well as the Poisson-Boltzmann equation for the electrostatic interaction in those solutions. By scaling the thickness of the double layer with the Debye screening length (κ^{-1}) and considering the reduced surface potential (γ) it is possible to obtain the potential energy of repulsion for two colloidal spheres by integration of all surface elements of the particles:

$$V_r(D) = 32\pi\varepsilon_r\varepsilon_0\left(\frac{k_BT}{ze}\right)^2 \cdot y \cdot e^{(-kD)} \qquad [3]$$

Whereas ε_r stands for the relative permittivity and ε_0 for the vacuum permittivity. k_B is the Boltzmann constant, T is the temperature, z is the charge number and e is the electronic charge originating from the Poisson-Boltzmann equation.[37]

To achieve a sufficient electrostatic stabilization of nanoparticles the repulsive forces have to be bigger than the attractive ones. High repulsive forces can for example be

generated through highly dense charge double layers inducing a strong energy barrier between two particles (Figure 2.1.6). Without an energy barrier every collision of two particles results in the formation of a bigger particle or cluster. In this case the aggregation velocity depends only on the diffusion velocity, the nature of the mixing (turbulent or laminar) and the interaction intensity. When an energy barrier is present the energy of the particles must be sufficiently high to overcome the barrier. This process is comparable to a bimolecular reaction in which an activation energy is needed and two different events can take place. If the kinetic energy and the attractive forces of the colliding particles are not high enough then the particles can not agglomerate and a stable dispersion is formed but aggregation can occur when the kinetic energy/attractive forces are sufficient.[38]

Alternatively nanoparticles can be sterically stabilized through the immobilization of stabilizer molecules like surfactants or functional polymers. These stabilizers have to possess a high affinity to the surface of the chosen nanoparticle and must provide good interaction properties with the chosen reaction medium. The steric stabilization is achieved by depletion forces and disjoining pressures that occur when the stabilizer corona of two particles overlap. The higher concentration of stabilizer in the overlapping region lowers the degrees of freedom of the stabilizers. The entropy is being decreased which is energetically unfavorable and leads to particle separation. Additionally, a concentration gradient is being formed by the overlap to the rest of the solution and thus an osmotic pressure occurs to diminish the imbalance and segregates the particles further.[39] The stabilizing agents additionally introduce new functionalities to the nanoparticle surface. Especially surfactants and smaller functional molecules which consist of head and tail proved to be very versatile. Normally the head of such compounds interacts with the nanoparticle surface while the tail is responsible for the interaction with the reaction media and thus for the stabilization of the particles. This sequential structure enables the tailoring of the stabilizer properties depending on which nanoparticle system has to be used. For example common stabilizers for metal and metal oxide nanoparticles are thiols, carboxylic acids, amines, phosphates and silanes. Previous studies showed that such compounds formed mono-, bi- or tridentate bonds depending on nature of the nanoparticle surface.[40] Especially phosphate functionalized stabilizer showed a superior affinity to metal oxide nanoparticles compared to carboxylic acids or amines (Figure 2.1.7). It could be shown that phosphates only formed bonds with

nanoparticle surface functions such as hydroxides and did not form any homo-condensates through P-O-P linking. Phosphates are additionally capable of forming up to three particle-O-P bonds via their three oxygen functions located on the phosphorous atom. Previous investigations showed for example that during the stabilization of titanium oxide or tin oxide nanoparticles covalent and bi- or trident bonds were formed resulting in stable nanoparticle dispersions.[41,42]

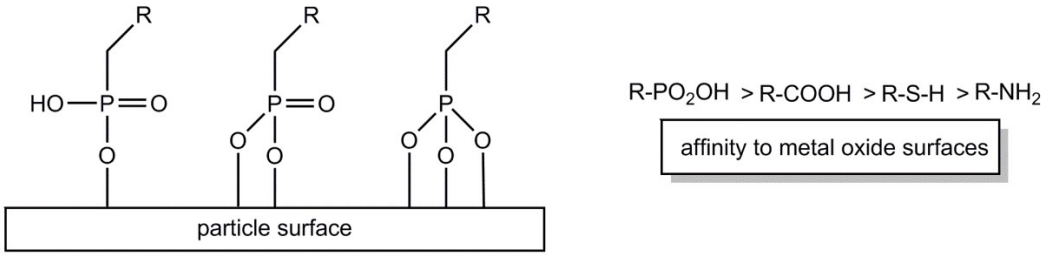

Figure 2.1.7: *Schematic illustration of the different binding types of phosphate stabilizers to metal oxide surfaces (left); affinities of different chemical groups to metal oxide surfaces (right).*[40]

Also the incorporation of nanoparticles in polymeric structures showed good stabilizations. Hereby the good stabilization properties are caused through the high amount of functionalities within a polymer. Especially the use of amphiphilic polymers proved to be successful. For example poly(acrylic acid) modified with aliphatic amines was used for the stabilization of quantum dots. It could be shown that the obtained solid after evaporation could be redispersed in aqueous media or organic solvents yielding stable and single nanoparticles. In order to increase the stability of the particles further a cross-linking reaction with lysine was also performed.[43,44] The incorporation of nanoparticles into microgels caused not only their stabilization but led also to the formation of interesting composite materials. Due to their pH- and temperature responsive properties are microgels possible candidates for carrier and drug delivery systems. For example were LaF_3:Eu nanoparticles immobilized in VCL/AAEM microgels via methacrylate functions present on the nanoparticle surface. The nanoparticles were first functionalized with the methacrylate containing stabilizer and subsequently incorporated into the microgels via radical polymerization. The nanoparticles acted simultaneously as crosslinking agent which made the adjustment of the microgel size depending on the nanoparticle amount possible.[45]

2.1.4 State of the Art Syntheses of Zinc Peroxide Nanoparticles*

This study focused on the synthesis, characterization and application of zinc peroxide nanoparticles. A completely new, fast and reproducible synthesis approach was developed (see section 2.1.5) but according to the literature many different synthesis approaches were already established.

For example Bai et al. synthesized ZnO_2 nanoparticles via a green hydrothermal method in aqueous solution in a Teflon-lined stainless steel autoclave using only ZnO powder and a 30 % H_2O_2 solution as starting material. They obtained particles with an average diameter of 12 nm, calculated through the Debye-Scherrer equation and observed that the reaction temperature (80 to 140 °C) was crucial for obtaining pure cubic phase nanoparticles.[46]

In contrast to that, the synthesis via laser ablation was done by Drmosh et al. The nanoparticles were obtained through the irradiation of a Zn plate through a Nd-YAG laser, with a wavelength of 355 nm, which resulted in nanoparticle diameter of 3 to 4 nm, again calculated through the Debye-Scherrer equation. They used different surfactants like SDS, CTAB and OGM and investigated their influence on the particle size and morphology. They observed that only SDS adsorbed on the particle surface and concluded that the high critical micelle concentration was responsible for the immobilisation of the SDS.[47]

A sol gel synthesis was developed by Sun et al., which used a 35W Xenon lamp to initiate the formation of ZnO_2 starting with zinc acetate dihydrate and 30 % hydrogen peroxide dissolved in water. This lamp had a similar energy distribution compared to normal sunlight, which was needed to transform the precursor zinc acetate to zinc peroxide. The solution was irradiated for 6h under continuous stirring to obtain a ZnO_2 precursor sol (average particle size: 68.0 nm). After two days aging this sol had to be baked at 40 °C overnight which resulted after crushing in a fine ZnO_2 powder. It was possible to change the obtained product to a sol or gel depending on reaction parameters like temperature and reaction time. Additionally they observed that with increasing sintering temperature (over 200°C) the zinc peroxide was transformed into pure zinc oxide with high crystallinity.[48]

Chen et al. synthesized zinc peroxide nanoparticles by an organometallic precursor method. They used as educt $ZnCl_2$ which was dissolved in THF containing

$Mg(C_6H_{11})Cl$ and 1-octylamine. This solution was heated to 323 K for 48 h followed by adding H_2O_2 to disperse the precipitate. The obtained solid was separated by centrifugation and dried at room temperature. The obtained particle size was found to be 3.1 nm calculated by Scherrer equation but only one HR-TEM image was provided to proof this calculation.[49]

Rosenthal-Toib et al. were able to generate zinc peroxide nanoparticles by a simple oxidation-hydrolysis-precipitation procedure. They used zinc acetate as precursor, hydrogen peroxide as oxidizer and water as solvent and hydrolysis source. Additionally, the surfactant polyethylene glycol 200 (PEG 200) was used in order to stabilize the nanoparticles. The reaction was simply carried out under continuous stirring in a glass beaker at room temperature for two hours. Sodium hydroxide was added to the resulting clear and colourless to yellowish solution, which resulted in precipitation of the zinc peroxide. They observed that the content of PEG 200 influenced the size of the particles significantly varying the sizes from 193 to 19 nm. Nevertheless the TEM images showed big aggregates indicating a lack of nanoparticle stability.[50]

Another simple and green synthesis method was established by Yang et al. They used hydrozincite ($Zn_5(CO_3)_2(OH)_6$) powder as precursor which was oxidized with a 30 wt% hydrogen peroxide solution. The reaction was carried out in water in a closed conical flask for 24 to 72 hours and the formed precipitate was separated by centrifugation. The particles sizes were calculated to be 3.1 to 4.2 nm (Scherrer equation) but TEM images showed mostly aggregates. They observed that their reaction conditions only worked with the used precursor. Experiments done with zinc oxide as precursor did not lead to zinc peroxide particles.[51]

All these different synthesis approaches led to the formation of zinc peroxide particles but the determination of the particle sizes was mostly done by calculation of the crystallite sizes vie the Debye-Scherrer equation. Microscopy investigations like TEM and FESEM measurements showed clusters and bigger particles indicating the occurrence of aggregation/agglomeration caused through an insufficient stabilization. These drawbacks were overcome with the newly introduced synthesis method.

2.1.5 Microfluidic Reaction Technology (MRT)

The previous synthesis examples proved that common synthesis strategies only led to polydisperse and aggregated nanoparticles. Therefore a new synthesis strategy was developed during this study. A microfluidizer MRT CR5 from Microfluidics© was used for the synthesis of zinc peroxide nanoparticles. This device combines the advantages of a micro reactor with very high shear and impact forces and turbulent mixings.

Normally micro reactors consist of rectangular or cylindrical micro channels with diameter below 100 µm (Figure 2.1.8).

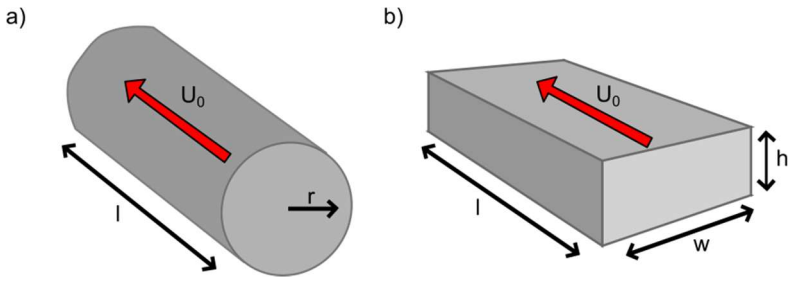

Figure 2.1.8: *Illustration of the two different types of micro channels: cylindrical (a) and rectangular (b) with flow velocity U_0 and the and the dimensional units r, l, w and h.*[52]

Through this dimensional reduction of reactors to the micro scale a dramatically change of the fundamental fluid physics can be achieved. For example becomes the mass transport inside normal microfluidic devices dependent on the viscous dissipation instead of inertial effects. To understand the different behavior of fluids in micro reactors several dimensionless number were introduced. The Reynolds number R_e, relating inertial forces to viscous forces; the Péclet number P_e, relating convection to diffusion; the capillary number C_a, relating viscous forces to surface tension; the Deborah, Weissenberg, and elasticity numbers D_e, W_i, and E_l, expressing elastic effects; the Grashof and Rayleigh numbers G_r and R_a, relating transport mechanisms in buoyancy-driven flows; and the Knudsen number K_n, relating microscopic to macroscopic length scales. Especially the Reynolds number is important for standard reactors but becomes nearly irrelevant for normal micro reactors. It describes the flow nature (turbulent/laminar) of fluids inside reactors in dependence on the flow velocity (U_0), the characteristic viscosity (η) and density (ρ) of the used fluid and a typical length scale (L_0):

$$R_e = \frac{U_0 L_0 \rho}{\eta} \qquad [4]$$

Due to the small diameter of common micro reactors only laminar flows can be achieved resulting in small Reynolds numbers. With water as the typical working fluid, flow velocities between 1 µm/s and 1 cm/s and typical channel radii of 1-100 µm, Reynolds numbers between 10^{-6} and 10 can be calculated. These low values of R_e affirm that viscous forces typically overwhelm inertial forces leading to laminar and predictable Stokes flows. To obtain turbulent mixings and by that more efficient reactions, the Reynolds number should be in a range of at least 2000 and 3000. Higher Reynolds numbers could be achieved though the increase of the flow velocity or through a change in the micro reactor architecture. For example in flow through a cylindrical channel that is curved with radius of curvature R much larger then the channel radius r, centrifugal forces on the fluid induce a secondary flow. This secondary flow causes an inhomogeneous flow resulting in a more turbulent mixing.[52]

The used high pressure impinging-jet reactor (MRT CR5) is capable of generating turbulent mixings inside it's micro reaction chamber. The device consists mainly of an intensifier pump with a four horse power performance (4 kW) and a special y-formed reaction chamber with channel diameter of 75 µm (Figure 2.1.9).

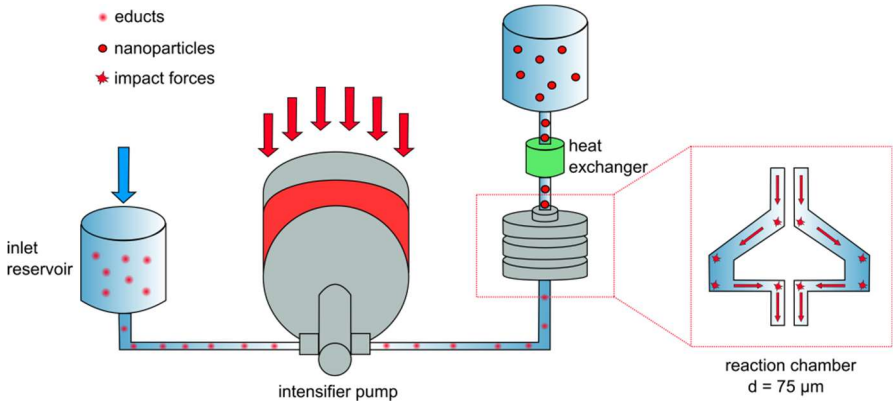

Figure 2.1.9: *Left: schematic setup of the Microfluidizer MRT CR5; right: structure of the y-formed reaction chamber.*[53]

The combination of the high performance and the geometry of the reaction chamber results in the formation of process pressures of up to 1400 bar (20000 psi) inside the reaction chamber and flow rates of approximately 500 m/s. The device can be used as a continuous reactor which allows a precise control over the particle sizes and morphologies via the reaction time (cycle number). The special geometry of the reaction chamber causes a turbulent mixing which generates a consistent pressure profile inside the chamber. Additionally two forces occur inside the chamber caused

through the high process pressures. Very high shear forces are generated in the horizontal cross connections of the chamber and very high impact forces (up to 10^6 s^{-1}) are generated through the collision of the fluid with the reaction chamber walls. An auxiliary processing module (APM) is also attached behind the reaction chamber. It consists of a z-formed reaction chamber and is responsible for the generation of a counter pressure to increase the effectiveness of the y-formed reaction chamber. The used reaction medium is progressively heated up with reaction time due to the high shear and impact forces present in the reaction chamber. Therefore the reaction medium has to be cooled down immediately after leaving the reaction chamber. This causes also a quenching of the reaction which means that the reaction only takes place inside the reaction chamber. All these factors result in a precise control over the nanoparticle sizes and morphologies. The shear and impact forces limit the growth of the nanoparticles through abrasive effects, the quenching through cooling guarantees that the particles only grow inside the reaction chamber and the high flow rates result in very short dwell times (approximately 1.0 ms) inside the chamber which induces very short and controllable growth periods.

2.1.6 Properties and Common Applications of Zinc Peroxide Nanoparticles

Zinc peroxide crystallizes in a cubic structure with the space group Pa3 (Figure 2.1.10).[54] The cubic structure of zinc peroxide itself consist of an array of irregular octahedra containing a zinc ion (Zn^{2+}) at its center surrounded by four oxygen ions (O^-) located at each corner of the polyhedron. Additionally the interatomic distance between two oxygen atoms is 1.47 Å long, 0.64 Å shorter than the bond length between a zinc ion and an oxygen ion (2.11 Å) on the same atomic array. This structure causes sites with a local charge disbalance causing a structural instability towards temperature which explains the relatively low decomposition temperature of approximately 190 °C determined via thermogravimetry.[48,50,55–58] Additionally zinc peroxide possesses a band gap of 3.3 to 4.6 eV which makes the material interesting for semi conductor applications.[46] Furthermore zinc peroxide decomposes in aqueous acidic media into zinc ions (Zn^{2+}) and hydrogen peroxide (H_2O_2), while the formed hydrogen peroxide dissociates into water and oxygen in presence of metal salts and metal oxide surfaces, given by the nanoparticle itself.[59,60] This property makes zinc peroxide nanoparticles suitable for oxygen release/biomedical

applications. For example the bactericidal properties of zinc peroxide particles were shown through their exposure to *Bacillus subtilis (B. subtilis)*, *Escherichia coli (E. coli)* and *Staphylococcus aureus (S. aureus)*. The diffusion agar method revealed that particles with average diameter of 134.0±32.0 nm established an inhibition zone around themselves in which no growth of the mentioned bacteria could be observed.[61]

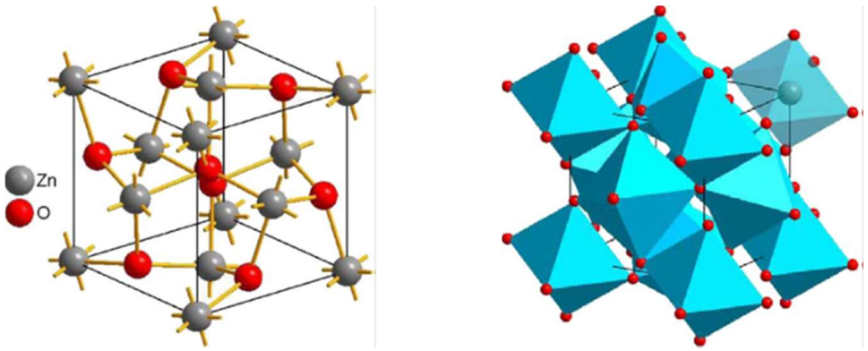

Figure 2.1.10: *Optimized unit cell of zinc peroxide (left) and the octahedral array of the cubic zinc peroxide crystal structure (right).*[62]

One common application for zinc peroxide is it's use as crosslinker for the production of carboxylated nitrile butadiene rubbers (XNBR). During the molding process of carboxyleted nitrile rubber in the presence of metallic peroxides/oxides, a carboxylic acid salt is formed that results in the formation of ionic elastomers or ionomers with greatly improved physical properties. The crosslinks produced by the zinc ion from the zinc peroxide/oxide are ionic as opposed to those produced by conventional vulcanization with sulphur accelerators or organic peroxides that are covalent.[63,64]

Furthermore zinc peroxide is used as photocatalyst. A composite material consisting of zinc peroxide and zinc oxide showed an increased photocatalytic activity compared to pure zinc oxide. The photocatalytic properties are caused through the semi conductor structures of both materials. Excited electrons and electron holes (electron/hole pair) can be generated through the irradiation with for example UV light inside the valance and conducting band of semi conducting material (Figure 2.1.11). The electrons and holes can either move to the surface of the material or can recombine inside the material. A recombination leads to a decrease of the catalytic activity of the material while the transport to the surface induces the reduction of an electron acceptor or the oxidation of an electron donator. The increased activity observed for the composite material based on the different band structures of the two

zinc compounds. This caused a potential gradient which allowed a longer separation of the electron/hole pair which minimized the recombination.[65,66]

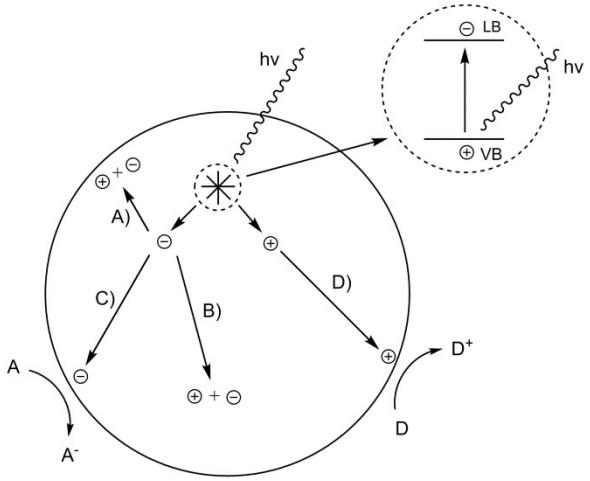

Figure 2.1.11: *Formation of the electron/hole pair through UV irradiation in semi conducting materials and their different movement sequences: surface recombination (A), volume recombination (B), electron transport to the surface (C) and hole transport to the surface (D).*[66]

Also zinc peroxide is often used as “green” precursor for the synthesis of zinc oxide nanoparticles. Therefore the zinc peroxide must be treated at approximately 190.0 °C whereby it is decomposed to zinc oxide and oxygen without any other side products. The cubic crystal structure of the peroxide is transformed to the hexagonal structure of the oxide during this process. Additionally changes the coordination of the zinc ion from octahedral to tetrahedral resulting in a more consistent crystal structure causing a much higher thermal consistency for the zinc oxide (over 1500 °C).[55]

Additionally zinc peroxide nanoparticles can be used for the oxidation of alcohols. For example the selective oxidation of aromatic alcohols to aryl aldehydes and ketones is a synthetically important reaction due to the wide applications of these compounds in synthetic organic chemistry.[67] Normally such reactions are carried out with inorganic oxidants like permanganate, bromate or Cr(VI) based compounds.[68–70] One disadvantage of this reaction management is the production of large amounts of heavy metal waste. Therefore new synthesis approaches with precious metals such as Ru, Ru modified catalysts, Pd modified compounds or supported gold nanoparticles have been developed.[71–74] However the higher costs of the precious metals and the mostly used toxic and volatile solvents limit the applicability of these approaches. Instead the catalytic activity and selectivity of zinc peroxide nanoparticles was investigated. The advantages were the relatively low decomposition temperature of the zinc peroxide (release of oxygen) and the surface

of the nanoparticles containing reactive species such as peroxy and hyperoxy radicals which can initiate the alcohol oxidation. It could be proven that zinc peroxide particles with average sizes of 50 to 150 nm converted different aromatic alcohols to their corresponding ketons or aldehydes with conversions between 84.0 and 100.0 %.These reactions were carried out in dimethyl carbonate (DMC) at 100.0 °C at reaction times between 5 and 12h. The zinc oxide which was obtained through the decomposition of the zinc peroxide could be easily separated through filtration. Afterwards the zinc oxide could be recycled through the reaction with hydrogen peroxide at 150.0 °C to give zinc peroxide.[75]

2.2 Synthesis of ZnO_2 Nanoparticles in Aqueous Media*

2.2.1 Introduction

The synthesis of zinc peroxide nanoparticles was performed in aqueous media via precipitation method in the high pressure impinging jet reactor. Zinc acetate dihydrate acted as precursor while a hydrogen peroxide solution (30 wt%) was used as precipitation agent. A possible synthesis mechanism was postulated by Escobedo-Morales et al. (Figure 2.2.1).[62]

$$Zn(CH_3COO)_2 \cdot 2H_2O \longrightarrow Zn^{2+} + 2(CH_3COO)^- + 2H_2O \quad (1)$$

$$(CH_3COO)^- + H_2O \longrightarrow CH_3COOH + OH^- \quad (2)$$

$$Zn^{2+} + 2OH^- \longrightarrow Zn(OH)_2 \quad (3)$$

$$Zn(OH)_2 + H_2O_2 \longrightarrow ZnO_2 + 2H_2O \quad (4)$$

Figure 2.2.1: *Reaction mechanism for the synthesis of zinc peroxide nanoparticles via the precipitation method.*

First the precursor dissociates into zinc ions and acetate ions (1). Since the acetate is a strong base it is immediately protonized through water molecules forming acetic acid and hydroxyl radicals (2). These radicals have a high tendency to interact with metal ions forming metal hydroxides which present in this case the intermediate compound (3). Afterwards the hydrogen peroxide reacts with the zinc hydroxide resulting in zinc peroxide and water molecules (4).

To obtain uniform nanoparticles the zinc peroxide had to be stabilized in situ with stabilizing agents. This chapter discusses the synthesis of zinc peroxide nanoparticles stabilized and functionalized with bis[2-(methacryloyloxy)ethyl] phosphate (BMEP), *o*-phosphorylethanolamine (*o*-PEA) and citrate (Figure 2.2.2). The phosphate function of the BMEP and *o*-PEA should interact with the zinc peroxide surface resulting in the stabilization of the particles while the two methacrylate functions respectively the amine function should remain intact after the synthesis providing a functionalization of the nanoparticle surface. The double bonds could for example be used to incorporate the synthesized nanoparticles into polymeric structures via radical polymerization. Furthermore the BMEP stabilized nanoparticles could act as a crosslinking agent during polymerization due to the multiple double bonds presented on their surface. Contrary the amine functions could

*Reproduced from Christian Bergs, Paul Simon, Yurii Prots, Andrij Pich; *RSC Adv.*, 2016, **6**, 84777 with permission from the Royal Society of Chemistry and from Dennis Berg, Christian Bergs, Karola Schäfer, Andrij Pich, Martin Möller; *Zinc Peroxide Particles as Bleaching Agents to Improve the Color of Postconsumer Poly(ethylene terephthalate)* (submitted).

for example be used for polycondensations with carboxylates or for click-reactions with epoxide compounds (more details see section 4.1.2) which offers diverse post-modification possibilities.

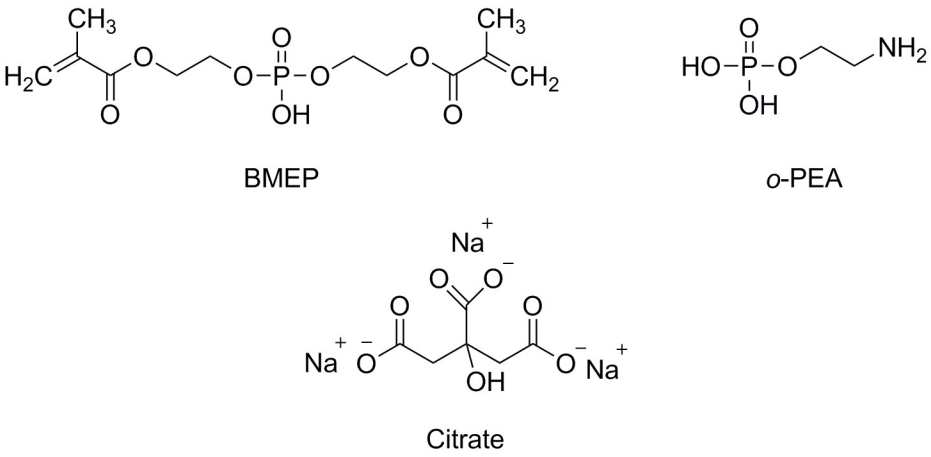

Figure 2.2.2: *Chemical structures of the stabilizer molecules bis[2-(methacryloyloxy)ethyl] phosphate (BMEP), o-phosphorylethanolamine (o-PEA) and citrate.*

Furthermore at least one of the carboxylate functions of the citrate should interact with the nanoparticle surface resulting in stabilized nanoparticles. The non-interacting carboxylate groups should functionalize the zinc peroxide surface and could be used for further post synthesis modifications. For example citrate was intensively used for the stabilization of gold nanoparticles and their incorporation into polymeric structures. It could be shown that the citrate formed mostly hydrogen bonds with for example the amide function of poly(N-isopropylacrylamide) (PNIPAm) acting as a linker between the gold nanoparticles and the polymer.[76,77]

2.2.2 Chemical Structure of ZnO_2 Nanoparticles

The high pressure impinging-jet reactor (MRT CR5) was used for the synthesis of the zinc peroxide nanoparticles stabilized with BMEP, *o*-PEA and citrate. The process pressure was kept constant at 1400 bar, to obtain the smallest particles as possible, while the influence of different cycle numbers or reaction times (5 (2min), 10 (4min), 20 (8min), 30 (12min) and 40 (16min) cycles) and precursor:stabilizer ratios (1/1, 5/1 and 10/1) on the particle sizes, the crystal structure, the sample composition and the conversion was investigated. XRD measurements revealed, that the typical zinc peroxide reflexes could be obtained for all synthesized samples (Figure 2.2.3).

Therefore only one representative diffractogram is shown for every nanoparticle/stabilizer system.

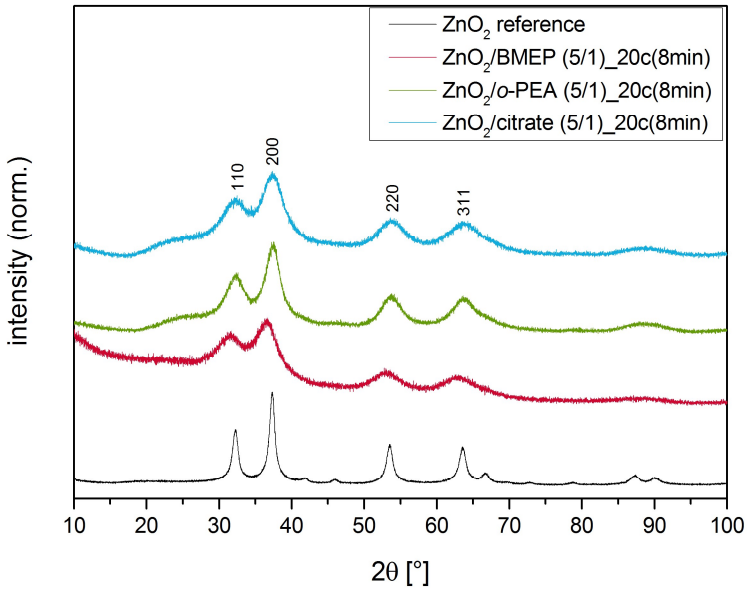

Figure 2.2.3: *XRD diffractograms of the obtained zinc peroxide nanoparticles synthesized with different stabilizer molecules in comparison to a zinc peroxide reference substance.*

The measurements showed for all different samples the same reflexes at 2θ = 31.0, 36.5, 53.0 and 63.0°, which could be assigned to the cubic crystal structure of zinc peroxide, through comparison with the measured reference diffractogram. Additionally the reflexes could be assigned to the indexes 111, 200, 220 and 311 characteristic for the cubic structure with the space group Pa3.[54,62] Furthermore the graphs showed broadened XRD reflexes, suggesting that the samples consisted of ZnO_2 nanoparticles.[78] By determination of the full width at half maximum (FWHM radian) of the reflexes 220 and 311 for every sample via profile fitting using a XRD pattern processing software it was possible to calculate the average crystallite sizes and the related standard deviations of the different samples using the Debye-Scherrer equation:

$$d = \frac{k\lambda}{\beta cos\theta} \qquad [5]$$

where: k = constant (0.9), λ = wavelength of the X-ray (0.1542 nm), β = FWHM radian and θ = diffraction angle.[79] Crystallite sizes between 2.4±0.0 and 3.6±0.6 nm (see section 2.2.3) could be calculated indicating that the obtained products indeed consisted of nanoparticles. But one have to keep in mind that the crystallite size must not be equivalent to the real nanoparticle size due to the fact that nanoparticles can

consist of a different number of crystallites (detailed discussion see section 2.2.3). Due the fact that pure zinc peroxide was already obtained after five cycles, which corresponds approximately to a reaction time of 2 minutes, it was obviously shown how fast the reaction could be realized by using the impinging-jet reactor. This phenomenon could be ascribed to the special geometry of the reaction chamber and the high process pressure. A turbulent and very effective mixing of the reactants could be achieved by these two factors, which resulted in very short reaction times.

In contrast, to the non existing influence of the reaction parameter on the crystal structure, a dependence of different reaction times (cycle numbers) and precursor:stabilizer ratios on the conversion of the used precursor zinc acetate and the different sample compositions could be observed. Thermogravimetric analysis (TGA) showed that 8min reaction time (20 cycles) resulted in the highest conversion for the BMEP stabilized nanoparticles (Figure 2.2.4, Table 2.2.1).

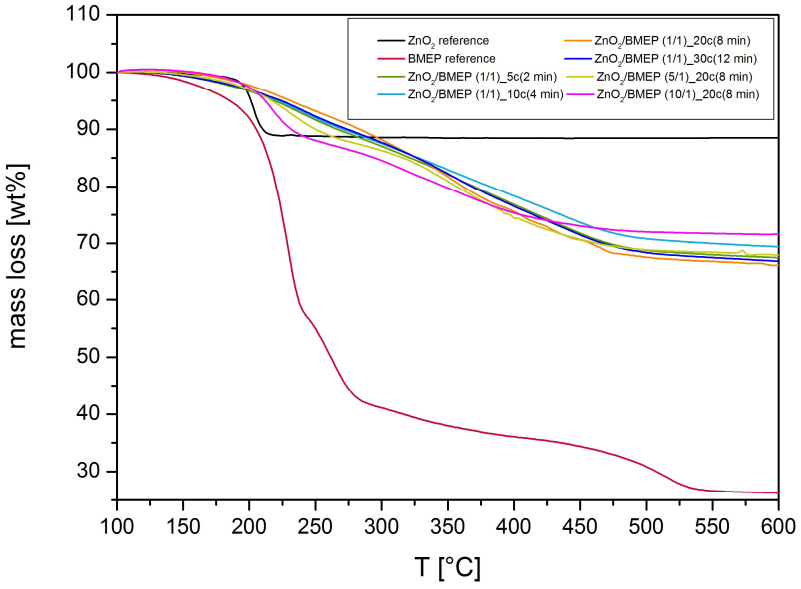

Figure 2.2.4: *Thermogravimetric measurements of the different ZnO_2/BMEP nanoparticle samples at different reaction times (cycle numbers) and precursor:BMEP ratios in comparison to the reference substances zinc peroxide and BMEP.*

To determine the conversion, it was necessary to calculate the different sample compositions first. By calculating the derivations of the measured thermograms with a Netzsch analytical program (Marsh method) it was possible to identify, separate and quantify the decomposition steps and their onset temperatures for zinc peroxide and BMEP in the synthesized nanoparticle samples. Additional reference measurements of pure zinc peroxide and BMEP supported the identification of the different

decomposition steps of the synthesized samples and allowed the calculation of their composition (Figure 2.2.4).

Table 2.2.1: *Sample compositions and conversions determined via TGA measurements for the BMEP stabilized zinc peroxide nanoparticles.*

Sample	Sample composition ZnO_2/BMEP [wt%/wt%]	Conversion $Zn(ac)_2$ [%]
ZnO_2/BMEP (1/1)_5c(2min)	65.7/34.3	37.5
ZnO_2/BMEP (1/1)_10c(4min)	63.8/36.2	37.9
ZnO_2/BMEP (1/1)_20c(8min)	62.3/37.7	46.7
ZnO_2/BMEP (1/1)_30c(12min)	61.7/38.3	20.5
ZnO_2/BMEP (5/1)_20c(8min)	71.5/28.5	50.6
ZnO_2/BMEP (10/1)_20c(8min)	78.0/21.9	45.2

The reference measurements showed for zinc peroxide one decomposition step in the temperature range of 193.0 to 210.0 °C, while the BMEP reference showed several decomposition steps between 208.2 to 534.4 °C. A similar behaviour could be investigated for the synthesized samples too. The calculated onset temperatures (Marsh method) for the first decomposition step were 189.9 (ZnO_2/BMEP (1/1)_5c(2min)), 188.7 (ZnO_2/BMEP (1/1)_10c(4min)), 187.9 (ZnO_2/BMEP (1/1)_20c(8min)) and 175.7 °C (ZnO_2/BMEP (1/1)_30c(12min)) which agreed quite well with the zinc peroxide reference measurement. This showed that the first decomposition step of the synthesized samples could be assigned to the amount of zinc peroxide present in the samples. The following decomposition steps starting between 220.0 and 230.0 °C could consequently only be addressed to the decomposition of the BMEP and by that to the amount of BMEP present in the different samples.

The evaluation of the data showed that similar product ratios were obtained for all four reaction time experiments. The ZnO_2/BMEP ratios were between 61.7/38.3 and 65.7/34.3 wt%/wt%, which showed that the reaction time did not have a significant influence on the final sample compositions in that case, what was desirable, due to the fact, that the same educt ratio was used in the four experiments. This showed the reproducibility of the nanoparticle synthesis. Furthermore the resulting conversion showed a correlation to the reaction times. The conversion increased with increasing reaction time up to 8 minutes, but a further increase to 12 minutes resulted in a much

lower conversion of zinc acetate. The increase can be explained through a more efficient transformation of $Zn(ac)_2$ to ZnO_2, while the following decrease did not fit to the expectations. An explanation could be that the irregular crystal structure (mentioned above) of zinc peroxide started to decompose at the longest reaction time, due to the longer exposure to the high pressures and shear forces. Further the TG data showed a direct correlation between the initial educts ratio and the final sample composition. Through the increase of the zinc acetate concentration from $8.58 \cdot 10^{-4}$ (1/1) to $4.90 \cdot 10^{-3}$ mol/L (10/1) it was possible to increase the amount of zinc peroxide from 62.3 to 78.0 wt% and to decrease the BMEP amount from 37.7 to 21.9 wt% respectively. This behavior showed that a control over the sample composition of the BMEP stabilized nanoparticles was possible.

Similar trends could be observed for the *o*-PEA stabilized zinc peroxide nanoparticles. Thermogravimetric measurements (Figure 2.2.5) showed that the conversion of the precursor zinc acetate increased from 7.7 to 13.5 % with increasing reaction time from 2 min to 8 min at constant precursor/stabilizer ratio of 1/1 (Table 2.2.2). A comparable increase was observed for different educt ratios, too.

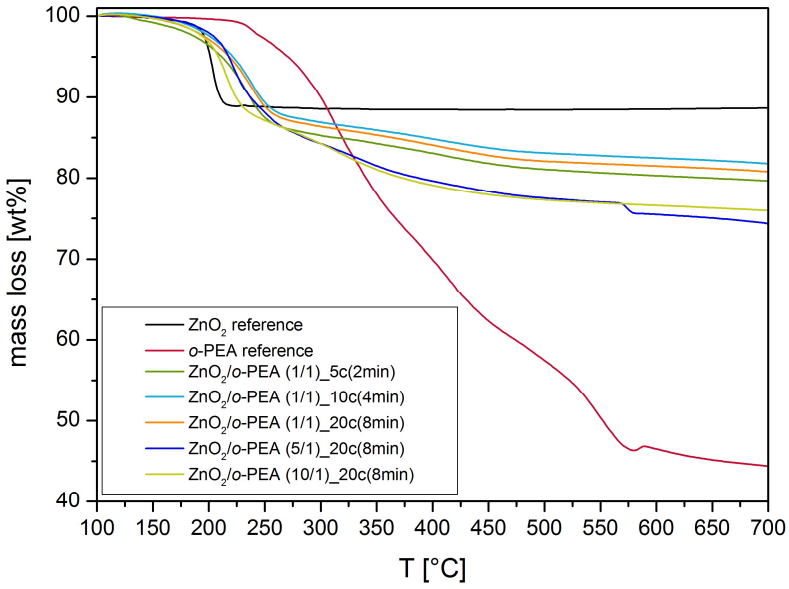

Figure 2.2.5: *Thermogravimetric measurements of the different ZnO_2/o-PEA nanoparticle samples at different reaction times (cycle numbers) and precursor:o-PEA ratios in comparison to the reference substances zinc peroxide and o-PEA.*

The conversion of the precursor increased from 35.0 to 41.1 % with decrease of the *o*-PEA concentration from 5/1 to 10/1. These two trends showed that a high concentration of *o*-PEA (ZnO_2/*o*-PEA (1/1) samples) seemed to inhibit the conversion

of zinc acetate to zinc peroxide. An explanation could be that a high *o*-PEA concentration prevents the necessary nucleation of the zinc ions induced through a local supersaturation of the reaction solution.[32] The sample compositions were calculated based on the decompositions steps analogously to the already discussed BMEP stabilized nanoparticles. The *o*-PEA reference showed several decomposition steps in a temperature range of 263.9 to 610.0 °C which could also be detected for the synthesized nanoparticles. The corresponding sample thermograms showed a first decomposition step at 170.1 (ZnO_2/*o*-PEA (1/1)_5c(2 min)), 182.5 (ZnO_2/*o*-PEA (1/1)_10c(4 min)), 183.2 (ZnO_2/*o*-PEA (1/1)_20c(8 min)), 203.5 (ZnO_2/*o*-PEA (5/1)_20c(8 min)) and 197.5 °C (ZnO_2/*o*-PEA (10/1)_20c(8 min)) followed by a second broad decomposition step in the temperature range of approximately 250.0 to 600.0 °C. Nearly all first decomposition temperatures were in good accordance with the decomposition temperature of the zinc peroxide reference measurement indicating that this decomposition step could be attributed to the sample amount of zinc peroxide. Only the first decomposition temperature of the sample ZnO_2/*o*-PEA (1/1)_5c(2 min) (170.1 °C) differed from this trend. An explanation could be the presence of crystal water inside the sample which falsifies the determination of the temperature.[80] Consequently, the following broad decomposition step between 250.0 and 600.0 °C could only be assigned to the decomposition and the sample amount of the stabilizer *o*-PEA.

Table 2.2.2: *Compositions of the synthesized ZnO_2/o-PEA particles and conversions determined by TGA measurements for the experiments performed at different reaction times and educt ratios.*

Sample	Sample composition ZnO_2/*o*-PEA [wt%/wt%]	Conversion $Zn(ac)_2$ [%]
ZnO_2/*o*-PEA (1/1)_5c(2 min)	18.3/81.7	7.7
ZnO_2/*o*-PEA (1/1)_10c(4 min)	23.2/76.8	11.1
ZnO_2/*o*-PEA (1/1)_20c(8 min)	26.6/73.4	13.5
ZnO_2/*o*-PEA (5/1)_20c(8 min)	68.1/31.9	35.0
ZnO_2/*o*-PEA (10/1)_20c(8 min)	75.5/24.5	41.1

The sample composition calculations revealed that the amount of zinc peroxide increased with increasing reaction time. For example, the sample ZnO_2/*o*-PEA (1/1)_5c(2 min) showed only a ZnO_2 content of 18.3 wt% while the ZnO_2/*o*-PEA (1/1)_20c(8 min) sample already showed a ZnO_2 content of 26.6 wt%. This was in

line with the already discussed zinc acetate conversions which increased with longer reaction times. The continuous reduction of the initial *o*-PEA synthesis concentration led also to higher zinc peroxide contents. The ZnO_2/*o*-PEA (5/1)_20c(8 min) sample showed a ZnO_2 content of 68.1 wt% while ZnO_2/*o*-PEA (10/1)_20c(8 min) revealed a content of 75.5 wt% which also fulfilled the expectations.

The conversions and sample compositions of the citrate stabilized nanoparticles were determined via inductively coupled plasma atom emission spectroscopy (ICP-OES). A dispersion of the different nanoparticles was introduced to an ionized argon gas which initiated the ionization of the sample. The formed ions could be quantitatively separated by their different mass to charge ratios which allowed the determination of the zinc ion concentration (Zn^{2+}). This concentration enabled the calculation of the zinc peroxide content of the different samples and consequently the calculation of the citrate sample amount (Table 2.2.3).[81]

Table 2.2.3: *Sample compositions and precursor conversions for the different zinc peroxide nanoparticle samples stabilized with citrate.*

Sample	Sample composition ZnO_2/citrate [wt%/wt%]	Conversion $Zn(ac)_2$ [%]
ZnO_2/citrate (1/1)_20c(8min)	14.1/85.9	22.9
ZnO_2/citrate (1/1)_30c(12min)	21.9/78.1	40.1
ZnO_2/citrate (1/1)_40c(16min)	32.2/67.8	55.4
ZnO_2/citrate (5/1)_20c(8min)	64.9/35.1	33.8
ZnO_2/citrate (10/1)_20c(8min)	61.5/38.5	35.4

It could be shown that the zinc peroxide content increased from 14.1 (ZnO_2/citrate (1/1)_20c(8min)) to 32.2 wt% (ZnO_2/citrate (1/1)_40c(16min)) with increasing reaction time from 8 to 16 minutes at constant zinc acetate/citrate ratio of 1/1. Simultaneously the conversion of the precursor increased from 22.9 to 55.4 %, which was a comparable trend to the *o*-PEA stabilized nanoparticles. Furthermore different zinc acetate/citrate ratios did also influence the sample composition and the precursor conversion. The zinc peroxide content increased from 14.1 to 64.9 wt% with decreasing initial stabilizer concentration from 0.043 (1/1) to 0.009 mol/L (5/1) showing that an adjustment of the final sample composition was possible by tuning the initial educt ratios. A further initial stabilizer concentration decrease to 0.004 mol/L (10/1) did not result in a significant change of the zinc peroxide content (61.5

wt%) indicating that some kind of equilibrium was reached. Additionally the conversion increased from 22.9 (1/1) to 33.8 (5/1) respectively 35.4 % (10/1) with decreasing stabilizer concentration.

These investigations showed that in most cases the precursor conversion increased with increasing reaction time and that the sample compositions could be tuned through the adjustment of the initial precursor/stabilizer ratios.

2.2.3 Size and Morphology of ZnO_2 Nanoparticles

Transmission electron microscopy (TEM) investigations showed for all synthesized samples very small and uniform nanoparticles. This indicated, that the stabilizer molecules BMEP, *o*-PEA and citrate interacted strongly with the particle surface, which resulted in efficient sterical/electrostatic stabilization of the nanoparticles. A second reason for the very small particle sizes and uniform morphologies was the high process pressure (1400 bar) and the special y-formed reaction chamber with channel diameter of 75 µm. Through the combination of the high process pressure and the small channel diameter, it was possible to generate very high shear and impact forces up to $7 \cdot 10^6$ s^{-1} inside the reaction chamber. These reaction conditions guaranteed that the growth of the formed nuclei was restricted and that the nanoparticles remained small and uniform The particle sizes were additionally controlled by very short growth periods. Due to the high process pressure, it was possible to achieve a flow rate of 480.0 mL/min through the reaction chamber which resulted in a dwell time of approximately 1.0 ms inside the chamber. The nanoparticle synthesis itself could only take place inside the chamber due to the fact that the needed reaction temperature of 100 °C was only present there (caused through the shear and impact forces), which resulted in combination with the mentioned dwell time in very short growth periods.[62] To additionally guarantee, that the nanoparticles only grew inside the reaction chamber, the reaction solution was immediately quenched with ice-cooled water after leaving the chamber. Through this procedure the particle growth stopped and didn't restart until the reaction solution re-entered the reaction chamber. The resulting average particle sizes and standard deviations (Figure 2.2.6 and Table 2.2.4) were determined by measuring diameters of 100-200 individual nanoparticles in TEM images followed by standard deviation calculation

(only representative examples are shown in Figure 2.2.6, all other images are shown in section 7).

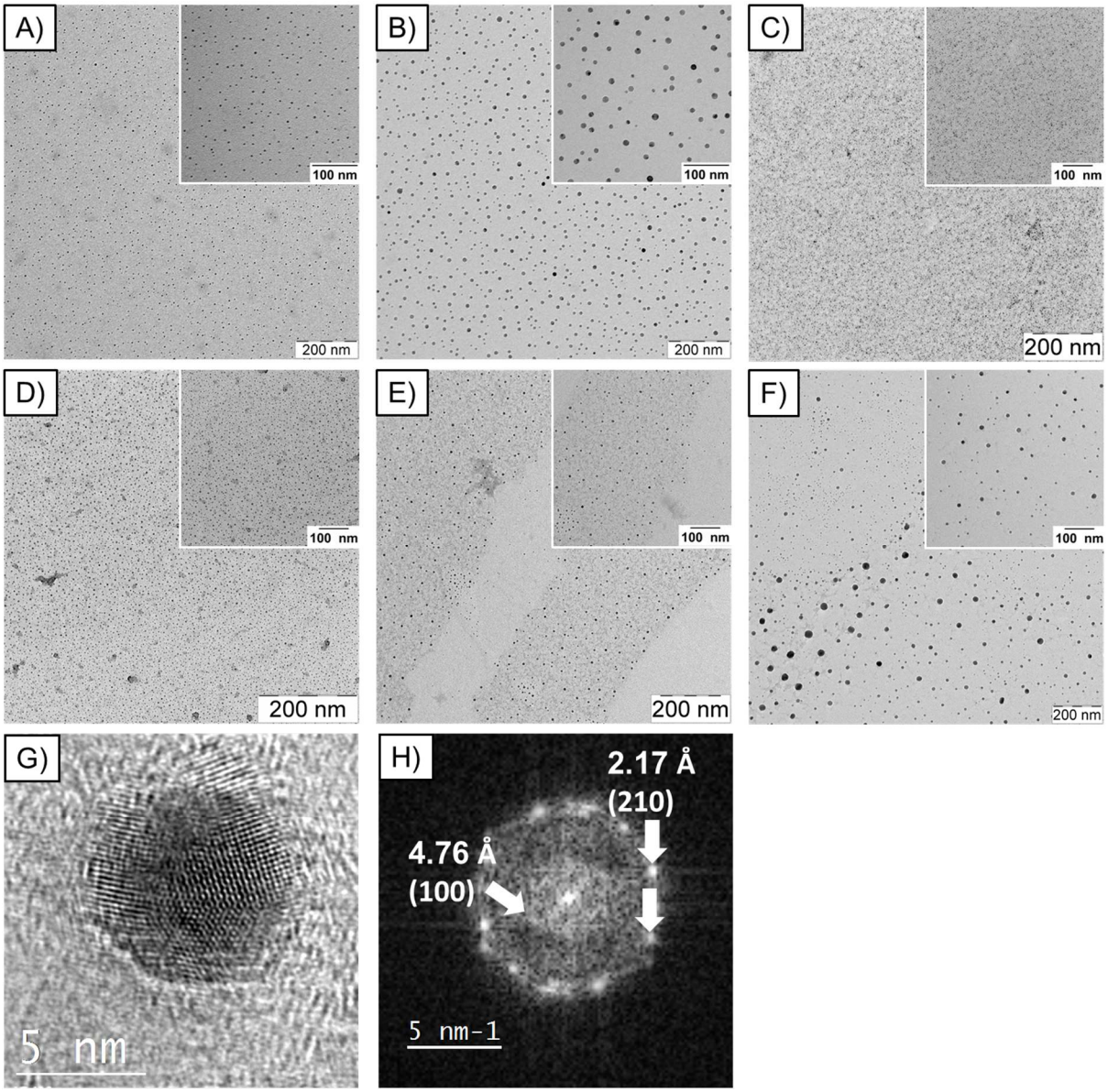

Figure 2.2.6: *TEM images of zinc peroxide nanoparticles stabilized with BMEP, o-PEA and citrate; A) ZnO_2/BMEP (1/1)_10c(4min), B) ZnO_2/BMEP (1/1)_30c(12min), C) ZnO_2/o-PEA (1/1)_5c(2 min), D) ZnO_2/o-PEA (1/1)_20c(8 min), E) ZnO_2/citrate (1/1)_20c(8min), F) ZnO_2/citrate (1/1)_40c(16min), G) HR-TEM image of the sample ZnO_2/BMEP (1/1)_5c(2min). The image was filtered in order to enhance signal noise ratio, for further details see text, H) Fast Fourier transform of Figure G). The nanocrystal is composed at least of three different subcrystals rotated with respect to each other.*

The investigations proved that the nanoparticle diameter of the BMEP stabilized nanoparticles were dependent on different reaction times and zinc acetate:BMEP ratios. The particle diameter decreased from 5.2±2.6 nm to 3.9±1.2 nm by increasing the reaction time from 2min to 4min, while a further reaction time increase to 8min and 12min led to bigger particles with diameter of 7.0±2.0 and 14.4±5.2 nm. The decrease of the nanoparticle sizes, which occurred in the first place, could be

explained by the increased exposition of the nanoparticles to the shear and impact forces, which reduced the sizes by abrasive effects. The following increase of the sizes and standard deviations could only be explained through enhanced Ostwald ripening, which can especially be seen based on the increasing standard deviation of the formed nanoparticles. Small particles were dissolved while bigger grew further at longer reaction times.[23] Further different zinc acetate:BMEP ratios resulted in different nanoparticle diameter. By increasing the zinc acetate concentration from $8.58 \cdot 10^{-4}$ mol/L to $2.51 \cdot 10^{-3}$ mol/L the particle sizes decreased from 7.0±2.0 nm to 3.3±0.9 nm. These observations coincide with the literature. Through a higher precursor concentration, a higher local supersaturation of the reaction solution was obtained, which influenced the nucleation and diffusion of the particles. The particle sizes decreased, because the nucleation rate increased disproportionately compared to the growth rate.[32] In contrast a further increase of the precursor concentration to $4.90 \cdot 10^{-3}$ mol/L led to bigger particles with average diameter of 11.5±3.6 nm. An explanation for this deviating behavior could be that the supersaturation reached a critical level, which resulted in coagulation of the particles.

Figure 2.2.6G shows the HRTEM image of a 7.0 nm large ZnO_2 nanocrystal stabilized with BMEP. The image was processed in order to obtain average background subtracted filter images of the HRTEM images, based on R. Kilaas's work.[82] This script carries out filtering of HRTEM images in frequency space. It uses rotational averaging of the fast Fourier transform (FFT) to separate the discrete spots due to crystalline material from the continuum due to amorphous material. The average amorphous component is then subtracted, to leave the just crystalline component. Figure 2.2.6H shows the FFT of figure 2.2.6G revealing that the nanocrystal is composed at least of three different domains.

Contrary the *o*-PEA stabilized nanoparticles showed no significant changes during the reaction parameter variations (Figures 2.2.6C and D). Small and uniform nanoparticles with diameters between 2.4±0.7 and 3.9±1.2 nm were obtained depending on different zinc acetate:*o*-PEA ratios (1/1, 5/1 and 10/1) and reaction times (2, 4 and 8min).

Table 2.2.4: *Nanoparticle diameters and crystallite sizes with corresponding standard deviations for the different stabilized ZnO_2 samples.*

Sample	Particle diameter [nm] (TEM)	Crystallite size [nm] (XRD)
ZnO_2/BMEP (1/1)_5c(2min)	5.2±2.6	2.5±0.2
ZnO_2/BMEP (1/1)_10c(4min)	3.9±1.2	3.6±0.6
ZnO_2/BMEP (1/1)_20c(8min)	7.0±2.0	2.5±0.3
ZnO_2/BMEP (1/1)_30c(12min)	14.4±5.2	2.4±0.0
ZnO_2/BMEP (5/1)_20c(8min)	3.3±0.9	2.6±0.1
ZnO_2/BMEP (10/1)_20c(8min)	11.5±3.6	2.4±0.1
ZnO_2/*o*-PEA (1/1)_5c(2 min)	2.4±0.7	2.6±0.1
ZnO_2/*o*-PEA (1/1)_10c(4 min)	2.9±1.0	2.8±0.1
ZnO_2/*o*-PEA (1/1)_20c(8 min)	3.9±1.2	3.0±0.2
ZnO_2/*o*-PEA (5/1)_20c(8 min)	2.4±0.7	2.9±0.2
ZnO_2/*o*-PEA (10/1)_20c(8 min)	3.3±1.0	2.9±0.2
ZnO_2/citrate (1/1)_20c(8min)	6.5±1.6	---
ZnO_2/citrate (1/1)_30c(12min)	6.7±2.9	---
ZnO_2/citrate (1/1)_40c(16min)	10.6±6.7	---
ZnO_2/citrate (5/1)_20c(8min)	6.1±2.0	2.4±0.2
ZnO_2/citrate (10/1)_20c(8min)	7.3±3.1	2.3±0.1

However the nanoparticles stabilized with citrate showed similar trends like the BMEP stabilized nanoparticles. The nanoparticle diameter increased from 6.5 to 10.6 nm with increasing reaction time from 8 to 16 min. Furthermore the calculated standard deviation increased from ±1.6 to ±6.7 nm indicating a decrease in uniformity caused through Ostwald ripening. Furthermore different zinc acetate:citrate ratios did have a slightly influence on the nanoparticle sizes. The diameter increased from 6.5±1.6 (1/1) to 7.3±3.1 nm (10/1) with decreasing stabilizer concentration from 0.043 to 0.004 mol/L. Although this diameter increase lay within the tolerance of the calculated standard deviations, indicated the increase of the standard deviations form ±1.6 to ±3.1 nm clearly that the citrate concentration decrease caused a more uncontrolled particle growth resulting in more irregular particles.

The crystallite size determinations made via the Debye Scherrer equation (section 2.2.2) supported the assumptions based on the TEM images. Very small crystallite sizes between 2.4±0.0 and 3.6±0.6 nm were calculated for most samples. Only the

crystallite sizes of the (1/1) citrate stabilized nanoparticles could not be calculated due to their high stabilizer content which disturbed the XRD measurements. The comparison to the determined diameter revealed that the synthesized nanoparticles consisted mostly of two to four crystallites each. Especially the comparison with the HR-TEM measurement (Figure 2.2.6G) of sample ZnO_2/BMEP (1/1)_5c(2min), which showed three crystallites for the nanoparticle, proved the really good correlation.

2.2.4 Chemical Composition of ZnO_2 Nanoparticles Surface

Based on the successful synthesis of very small and uniform nanoparticles in aqueous solutions discussed above, one may conclude that the stabilizer molecules BMEP, *o*-PEA and citrate efficiently interacted with the ZnO_2 surface. Especially the phosphates should interact with the nanoparticle surface forming covalent or hydrogen bonds as already investigated for similar nanoparticle systems.[41,42,53] Raman spectroscopy and Fourier transform infrared spectroscopy (FTIR) measurements were performed, to investigate the interaction between the phosphate respectively the carboxylate function of the stabilizer molecules and the particle surface, while pH dependent zeta potential measurements revealed the change of the nanoparticle surface charge.

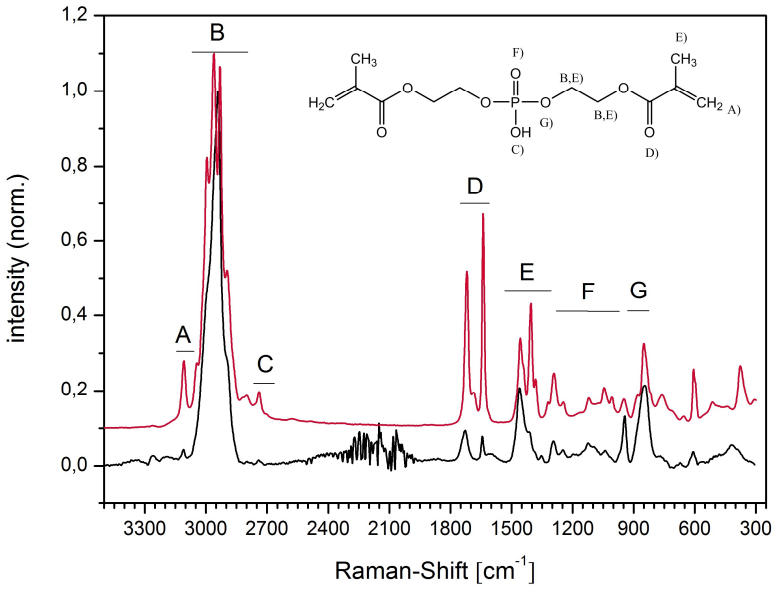

Figure 2.2.7: *Raman spectra of the ZnO_2/BMEP (1/1)_20c(8min) sample (black) and a BMEP reference substance (red).*

Figure 2.2.7 shows spectra of a ZnO_2/BMEP sample, as well as the spectrum of the BMEP reference substance. The characteristic bands of the aliphatic hydrocarbons showed mostly no change, besides of the band broadening of signal E. The BMEP reference spectrum showed instead of this a duplet signal at this Raman-shift. This can be explained by a higher packing density of the BMEP molecules in the bulk material compared to the particle surface in the synthesized sample.[83] Conversely, the phosphate bands showed significant changes. The sample spectrum didn't show the bands for the P-OH function (signal C), one P=O band at 1320 cm^{-1} vanished (signal F) and one P-O band at 1006 cm^{-1} disappeared (signal G). Based on previous works of Kim et al., this data indicated that the P-OH and P=O functions of BMEP interacted with the zinc peroxide surface, forming a bidentate bonding (Figure 2.2.11).[84] The characteristic bands of the methacrylate function (signal A) at 3108 cm^{-1} showed a strongly decreased intensity compared to the reference spectrum, which would mean that some of the double bonds of the methacrylate functions were decomposed during the synthesis. But the ratios between the carbonyl (1718 cm^{-1}) and the vinyl (3108 cm^{-1}) bands remained nearly the same for the composite sample and the BMEP reference. Values of 1.85 (BMEP reference) and 2.14 (ZnO_2/BMEP sample) were calculated. The increased ratio of 2.14 indicated again that the double bonds were decomposed, but it showed also that only a small amount of the double bonds were inactive. Most of the functions were stable during the synthesis, and could be used for further modifications steps, like grafting or polymerization processes.

Further Raman spectroscopy measurements revealed the interaction between *o*-PEA and the nanoparticle surface. Figure 2.2.8 shows the Raman spectra of one synthesized ZnO_2/*o*-PEA sample and of the *o*-PEA reference substance. The signals of the sample measurement (black) are mostly in good accordance with the reference measurement (red) indicating that *o*-PEA remained inert during the synthesis. For example, the asymmetric and symmetric stretching vibrations of the aliphatic hydrocarbons at 3046 to 2727 cm^{-1} (signal A) and the deformation vibration of the primary amino function at 1640 cm^{-1} (signal C) showed nearly no differences.

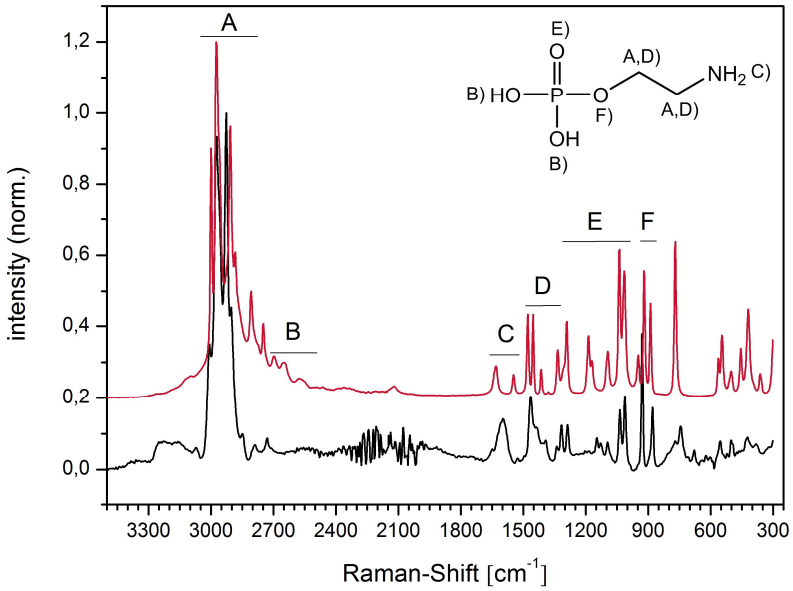

Figure 2.2.8: *Raman spectra of the ZnO_2/o-PEA (1/1)_20c(8 min) sample (black) and an o-PEA reference substance (red).*

Contrary, a duplet signal at 1483 to 1456 cm^{-1} (signal D) was detected for the reference *o*-PEA while the sample spectrum showed only a broadened signal. The broadening of the signal can again be explained by the lower packing density of the *o*-PEA molecules on the nanoparticle surface compared to the bulk reference substance resulting in less discrete signals.[83] Additionally, changes of the characteristic bands of the phosphate function were observed. The stretching bands of the P-OH bond in the range of 2650 to 2570 cm^{-1} (signal B) vanished completely for the sample spectrum, while one band of the P=O bond was shifted from 1190 to 1130 cm^{-1} (signal E) and one band of the P-O bond at 951 cm^{-1} (signal F) vanished. The comparison to the BMEP stabilized nanoparticles and previously published literature led to the assumption that the o-PEA could have formed a tridentate bond to the zinc peroxide surface.[84]

The surface composition of the citrate stabilized nanoparticles was investigated via Fourier transform infrared spectroscopy (FTIR) measurements (Figure 2.2.9). Figure 2.2.9 shows the measurements for the sample ZnO_2/citrate (10/1)_20c(8min) and the citrate reference. The obtained signals of the reference measurement could be assigned to the different functional groups of the stabilizer. For example could the signals at 1577 cm^{-1} (signal B) and 1391 cm^{-1} (signal C) be allocated to the asymmetric and symmetric stretching vibrations of the deprotonated carboxylate groups of the citrate molecule.

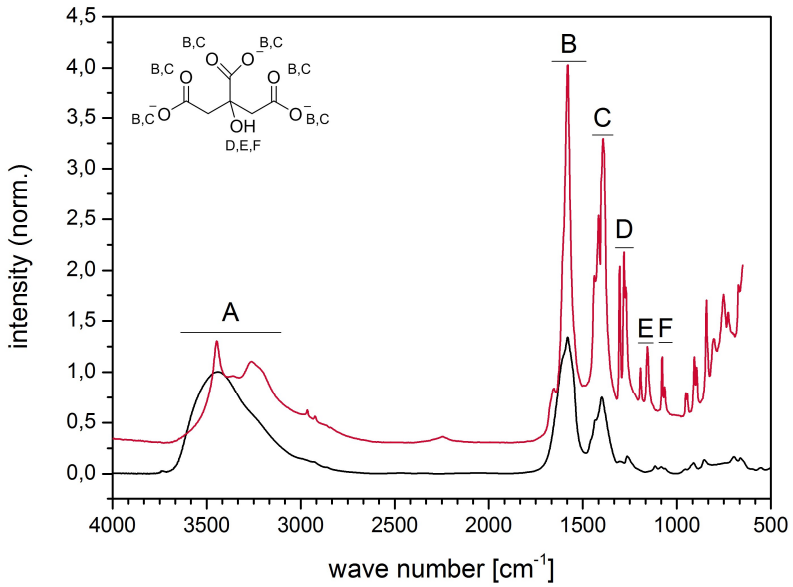

Figure 2.2.9: *FTIR spectra of the ZnO_2/citrate (10/1)_20c(8 min) sample (black) and the citrate reference substance (red).*

Furthermore the signals at ~1300 cm^{-1} (signal D), ~1170 cm^{-1} (signal E) and ~1080 cm^{-1} (signal F) could be assigned to the deformation vibration of the tertiary alcohol function (-OH) and to the stretching vibrations of the corresponding C-O bonds. Signal A was caused through the presence of crystal water in the samples (stretching vibration of –OH). The comparison with the sample spectrum revealed significant differences indicating an interaction between the citrate molecules and the zinc peroxide nanoparticle surface. A strong intensity decrease of the signals B and C could be observed for the sample spectrum which could only be caused through a change of the chemical configuration of the carboxylate functions of the citrate. Furthermore the characteristic signals of the tertiary alcohol function showed changes too. The intensities of all three signals (D, E, F) significantly decreased while the signal E was also shifted from 1170 to 1120 cm^{-1}. These changes could indicate that the hydroxyl function also interacted with the nanoparticle surfaces. Previous studies concerning the stabilization of gold nanoparticles with citrate postulated that at least one of the carboxylate functions interacted with the nanoparticle surface resulting in an electrostatic stabilization. It was also shown that this electrostatic interaction was mostly caused through physisorption, which allows the assumption that a similar mechanism can be postulated for the synthesized zinc peroxide nanoparticles.[85–87]

The interaction of the stabilizers with the nanoparticle surface caused further a change of the surface charge of these particles. These changes were investigated

with pH dependent zeta potential measurements. One representative sample was measured for each type of stabilized nanoparticle (ZnO_2/BMEP (1/1)_20c(8min), ZnO_2/*o*-PEA (1/1)_20c(8 min), ZnO_2/citrate (10/1)_20c(8min)) in combination with a reference measurement of unmodified zinc peroxide (Figure 2.2.10). The zeta potential diagram shows for the unmodified zinc peroxide a typical ampholyte behavior with isoelectric point around pH=8. The surface hydroxide functions were protonated in acidic media, which resulted in a positive surface charge, while a deprotonation of the hydroxide functions took place in basic media, which resulted in a negative surface charge.[88]

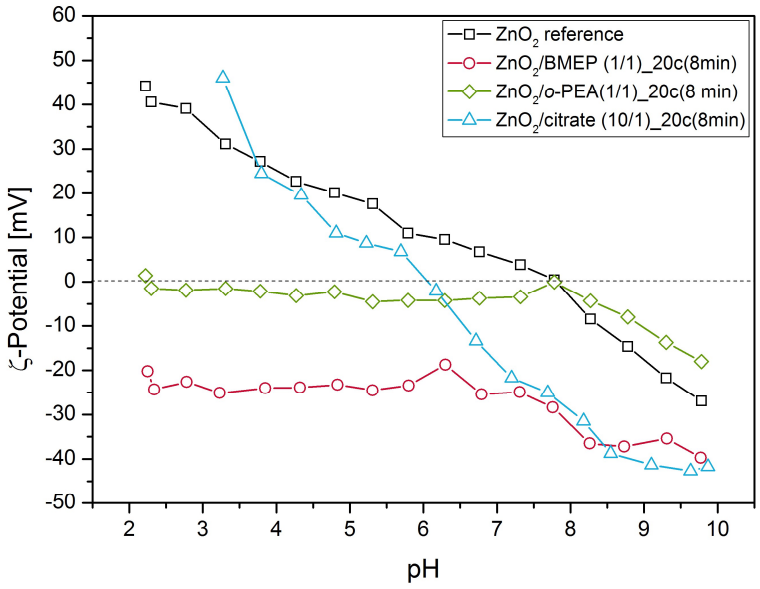

Figure 2.2.10: *pH dependent zeta potential measurements for the samples ZnO_2/BMEP (1/1)_20c(8min) (red), ZnO_2/o-PEA (1/1)_20c(8 min) (green),ZnO_2/citrate (10/1)_20c(8min) (blue) and a ZnO_2 reference substance (black).*

In contrast to that, the surface of the ZnO_2/BMEP nanoparticles exhibits negative surface charge in the whole pH range. This negative surface charge can only be explained through the deprotonation of the P-OH function of the BMEP.[89] But the Raman data showed that the P-OH function interacted with the nanoparticle surface, which would mean that this function could not be deprotonated in aqueous media. An explanation for this contradictory data would be the formation of a BMEP double layer around the nanoparticles (Figure 2.2.11). The first layer would interact with the particle surface through the P-OH function, which was proven by the Raman measurements, while the second layer would interact with the solvent under deprotonation, which would explain the negative surface charge.

Contrary the ZnO_2/*o*-PEA nanoparticles showed a nearly neutral/slightly negative surface charge in a pH range from 2.0 to 8.0 followed by a continuous decrease in surface charge (to -17.9 mV) with increasing pH value (pH = 10.0). An explanation for the nearly neutral/slightly negative surface charge could be the formation of an *o*-PEA double layer around the nanoparticles similar to the ZnO_2/BMEP samples (Figure 2.2.11). In this case, the first layer of the *o*-PEA would interact with the nanoparticle surface through the phosphate function while its free amine function would be protonated in acidic media and deprotonated in basic media. At the same time, the free phosphate functions of the second *o*-PEA layer would be deprotonated over the whole pH range resulting in combination with the positively charged amine functions (pH = 2.0 to 8.0) in a nearly neutral zeta potential. The subsequent decrease of the zeta potential (pH = 8.0 to 10.0) could be explained by the combined negative charges of the amine and phosphate function.

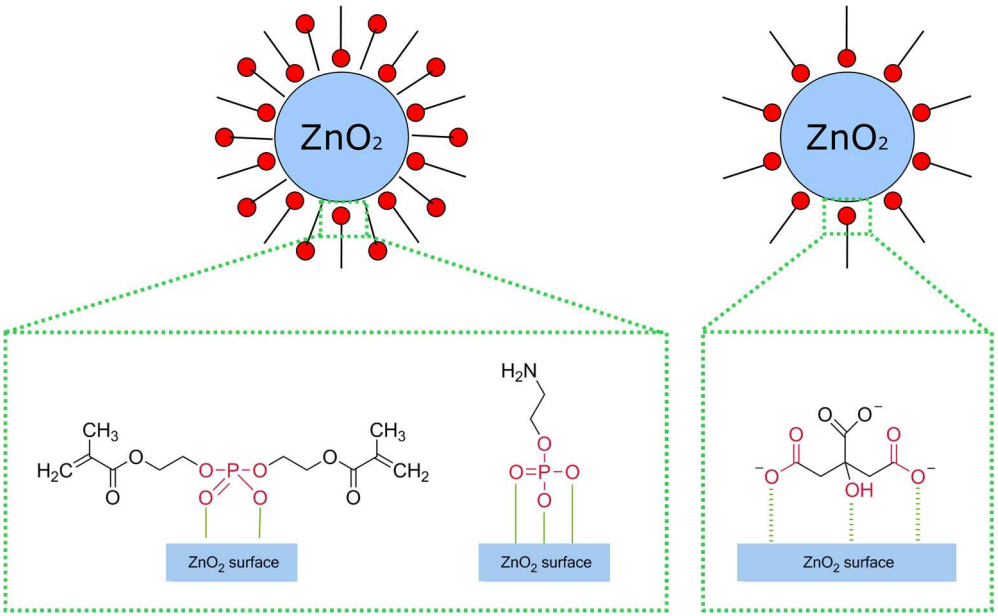

Figure 2.2.11: *Schematic illustration of the interaction between the different stabilizer molecules and the nanoparticle surface leading to stabilizer mono/double layer.*

Further the sample spectrum of the ZnO_2/citrate nanoparticles showed an ampholyte behavior but with significant differences to the reference measurement indicating the immobilization of the citrate molecules on the nanoparticles. The synthesized nanoparticles possessed a maximum negative surface charge of -41.8 mV at a pH value of 10.0 while the zinc peroxide reference only showed a surface charge of -27.4 mV. Additionally the isoelectric point was shifted from pH value 7.8 to 6.1. Furthermore a steeper increase of the zeta potential could be observed for the synthesized nanoparticles at pH values below 4.0. These changes could be

explained through the presence of the citrate. Its carboxylate functions stay mostly deprotonated until a pH value of 4.0 is reached as the p*Ka* values of citrate are 3.14, 4.77 and 6.39.[90] Afterwards all functions are protonated which explains the steeper increase of the surface charge. Also the presence of citrate explains the more negative surface charge compared to the reference. The carboxylate functions are longer negatively charged than the hydroxyl functions on the unmodified zinc peroxide surface. Contrary if the nanoparticles would have been completely decorated with citrate an even more negative surface charge should have been measured. Unmodified areas with hydroxyl functions must be present which can be protonated more easily causing the increase of the zeta potential with decreasing pH value.

The combination of Raman/FTIR and zeta potential measurements showed clearly that the different stabilizer molecules BMEP, *o*-PEA and citrate interacted with the nanoparticles and that in two cases stabilizer double layer were formed around the nanoparticles.

2.2.5 Oxygen Release Properties of ZnO_2 Nanoparticles

Beside the investigations of the nanoparticle morphologies, sizes and surface properties, the oxygen release properties of the different stabilized nanoparticles were particular important. Two different stimuli can be used to trigger the oxygen release from zinc peroxide: increased temperatures (T>190.0 °C, dry state) or slightly acidic environments (pH<7.5, aqueous state). Firstly the temperature induced oxygen release of the ZnO_2/BMEP and ZnO_2/*o*-PEA nanoparticles was investigated. Temperature dependent XRD measurements of the zinc peroxide reference substance revealed, that at temperatures around 200 °C the zinc peroxide was transformed to zinc oxide under elimination of oxygen (Figure 2.2.12a). The diffractogram at 100.0 °C showed only the typical reflexes for zinc peroxide at θ = 31.0, 36.5, 53.0, 63.0, 87.3, 90.3, 101.6 and 110.4°, while the 200.0 °C measurement showed also characteristic reflexes for zinc oxide at θ = 34.9, 48.1, 57.2 and 68.5°.[91] The intensity of these reflexes increased with increasing temperatures, which showed that a higher crystallinity was achieved through higher temperatures in combination with a higher conversion of the zinc peroxide.[91] At the same time a decrease of the intensity of characteristic ZnO_2 reflexes could be observed at θ = 66.8 and 78.3°

which showed the zinc peroxide conversion additionally. The same trend could be observed for the synthesized ZnO_2/BMEP nanoparticles (Figure 2.2.12b). Zinc peroxide was the only species present at 119.0 °C, while zinc oxide occurred at higher temperatures (311.0 and 524.0 °C).

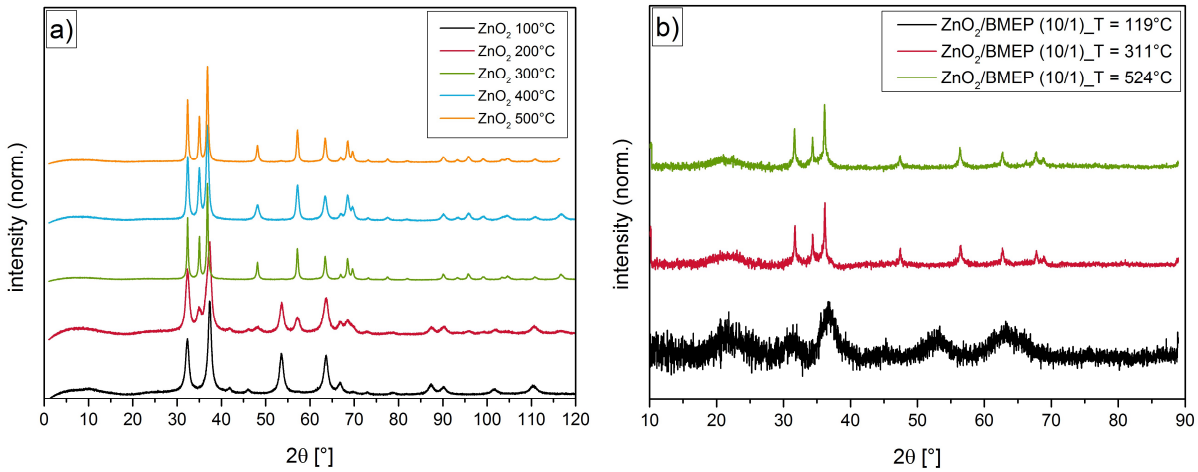

Figure 2.2.12: *Temperature dependent XRD measurements of reference zinc peroxide (a) and synthesized ZnO_2/BMEP nanoparticles (b).*

TG and TG-MS measurements were performed to quantify the amount of the oxygen released upon heating of the different synthesized ZnO_2/BMEP samples and to validate the presence of oxygen during the conversion of zinc peroxide to zinc oxide (Figure 2.2.13, Table 2.2.5). The amount of released oxygen was calculated through the mass loss during the decomposition of zinc peroxide to zinc oxide at 190.0 °C. This detected mass loss could only be contributed to the formed oxygen and could be quantified in relation to the used sample amount (see section 2.2.2). The TG-MS measurements showed that at increased temperatures molecular species with molar masses of 16 and 32 g/mol were released, which indicated clearly that oxygen radicals and oxygen molecules were released during the conversion of the synthesized zinc peroxide to zinc oxide. In addition to this qualitative verification, the quantitative amount of oxygen was calculated.

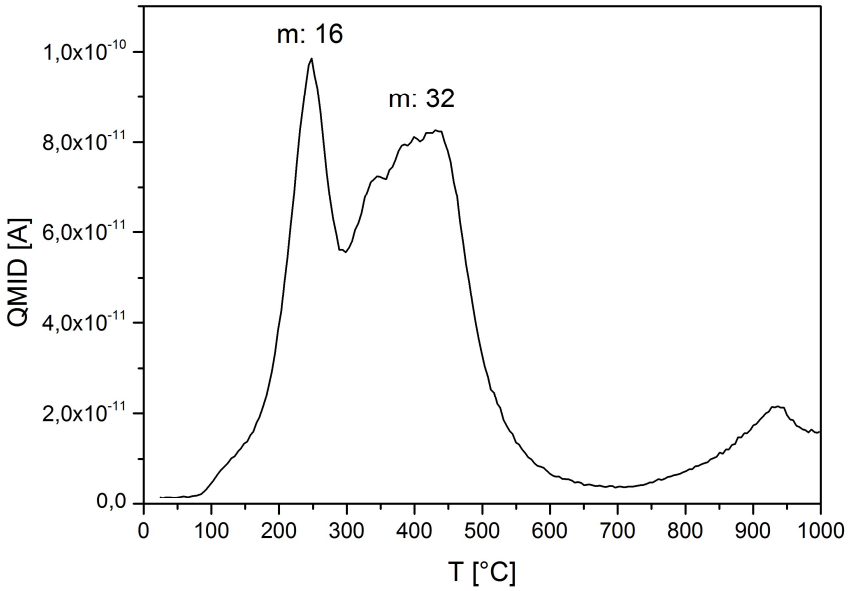

Figure 2.2.13: *TG-MS measurement of a representative ZnO_2/BMEP sample (ZnO_2/BMEP (10/1)_20c(8min)).*

As a general trend an increase of the released oxygen with increasing sample content of zinc peroxide could be investigated. For example the ZnO_2/BMEP (1/1)_20c(8min) sample with a content of 62.3 wt% ZnO_2 released 1.4 mmol oxygen per gram sample, while the ZnO_2/BMEP (10/1)_20c(8min) sample with a content of 78.0 wt% ZnO_2 released 3.9 mmol oxygen per gram sample. In comparison to the zinc peroxide reference only the 1/1 sample released smaller oxygen amount (1.4 compared to 3.5 mmol/g). Nevertheless the 1/1 sample consisted of nanoparticles with a diameter of 7.0±2.0 nm, which should allow a much more homogeneous distribution of the particles compared to the bulk reference, which should result in a much more controllable oxygen release. Beside these investigations, the oxygen release of the nanoparticles prepared at different reaction times was investigated. Due to the fact that all sample had similar compositions (see Table 2.2.5), no significant changes in the amount of oxygen could be detected (1.4 to 1.5 mmol O_2 per gram sample).

The ZnO_2/*o*-PEA nanoparticles showed similar behaviors. The measurements showed that with increasing zinc peroxide content the amount of released oxygen also increased (Table 2.2.5). The lowest oxygen release of 0.9 mmol/g was calculated for the sample with the lowest zinc peroxide content of 18.3 wt% (ZnO_2/*o*-PEA (1/1)_5c(2 min)) while the highest release of 3.9 mmol/g was detected for the sample with the highest ZnO_2 content of 75.5 wt% (ZnO_2/*o*-PEA (10/1)_20c(8 min)). Further the temperature induced oxygen release efficiency of the ZnO_2/*o*-PEA

nanoparticles seemed to be higher compared to the ZnO_2/BMEP nanoparticles. Significantly lower zinc peroxide contents caused comparable oxygen release amounts, which could be explained through the smaller nanoparticle sizes (see Table 2.2.4) compared to the ZnO_2/BMEP nanoparticles.

Table 2.2.5: *Sample compositions and temperature induced oxygen release amounts of zinc peroxide nanoparticles stabilized with BMEP and o-PEA.*

Sample	Sample composition ZnO_2/stabilizer [wt%/wt%]	Oxygen release [mmol O_2/g sample]
ZnO_2/BMEP (1/1)_5c(2min)	65.7/34.3	1.4
ZnO_2/BMEP (1/1)_10c(4min)	63.8/36.2	1.4
ZnO_2/BMEP (1/1)_20c(8min)	62.3/37.7	1.4
ZnO_2/BMEP (1/1)_30c(12min)	61.7/38.3	1.5
ZnO_2/BMEP (5/1)_20c(8min)	71.5/28.5	3.7
ZnO_2/BMEP (10/1)_20c(8min)	78.0/21.9	3.9
ZnO_2/*o*-PEA (1/1)_5c(2 min)	18.3/81.7	0.9
ZnO_2/*o*-PEA (1/1)_10c(4 min)	23.2/76.8	1.2
ZnO_2/*o*-PEA (1/1)_20c(8 min)	26.6/73.4	1.4
ZnO_2/*o*-PEA (5/1)_20c(8 min)	68.1/31.9	3.5
ZnO_2/*o*-PEA (10/1)_20c(8 min)	75.5/24.5	3.9
ZnO_2 reference	100/0	3.5

Additionally the pH induced oxygen release of the BMEP, *o*-PEA and citrate stabilized zinc peroxide nanoparticles in aqueous media was investigated. Zinc peroxide dissociates in aqueous acidic media into zinc ions and hydrogen peroxide, while the formed hydrogen peroxide dissociates into water and oxygen in presence of metal salts and metal oxide surfaces, given by the nanoparticle itself.[59,60] The quantifications of the released oxygen were done by long time measurements (approximately six days) under an inert argon atmosphere, to make sure that the measured amount of oxygen could not be distorted by atmospheric oxygen. Additionally, a pure water reference measurement was performed under identical conditions. The obtained data were used as a baseline measurement and were subtracted from all following measurement data. The measurements itself were carried out with an optical oxygen sensor at different pH values in degassed aqueous media (pH = 8.5, 7.5, 6.5) and at room temperature (T = 23 to 24 °C) (Figure 2.2.14).

The measurements showed clearly the long time oxygen release properties of zinc peroxide. All samples, including the zinc peroxide reference showed an activity for at least three and a half days, recognizable at the saturation curves. The measurement solutions were degassed and kept under an argon atmosphere to ensure that nearly no oxygen is present at the measurement start. Afterwards the nanoparticles released constantly oxygen which concentrated in the measurement solution until the nanoparticles became inactive which caused the plateau beginning after four days. The comparison with literature values proved that the plateau can only be caused through the nanoparticle inactivity due to the fact that the maximum concentration of dissolved oxygen in water was not reached at the end of the measurements (8.7 to 8.4 mg/L at 23 to 24 °C).[92]

Beside the long time release properties, it was possible to observe a dependence of the amount of released oxygen to the sample compositions, the nanoparticle sizes and the pH values of the used media. Figure 2.2.14a shows the dependence of the released oxygen to the sample compositions and the nanoparticle sizes at a constant pH value of 6.5 for the ZnO_2/BMEP nanoparticles. It could be proven that the sample ZnO_2/BMEP (5/1)_20c(8 min) showed the highest oxygen release of the three compared samples of approximately 2.21 mg/L, which fits to the expectations due to the fact that this sample consisted of the smallest nanoparticles (3.3±0.9nm, Table 2.2.4) resulting in the highest surface activity. Additionally the percentage amount of zinc peroxide of this sample was relatively high at 71.5 wt% (Table 2.2.5) which provided a high oxygen release too. In contrast to that the other two samples 1/1 and 10/1 showed a similar behavior like the measured bulk zinc peroxide reference. The amount of released oxygen of the sample 1/1 was 0.83 mg/L while the release of the reference substance was 0.93 mg/L. This coincidence could be explained by the sample composition. The sample 1/1 consisted indeed of small uniform nanoparticles (7.2±2.0nm, Table 2.2.4) which should have resulted in a much higher oxygen release compared to the bulk zinc peroxide reference, but the amount of zinc peroxide was only 62.3 wt% (Table 2.2.5) which limited the oxygen release of this sample. A similar explanation could be found for the 10/1 sample. This sample should have shown a lower release compared to the 1/1 sample due to its lower surface activity caused by bigger particles (11.5±3.6nm, Table 2.2.4) but the higher amount of zinc peroxide (78.0 wt%, Table 2.2.5) compensated this disadvantage resulting in a oxygen release of 1.15 mg/L. These data showed clearly that the

oxygen release depends on both the sample composition and the nanoparticle sizes and can be controlled by both factors.

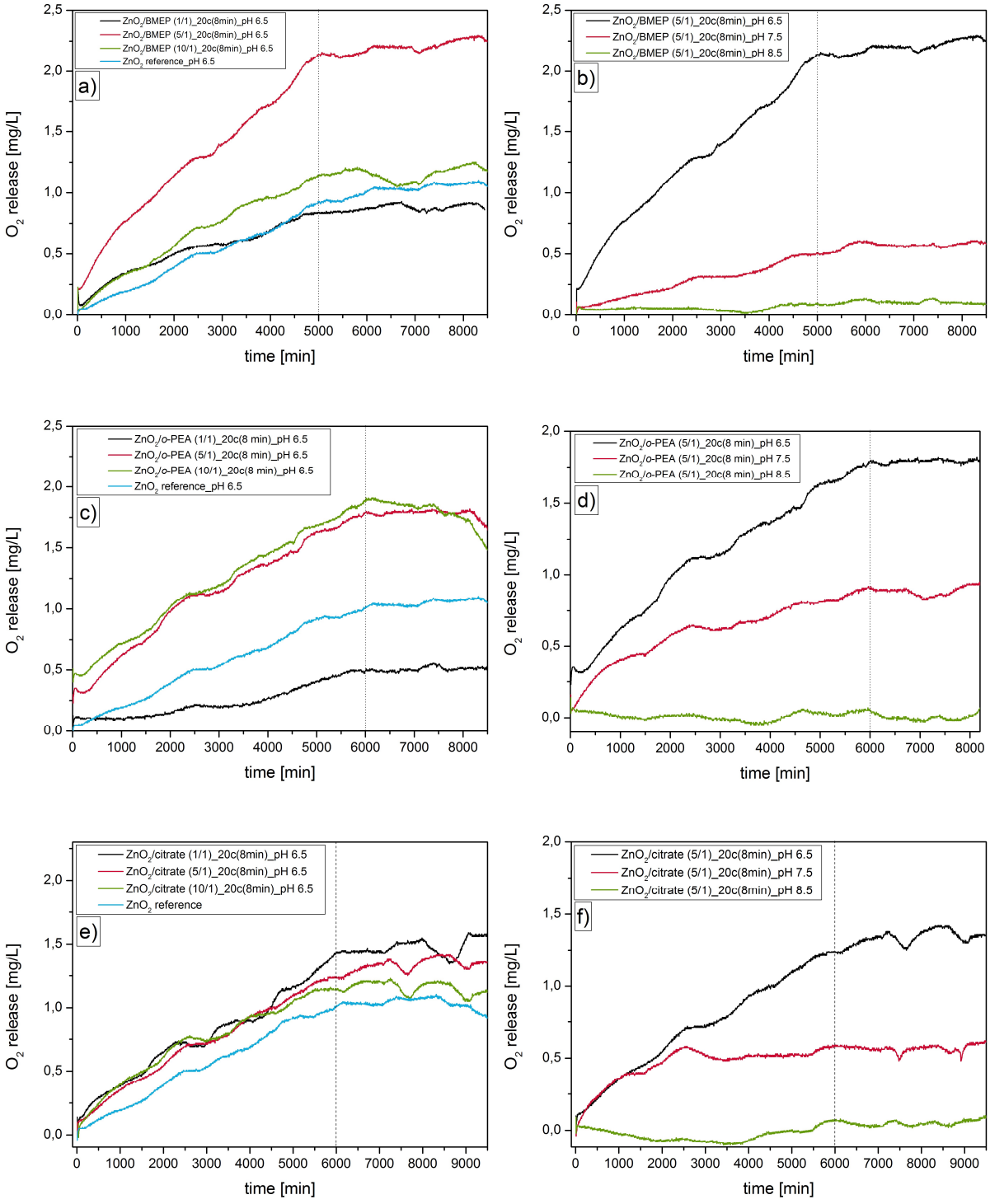

Figure 2.2.14: *Time dependent, pH induced oxygen release measurements in aqueous media: a) different BMEP samples at constant pH value 6.5; b) one BMEP sample at different pH values (6.5, 7.5 and 8.5); c) different o-PEA samples at constant pH value; d) one o-PEA sample at different pH values; e) different citrate samples at constant pH value and f) one citrate sample at different pH values.*

The *o*-PEA stabilized nanoparticles showed the same trends (Figure 2.2.14c). The sample ZnO_2/*o*-PEA (1/1)_20c(8 min) reached a maximum oxygen concentration of 0.49 mg/L while the sample ZnO_2/*o*-PEA (5/1)_20c(8 min) already reached an oxygen amount of 1.79 mg/L at a pH value of 6.5. This increase was caused through the higher zinc peroxide content of the sample 5/1 (68.1 wt%) compared to the 1/1 (26.6 wt%) sample. Furthermore sample 5/1 consisted of smaller and more uniform nanoparticles (2.4±0.7 nm) compared to the 1/1 sample (3.9±1.2 nm) which resulted in a higher surface activity. Compared to this strong oxygen release increase the difference between the samples 5/1 and 10/1 was nearly negligible. The amount of released oxygen increased from 1.79 to 1.89 mg/L. Due to the higher zinc peroxide amount of sample 10/1 (75.5 wt%) compared to sample 5/1 a more significant increase was expected. An explanation for the minor increase was that the sample consisted of slightly bigger particles (3.3±1.0 nm) compared to the 5/1 sample resulting in a minor activity.

Table 2.2.6: *pH induced oxygen release amounts in aqueous media for the BMEP, o-PEA and citrate stabilized zinc peroxide nanoparticles.*

Sample	Oxygen release [mg/L]
ZnO_2/BMEP (1/1)_20c(8 min)_pH 6.5	0.83
ZnO_2/BMEP (5/1)_20c(8 min)_pH 6.5	2.21
ZnO_2/BMEP (10/1)_20c(8 min)_pH 6.5	1.15
ZnO_2/BMEP (5/1)_20c(8 min)_pH 7.5	0.50
ZnO_2/BMEP (5/1)_20c(8 min)_pH 8.5	0.00
ZnO_2/*o*-PEA (1/1)_20c(8 min)_pH 6.5	0.49
ZnO_2/*o*-PEA (5/1)_20c(8 min)_pH 6.5	1.79
ZnO_2/*o*-PEA (10/1)_20c(8 min)_pH 6.5	1.89
ZnO_2/*o*-PEA (5/1)_20c(8 min)_pH 7.5	0.91
ZnO_2/*o*-PEA (5/1)_20c(8 min)_pH 8.5	0.06
ZnO_2/citrate (1/1)_20c(8min)_pH 6.5	1.50
ZnO_2/citrate (5/1)_20c(8min)_pH 6.5	1.36
ZnO_2/citrate (10/1)_20c(8min)_pH 6.5	1.21
ZnO_2/citrate (5/1)_20c(8min)_pH 7.5	0.58
ZnO_2/citrate (5/1)_20c(8min)_pH 8.5	0.06
ZnO_2 reference_pH 6.5	0.93

Furthermore the samples 5/1 and 10/1 showed a significant higher oxygen release compared to the macroscopic zinc peroxide reference (maximum value 0.93 mg/L) indicating again the superiority of the synthesized nanoparticles over commercial available zinc peroxide. Only the 1/1 sample revealed a lower oxygen release which could be explained though its low zinc peroxide amount caused through the high stabilizer amount.

Also the citrate stabilized nanoparticles showed partly the already observed correlation between the sample composition and the amount of released oxygen (Figure 2.2.14e). Maximum oxygen concentrations of 1.50 (ZnO_2/citrate (1/1)_20c(8min)), 1.36 (ZnO_2/citrate (5/1)_20c(8min)) and 1.21 mg/L (ZnO_2/citrate (10/1)_20c(8min)) could be observed. It was shown that the samples 5/1 and 10/1 released nearly the same amount of oxygen. This behavior was explained through the similar zinc peroxide contents of 64.9 and 61.5 wt% of these two samples. Contrary the 1/1 sample showed an unexpected high oxygen release of 1.50 mg/L while it's relatively low zinc peroxide content of 14.1 wt% should have resulted in a lower oxygen release compared to the 5/1 and 10/1 sample.

Beside the investigated control through the sample compositions and particle sizes the adjustment of the pH value of the dispersion solution could influence the oxygen release too. The Figures 2.2.14b, d and f show that with increasing pH value the oxygen release decreased constantly. It was possible to achieve oxygen release amounts of 2.21 (BMEP), 1.79 (*o*-PEA) and 1.36 (citrate) mg/L at pH 6.5 while the release decreased to approximately 0.00 (BMEP), 0.06 (*o*-PEA) and 0.06 (citrate) mg/L at pH value 8.5. This fulfilled the expectations because an acidic media is necessary to start the decomposition of the zinc peroxide, which induces the oxygen release.[59,60]

2.2.6 Summary

The zinc peroxide nanoparticles were stabilized and functionalized in aqueous media with the stabilizer molecules BMEP, *o*-PEA and citrate. As proved by Raman/FTIR and pH dependent zeta potential measurements the phosphate function of the BMEP and *o*-PEA molecules interacted with the zinc peroxide surface, forming covalent P-O-Zn bonds, while the carboxylate functions of the citrate mostly physisorbed on the

nanoparticle surface. Beside that the BMEP and *o*-PEA formed a double layer around the zinc peroxide nanoparticles, according to the pH dependent zeta potential measurements, resulting in an additional electrostatic stabilization of the nanoparticles in aqueous solution. The terminal methacrylate groups of the BMEP, the amine functions of the *o*-PEA and the free carboxylate functions of the citrate attached to the nanoparticle surface could be used for further post-modifications.

The sizes of the nanoparticles could be controlled by different cycle numbers (reaction times) and $Zn(ac)_2$:stabilizer ratios. It was possible to control the size of the ZnO_2/BMEP nanoparticles between 3.9±1.2 and 14.4±5.2 nm by varying the cycle numbers between five and thirty (reaction times between 2 min and 12 min). The variation of the size and standard deviations could be contributed to the longer exposition of the particles to the shear and impact forces within the reaction chamber and to the occurrence of Ostwald ripening. Different zinc acetate:BMEP ratios afflicted the nanoparticle diameter too. By increasing the precursor concentration from $8.58 \cdot 10^{-4}$ mol/L to $4.90 \cdot 10^{-3}$ mol/L at a constant stabilizer concentration, it was possible to tune the nanoparticle diameter from 3.3±0.9 to 11.5±3.6 nm. This dependence was caused by a change in the supersaturation of the reaction solution which influenced the particle growth.

Contrary the ZnO_2/*o*-PEA nanoparticles showed no significant size changes during parameter variation. Small and uniform nanoparticles with diameters between 2.4±0.7 and 3.9±1.2 nm were obtained depending on different zinc acetate:*o*-PEA ratios (1/1, 5/1 and 10/1) and reaction times (2, 4 and 8min).

The ZnO_2/citrate nanoparticles showed similar trends like the ZnO_2/BMEP nanoparticles. It could be shown that with increasing reaction time from 8min to 16min the nanoparticle sizes increased from 6.5±1.6 to 10.6±6.7 nm. Furthermore the decrease of the stabilizer concentration did also result in more irregular nanoparticles (from 6.5±1.6 to 7.3±3.1 nm) which could be explained through a more insufficient stabilization.

Crystallite size determinations via the Debye Scherrer equation supported the assumptions made by TEM images. Crystallite sizes between 2.4±0.0 and 3.6±0.6 nm could be calculated which indicated that the synthesized nanoparticles consisted mostly of two to four crystallites each.

Another essential point was the investigation of the oxygen release properties of the zinc peroxide nanoparticles. Temperature and pH could be used to trigger the oxygen release from zinc peroxide nanoparticles. TGA, TGA-MS, and temperature dependent XRD measurements revealed that the temperature induced oxygen release from dry zinc peroxide nanoparticles started at temperatures between 190 and 200 °C and showed a clear dependence from the sample compositions. The amount of released oxygen increased from 1.8 to 3.9 mmol oxygen per gram sample with increasing sample amount of zinc peroxide from 62.3 to 78.0 wt% for the BMEP stabilized nanoparticles. Simultaneously the temperature induced oxygen release of the ZnO_2/*o*-PEA nanoparticles increased from 0.9 to 3.9 mmol O_2/g sample with increasing zinc peroxide sample content from 18.3 to 75.5 wt%.

Furthermore pH dependent oxygen release measurements in aqueous media showed that a long time oxygen release could be achieved. The particles released oxygen continuously for approximately for days depending on the type of stabilizer. Additionally the amount of released oxygen was dependent on the sample composition, the particle sizes and the pH value of the dispersion. For example released the ZnO_2/BMEP nanoparticles oxygen amounts between 2.21 and 0.83 mg/L with increasing zinc peroxide content from 62.3 to 78.0 wt% and decreasing particle sizes. Further the ZnO_2/*o*-PEA nanoparticles showed similar trends. The amount of released oxygen increased from 0.49 to 1.89 mg/L with increasing zinc peroxide sample amount from 26.6 to 75.5 wt%. Contrary the ZnO_2/citrate nanoparticles with the lowest zinc peroxide content of 14.1 wt% induced the highest oxygen amount of 1.50 mg/L. Additionally the dependence of the oxygen release on the pH value of the dispersion media could be proven. A constantly oxygen concentration decrease from 2.21 (BMEP), 1.79 (*o*-PEA) and 1.36 (citrate) mg/L to 0.00 (BMEP), 0.06 (*o*-PEA) and 0.06 (citrate) mg/L could be measured through the pH increase from 6.5 to 8.5.

2.3 Synthesis of ZnO_2 Nanoparticles in Organic Media

2.3.1 Introduction

Beside the already discussed zinc peroxide nanoparticle syntheses carried out in aqueous media, also one synthesis in organic media was established. This chapter discusses the synthesis of ZnO_2 nanoparticles from zinc acetate in methanol. The synthesis was performed in a flask instead of the high pressure impinging jet reactor due to the stronger precipitation of the product during the synthesis which could have clogged the reaction chamber of the reactor. The nanoparticles were stabilized and functionalized in situ with dioctyl sulfosuccinate (AOT; Figure 2.3.1). This molecule consists of a sulfonate head group to which two branched alkane chains are attached via an ester group.

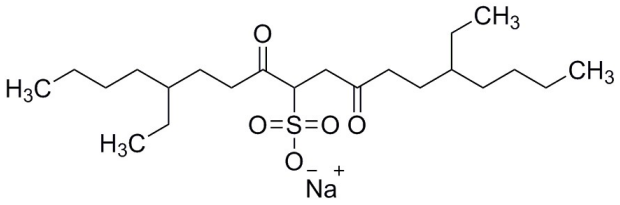

Figure 2.3.1: *Chemical structure of the stabilizing agent dioctyl sulfosuccinate (AOT).*

The sulfonate head group should interact with the nanoparticle surface while the branched alkane chains should induce a sterical stabilization of the zinc peroxide leading to small and uniform nanoparticles. Furthermore the AOT should support the redispersibility of the nanoparticles in organic media. Normally AOT is used as an emulsifier during the synthesis of nanomaterials. Due to its polar head and its unpolar tails it is highly capable of forming microemuslions consisting of for example water and *n*-heptane. The corresponding nanoparticle precursors and precipitation agents are solved in two separate water phases and can only react when two water droplets attract each other. The size of the resulting nanoparticle is then determined through the water droplet size.[93] For example nanomaterials consisting of CeO_2, copper (Cu) or silver (Ag) were synthesized via AOT stabilized microemulsions.[94–96]

2.3.2 Chemical Structure of ZnO_2 nanoparticles

The influence of different nanoparticle precursor ($Zn(ac)_2$) to stabilizer (AOT) ratios on properties like crystal structure, sample composition, precursor conversion,

nanoparticle diameter and oxygen release properties were investigated. Synthesis ratios of 5/1, 10/1, 20/1 and 30/1 were tested and investigated. X-Ray diffraction measurements revealed the characteristic reflexes of the cubic crystal structure of zinc peroxide at 2θ = 31.7° (110), 37.0° (200), 53.0° (220) and 63.1° (311) in comparison with the reference measurement (Figure 2.3.2a).[54,62]

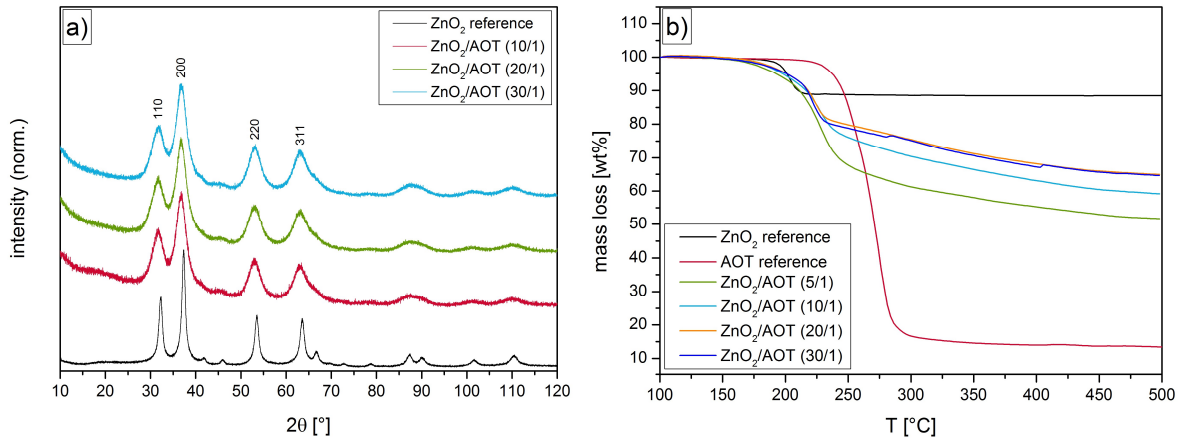

Figure 2.3.2: *X-Ray diffraction measurements of zinc peroxide nanoparticles stabilized with AOT in comparison to zinc peroxide reference measurements (a); thermogravimetric measurements of the different zinc peroxide nanoparticles stabilized with AOT in comparison to reference measurements of zinc peroxide and AOT (b).*

The measurements indicated the presence of zinc peroxide for all synthesized samples beside the sample ZnO_2/AOT (5/1). No convincing XRD measurements could be performed for this sample due to its higher stabilizer content (see Table 2.3.1) which disturbed the measurement resulting in suppressed reflexes. Nevertheless TEM measurements (see section 2.3.3) showed the presence of nanoparticles which allowed the assumption that zinc peroxide was formed for sample ZnO_2/AOT (5/1) too. Furthermore broadened reflexes could be detected which proved the formation of nanoparticles. Crystallite size calculations based on the Debye Scherrer equation revealed sizes between 2.7±0.1 and 3.2±0.1 nm indicating small and uniform nanoparticles (detailed size discussion see section 2.3.3).[78,79]

Beside the influence of the different precursor:AOT ratios on the crystal structure also the influence on the sample composition and the precursor conversion was investigated. Thermogravimetric measurements (TGA) showed that with decreasing initial stabilizer concentration the sample stabilizer content continuously decreased too, which was in line with the expectations (Figure 2.3.2b, Table 2.3.1). For example was a sample stabilizer content of 45.5 wt% (ZnO_2/AOT (5/1)) achieved for an initial

stabilizer concentration of $1.9 \cdot 10^{-3}$ mol/L while only a stabilizer content of 28.0 wt% (ZnO_2/AOT(30/1)) could be measured at an initial stabilizer concentration of $3.2 \cdot 10^{-4}$ mol/L. The decrease showed that a control of the sample composition was possible by varying the educt concentrations but not fully predictable. For example should the stabilizer content of the 5/1 sample have been six times higher than the stabilizer content of the 30/1 sample. An explanation could be that the initial applied amount of AOT was too high for the synthesis approach 5/1. The data suggest that a smaller stabilizer amount was sufficient for the nanoparticle stabilization and that the abundant AOT was removed during the cleaning process.

Table 2.3.1: *Sample compositions and precursor conversions for the different zinc peroxide nanoparticle samples stabilized with AOT determined through thermogravimetric measurements.*

Sample	Synthesis ratio $Zn(ac)_2$/AOT	Sample composition [wt%/wt%]	Conversion $Zn(ac)_2$ [%]
ZnO_2/AOT (5/1)	5/1	54.5/45.5	46.8
ZnO_2/ AOT (10/1)	10/1	62.6/37.4	37.3
ZnO_2/ AOT (20/1)	20/1	67.5/32.5	52.5
ZnO_2/ AOT (30/1)	30/1	72.0/28.0	47.0

Contrary to the investigated correlation between the zinc acetate:AOT ratio and the sample composition no clear trend could be observed for the conversion of the nanoparticle precursor zinc acetate. Moderate conversions between 37.3 and 52.0 % could be calculated based on the zinc peroxide content of the different samples, the product yield and the applied amount of zinc acetate. The non existing trend could maybe be explained through the stronger product precipitation during the reaction. This could cause difficulties during the cleaning process which could influence the product yield and consequently the calculated precursor conversion.

The sample compositions and the corresponding conversions were determined based on the different thermal decomposition steps measured via TGA. The reference measurements for zinc peroxide and AOT showed that zinc peroxide decomposed between 193.0 and 210.0 °C while AOT decomposed in a temperature range of 220.0 to 315.0 °C. The identification of these two separate decompositions enabled the separation of the different decomposition steps of the synthesized samples like for the already discussed nanoparticle systems. Sample ZnO_2/AOT (5/1) showed a first decomposition step in a temperature range of 179.6 to 202.3 °C,

sample ZnO_2/AOT (10/1) between 176.9 and 208.1 °C, sample ZnO_2/AOT (20/1) between 177.7 and 204.8 °C and sample ZnO_2/AOT (30/1) between 178.3 and 219.3 °C. These decomposition steps could be assigned to zinc peroxide present in the samples and consequently to their zinc peroxide sample content. The shift of the decomposition start to smaller temperatures could be explained through the presence of nanoparticles which can be more easily decomposed than the bulk zinc peroxide. The following relatively broad decomposition step up to approximately 450.0 °C could then only be ascribed to the AOT content of the different samples.

2.3.3 Size and Morphology of ZnO_2 nanoparticles

Beside the influence of the precursor:stabilizer ratio on the sample composition and the conversion of the nanoparticle precursor also the influence on the size and morphology of the obtained zinc peroxide nanoparticles was investigated. The already discussed broadened XRD reflexes gave first evidence of the presence of nanoparticles. TEM measurements were performed to validate this assumption. Each sample was investigated via measuring over 100 nanoparticles and the calculation of the corresponding standard deviations (Figure 2.3.3, Table 2.3.2).

Table 2.3.2: *Nanoparticle diameter and crystallite sizes for the zinc peroxide nanoparticles stabilized with AOT determined via transmission electron microscopy and X-Ray diffractometry.*

Sample	Particle diameter [nm] (TEM)	Crystallite sizes [nm] (XRD)
ZnO_2/AOT (5/1)	6.1±2.9	---
ZnO_2/AOT (10/1)	2.1±0.6	3.2±0.2
ZnO_2/AOT (20/1)	8.4±2.3	2.7±0.1
ZnO_2/AOT (30/1))	10.7±3.0	2.8±0.1

The TEM images showed small and relatively uniform nanoparticles for all synthesized samples. Additionally an influence of the precursor:stabilizer ratios on the nanoparticle sizes could be investigated. The nanoparticle diameter decreased from 6.1±2.9 to 2.1±0.6 nm with decreasing stabilizer concentration from $1.9 \cdot 10^{-3}$ (5/1) to $9.4 \cdot 10^{-4}$ mol/L (10/1). This size decrease could be explained through a higher local supersaturation of the precursor caused through fewer stabilizer molecules present in the reaction solution. A higher supersaturation induces an exponential

growth of the nucleation rate of the nanoparticles leading to smaller and more uniform particles like already observed for example for the BMEP stabilized nanoparticles.[32] Especially the decrease of the calculated standard deviation form ±2.9 to ±0.6 nm supported this assumption. A further decrease of the initial stabilizer concentration to $4.9 \cdot 10^{-4}$ (20/1) or $3.2 \cdot 10^{-4}$ mol/L (30/1) contrary led to bigger particles with diameter of 8.4±2.3 and 10.7±3.0 nm. This increase indicated that not sufficient enough stabilizer was present compared to sample 10/1 to prevent the nanoparticles fully from aggregation and Ostwald ripening during the nucleation and growth rate. This led to bigger and more irregular particles which could be also proven through the increasing standard deviations.[23]

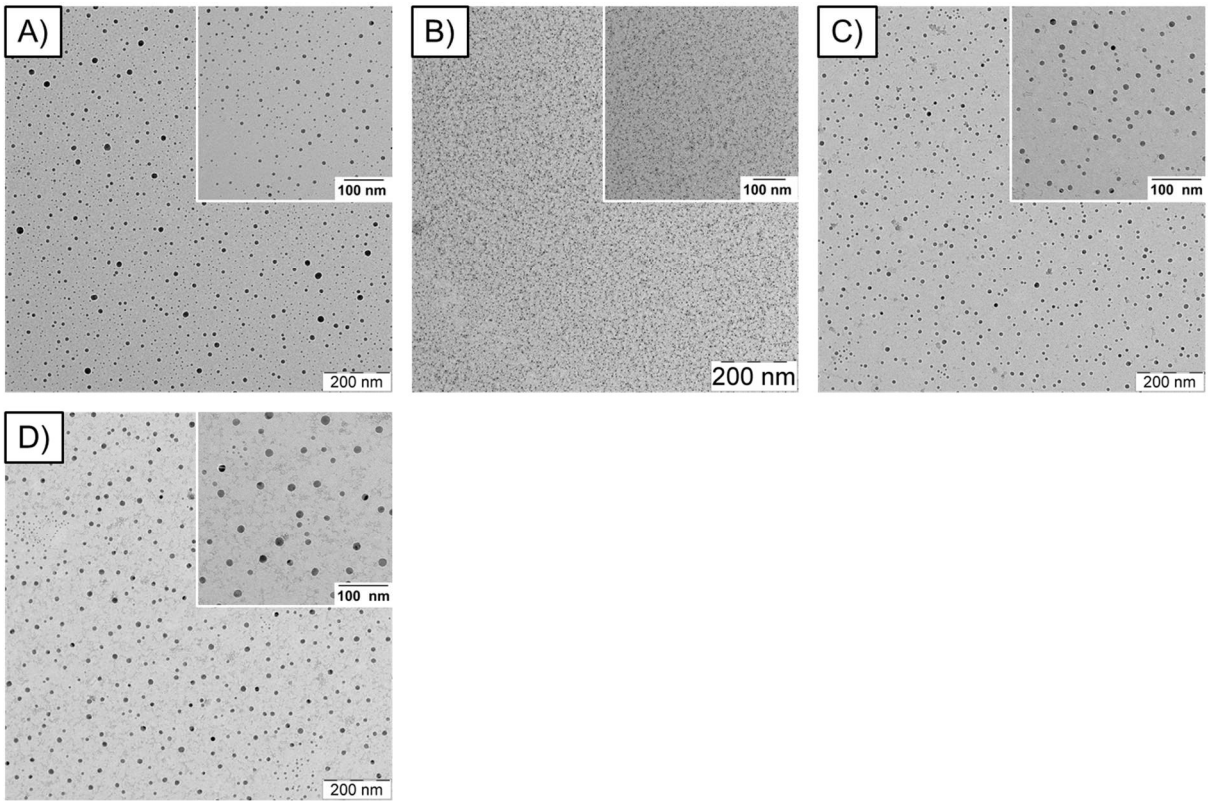

Figure 2.3.3: *Transmission electron microscopy images of the different zinc peroxide nanoparticle samples stabilized with AOT: ZnO_2/AOT (5/1) (A), ZnO_2/AOT (10/1) (B), ZnO_2/AOT (20/1) (C) and ZnO_2/AOT (30/1) (D).*

Furthermore the crystallite size calculations based on the FWHM radian of the reflexes 220 and 311 and the Debye Scherrer equation supported the TEM measurements. The crystallite sizes for the samples 20/1 and 30/1 of 2.7±0.1 and 2.8±0.1 nm indicated that the synthesized nanoparticles most probably consisted of two, three or four crystallites each. Additionally the crystallite standard deviations were very small showing a controlled nanoparticle crystal growth. Only the crystallite

size of sample 10/1 (3.2±0.2 nm) did not completely fit to the measured nanoparticle sizes (2.1±0.6 nm). This deviation could probably be assigned to a measurement error due to the fitting of all already discussed nanoparticle size discussions.

2.3.4 Chemical Composition of ZnO_2 Nanoparticles Surface

The size investigations via TEM and XRD measurements showed that nanoparticles could be synthesized for all synthesis approaches. This indicated that the stabilizer molecule AOT must have interacted with the zinc peroxide surface resulting in its stabilization. FTIR and pH dependent zeta potential measurements were performed to investigate and to prove this interaction. One representative sample (ZnO_2/AOT (30/1)), unmodified zinc peroxide and pure AOT were measured and the differences between the measurements examined (Figure 2.3.4).

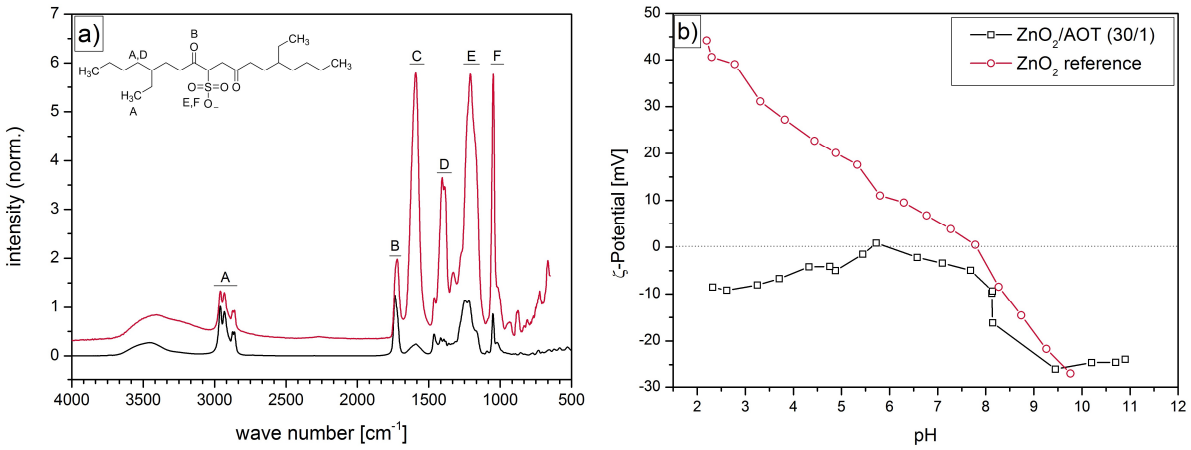

Figure 2.3.4: *FTIR spectra of the ZnO_2/AOT (30/1) sample (black) and the AOT reference substance (red) (a); pH dependent zeta potential measurements for the ZnO_2/AOT (30/1) sample (black) and a ZnO_2 reference substance (red).*

Figure 2.3.4a shows the FTIR spectra of the sample ZnO_2/AOT (30/1) and the reference substance AOT. The detected bands could be attributed to the different chemical groups of AOT. For example were the bands between 2963 and 2787 cm^{-1} characteristic for the asymmetric and symmetric stretching vibrations of the alkyl chain functions (-CH_3, -CH_2-; signal A) while the band at 1719 cm^{-1} could be assigned to the asymmetric stretching vibration of the carbonyl function of the alkyl chains (C=O; signal B). Additionally signal D (1402 cm^{-1}) could also be attributed to the –CH_2- function. Furthermore the detected signals at 1215 and 1049 cm^{-1} (signal E and F) were caused through the asymmetric and symmetric stretching vibration of

sulfonate head group (S-O and S=O) of the AOT.[97–100] Signal B showed no differences to the reference measurement indicating that no interaction took place between the zinc peroxide surface and the carbonyl group of the AOT. Contrary the intensity of signal D decreased significantly. This could be caused through a change of the alkyl chain orientation through the interaction of the AOT with the nanoparticles. Due to the limited available space on the nanoparticle surface a dense packing of the stabilizer could result in an approaching of the two chains of each molecule. Also signal E and F showed strong intensity decreases. This could indicate that the polar sulfonate head function of the AOT interacted with the nanoparticle surface. Previous studies postulated that sulfonates interact with metal oxides through dipole interactions (physisorption) which could be assumed for the AOT stabilized zinc peroxide nanoparticles too.[101]

To validate the assumption that the AOT interacted with the nanoparticles pH dependent zeta potential measurements were performed for the ZnO_2/AOT (30/1) sample and unmodified zinc peroxide (Figure 2.3.4b). The measured significant surface charge change of the synthesized nanoparticles (black) compared to the zinc peroxide reference (red) suggested the immobilization of the AOT and supported the FTIR measurements. A maximum positive surface charge of 44.1 mv (pH value of 2.0) could be measured for the unmodified zinc peroxide while a value of -8.7 mV was achieved for the AOT modified zinc peroxide nanoparticles at same measurement conditions. Additionally the synthesized nanoparticles showed a slight increase of the surface charge (from -8.7 to 0.1 mV) with increasing pH value from 2.0 to 5.7 followed by a continuously surface charge decrease (from 0.1 to -26.1 mV) in a pH range from 5.7 to 9.5. These observations could indicate the formation of an AOT double layer around the nanoparticles like for the BMEP and *o*-PEA stabilized nanoparticles (see section 2.2.4). The first layer would interact with the nanoparticle surface through its sulfonate functions (see FTIR discussion) and its branched alkyl chains could interact with the dispersion solvent. Contrary the alkyl chains of the second layer would be directed towards the nanoparticle surface while its sulfonate functions would be directed towards the solvent. These outer sulfonate functions could be deprotonated in basic media resulting in a negative surface charge and could be protonated in acidic media resulting in a neutral surface charge.[102] The observed surface charges fitted to this assumption with exception of the slightly negative surface charge in acidic environment. This deviation could be explained

through titration errors of the used auto titrator due to concentration gradients in the measurement dispersion.

2.3.5 Oxygen Release Properties of ZnO_2 Nanoparticles

The temperature and pH induced oxygen release of the AOT stabilized zinc peroxide nanoparticles was investigated via thermogravimetric analysis and long time release measurements in aqueous solution. TGA measurements revealed that the synthesized zinc peroxide nanoparticles started to decompose at temperatures of approximately 180.0 °C (see section 2.3.2) under elimination of specific amounts of oxygen (Table 2.3.3). The temperature induced oxygen release was quantified through the identification and quantification of the decomposition step at this temperature.

Table 2.3.3: *Temperature induced oxygen release amounts of the AOT stabilized zinc peroxide nanoparticles.*

Sample	Oxygen release [mmol O_2/g sample]
ZnO_2/AOT (5/1)	2.1
ZnO_2/AOT (10/1)	2.3
ZnO_2/AOT (20/1)	1.8
ZnO_2/AOT (30/1)	2.7

The measurements showed that a dependence of the oxygen release on the sample composition could be achieved. The amount increased from 2.1 (5/1) to 2.7 mmol O_2/g sample (30/1) with increasing zinc peroxide sample content from 54.5 to 72.0 wt% which was in line with the expectations. Only sample ZnO_2/AOT (20/1) showed a minor oxygen release of 1.8 mmol O_2/g sample compared to the other samples. The measurement was repeated twice to minimize measurement errors but similar oxygen values could be calculated.

Furthermore the pH induced oxygen release was investigated too. The measurements were performed in degassed aqueous dispersion at different pH values (6.5, 7.5 and 8.5), under argon atmosphere and at room temperature similar to the already discussed nanoparticle samples (Figure 2.3.5, Table 2.3.4). The release lasted for approximately five days for most samples, beside sample ZnO_2/AOT (30/1) which release only lasted for 3.5 days. Figure 2.3.5a shows the

continuous measurements for different synthesized samples at constant pH value of 6.5. It could be proven again that the amount of released oxygen was dependent on the different nanoparticle diameter and the different sample compositions.

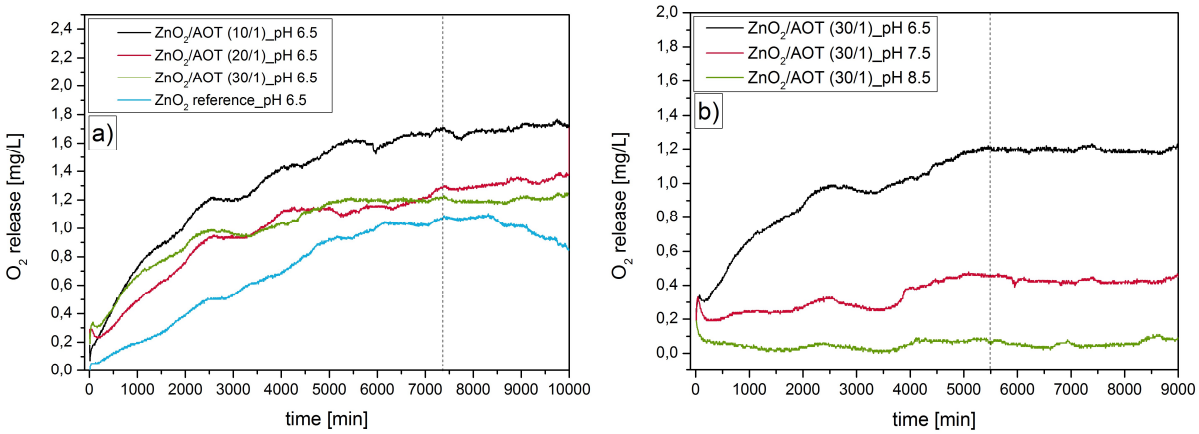

Figure 2.3.5: *Oxygen release measurements for different AOT stabilized samples at constant pH value (a) and pH dependent oxygen release measurements for one sample (b).*

For example showed sample ZnO_2/AOT (10/1) the highest oxygen release of 1.69 mg/L oxygen while the samples ZnO_2/AOT (20/1) and ZnO_2/AOT (30/1) induced nearly similar oxygen amounts of 1.29 and 1.21 mg/L. The increased release of sample 10/1 could be explained through the significant smaller nanoparticles (2.1±0.6 nm) compared to the samples 20/1 (8.4±2.3 nm) and 30/1 (10.7±3.0 nm) which resulted in an increased surface activity. Following this explanation sample 20/1 should have released much more oxygen than sample 30/1. The observed contrary behavior was caused through the different zinc peroxide sample contents of 67.5 (20/1) and 72.0 wt% (30/1) which compensated the nanoparticle differences of this two samples which resulted in nearly similar oxygen release amounts. Additionally all AOT stabilized nanoparticles released more oxygen than the macroscopic zinc peroxide reference which proved their superior oxygen release properties.

Table 2.3.4: *pH induced oxygen release amounts of the AOT stabilized nanoparticles at different sample compositions and pH values.*

Sample	Oxygen release [mg/L]
ZnO_2/AOT (10/1)_pH 6.5	1.69
ZnO_2/AOT (20/1)_pH 6.5	1.29
ZnO_2/AOT (30/1)_pH 6.5	1.21
ZnO_2/AOT (30/1)_pH 7.5	0.45
ZnO_2/AOT (30/1)_pH 8.5	0.06
ZnO_2 reference_pH 6.5	0.93

Furthermore the influence of different pH values on the oxygen releasing properties of one representative sample (ZnO_2/AOT (30/1)) was investigated too (Figure 2.3.5b). It could be shown that the oxygen release decreased constantly from 1.21 to 0.06 mg/L with increasing pH value from 6.5 to 8.5. This was in line with the already investigated nanoparticle syntheses and proved again that a slightly acidic environment triggered the oxygen release.[59,60]

2.7.6 Summary

Zinc peroxide nanoparticles stabilized with dioctyl sulfosuccinate (AOT) were successfully synthesized. The synthesis was carried out in methanol at 100 °C in a flask for one hour. Different initial precursor:stabilizer ratios of 5/1, 10/1, 20/1 and 30/1 ($Zn(ac)_2$/AOT) were tested and their influence on properties like crystal structure, sample composition, precursor conversion, nanoparticle size and oxygen release properties investigated.

TEM measurements proved that small nanoparticles could be obtained for all synthesis approaches. Furthermore a dependence of the nanoparticle size on the zinc acetate:AOT ratio could be observed. The diameter decreased from 6.1±2.9 to 2.1±0.6 nm with decreasing stabilizer concentration from $1.9 \cdot 10^{-3}$ (5/1) to $9.4 \cdot 10^{-4}$ mol/L (10/1). This decrease could be explained through a higher local supersaturation of the reaction solution resulting in an exponential increase of the nucleation rate. Further reductions of the stabilizer concentration led to bigger particles with diameter of 8.4±2.3 (20/1) and 10.7±3.0 nm (30/1) showing that the amount of stabilizer was not sufficient enough to prevent the particles fully from aggregation/agglomeration and Ostwald ripening.

The presence of nanoparticles suggested that the stabilizer AOT must have interacted with the zinc peroxide surface resulting in its stabilization. FTIR and pH dependent zeta potential measurements showed that the sulfonate function of the AOT interacted with the nanoparticles most probably via physisorption. Additionally the zeta potential measurements indicated the formation of an AOT double layer around the synthesized nanoparticles. The sulfonate groups of the first layer interacted with the surface while the sulfonate groups of the second layer were

directed toward the dispersion medium inducing a negative surface charge in basic environment.

Furthermore the sample compositions could be controlled trough the initial zinc acetate:AOT ratios. The stabilizer sample amount decreased constantly from 45.5 to 28.2 wt% with decreasing initial stabilizer concentration from $1.9 \cdot 10^{-3}$ (5/1) to $3.2 \cdot 10^{-4}$ mol/L (30/1) while the zinc peroxide sample amount increased proportionally. Contrary the conversion of the precursor zinc acetate showed no clear trend. The conversion varied between 37.3 and 52.5 %.

The temperature induced oxygen release of the AOT stabilized nanoparticles was investigated via TGA measurements. It could be shown that the amount of released oxygen increased from 2.1 (5/1) to 2.7 mmol O_2/g sample (30/1) with increasing zinc peroxide sample amount from 54.5 to 72.0 wt%. Only sample ZnO_2/AOT (20/1) showed a divergent behavior with an oxygen release of 1.8 mmol O_2/g sample. The pH induced oxygen release in aqueous solution was determined via continuous long time measurements under argon atmosphere. The influence of different sample compositions, nanoparticle diameters and pH values on the amount of released oxygen was investigated. The measurements revealed that sample ZnO_2/AOT (10/1) released the highest amount of oxygen (1.69 mg/L) due to the smallest nanoparticles present (2.1±0.6 nm) for this sample. Further a pH dependence of the oxygen release could also be proven. The release decreased constantly from 1.21 to 0.06 mg/L with increasing pH value from 6.5 to 8.5, which was in line with the expectations.

2.4 Synthesis of Biofunctionalized ZnO_2 Nanoparticles*

2.4.1 Introduction

Beside the already discussed functionalized nanoparticles also biofunctionalized zinc peroxide nanoparticles were successfully synthesized. Glucose-1-phosphate (Glc-1P) and uridine 5'-diphosphoglucose (UDP-Glc) were used for the stabilization and functionalization of the nanoparticles (Figure 2.4.1). Both syntheses were carried out in aqueous media with the precursor zinc acetate and the precipitation agent hydrogen peroxide, but the synthesis of the ZnO_2/Glc-1P nanoparticles was done within the high pressure impinging jet-reactor while the synthesis of the ZnO_2/UDP-Glc nanoparticles was performed in a flask. On the one hand these bio molecules took part in the stabilization of the nanoparticles through their phosphate functions and on the other hand they introduced the bioactive glucose function to the nanoparticle surface, which could be used as a bio-recognition linker in biological systems.

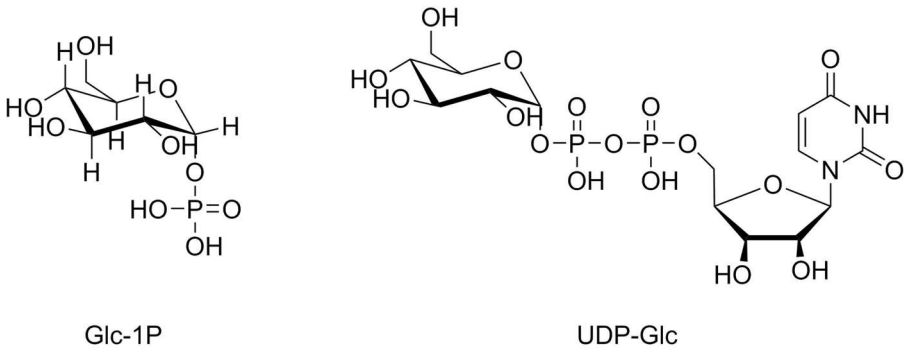

Figure 2.4.1: *Chemical structure of the stabilizer molecules glucose-1-phosphate (Glc-1P) and uridine 5'-diphosphoglucose (UDP-Glc).*

This linking can take place through the interaction between the glucose function and lectins present on the cell surface. Lectins are structurally diverse carbohydrate-binding proteins of nonimmune origin. Most of these lectins possess two or more sugar binding sites and can agglutinate cells and/or precipitate complex carbohydrate conjugates.[103,104] They are normally located in the glycocalyx, a carbohydrate cell coating consisting of membrane, glycoproteins, glycolipids and glycosaminoglycans and are responsible for cell-cell interactions by combining with complementary carbohydrates on opposing cells (Figure 2.4.2).[105–107]

For this study the lectin Concanavalin A (ConA) was used to show that the synthesized nanoparticles indeed interact specifically with biomolecules through the

*Reproduced from Christian Bergs, Lisa Brück, Ruben R. Rosencrantz, Georg Conrads, Lothar Elling, Andrij Pich; *Biofunctionalized ZnO_2 nanoparticles as active oxygen source and antibacterial agents* (submitted).

surface located glucose function. ConA is a lectin, which interacts specifically with the α forms of mannose and glucose and can be found in plants, animals and microorganisms.[104,108,109] The protein consists of four identical subunits with a molecular weight of approximately 27000 Da for each monomeric unit.[110,111] Con A subunit interactions are dependent on pH. At pH values between 2.0 and 5.5 ConA consists of two non covalently bound subunits building a dimer, whereas at pH values above 5.5 a tetramer with a molecular weight of 110000 Da is formed.[112,113] The interactions between the subunits contain mostly of hydrogen and salt bridge bonds explaining the pH dependence.[111] The subunit carbohydrate binding sites of ConA facilitate mostly hydrogen bonds to the oxygen atoms of glucose or mannose through the amino acid residues Arg228, Asn14, Asp208, Tyr100 and Leu99.[114] During this interaction the position of the oxygen atoms of the sugar molecules is crucial for the strength of the resulting bonding. Previous studies showed that ConA establishes in total seven hydrogen bonds to methyl-α-D-mannopyranoside but especially three bonds showed an increased stability due to nearly linear bond angles and short bond lengths caused through the O-atom-positions (Figure 2.4.2). Beside the hydrogen bonds hydrophobic interactions take also part in the specific interaction of ConA and glucose or mannose molecules. It was shown that the aromatic ring of Tyr12 interacts with two C atoms of the pyranose ring resulting in a stabilization of the binding site.[114–116] These specifications made the ConA a suitable choice to investigate the binding properties of the synthesized and functionalized zinc peroxide nanoparticles.

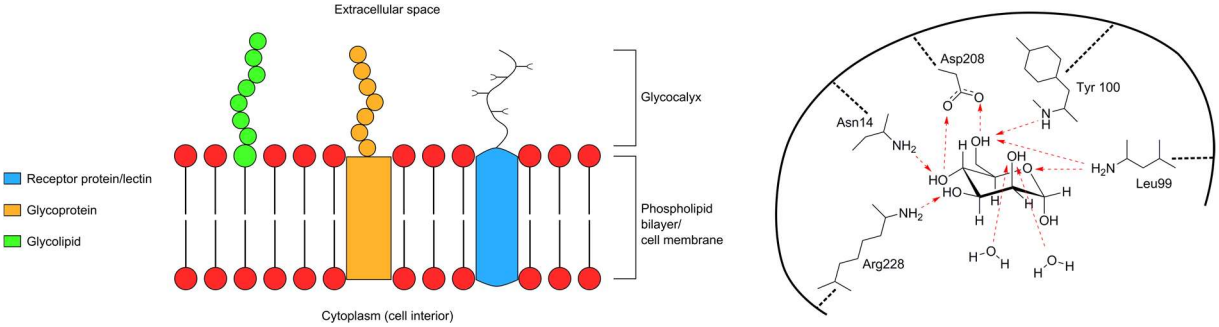

Figure 2.4.2: *Schematic illustration of a cell surface containing the glycocalyx layer (left); schematic illustration of the binding pocket of the lectin Concanavalin A (ConA) including the formation of hydrogen bonds between the functional groups of the lectin (Arg228, Asn14, Asp208, Tyr100 and Leu99) and a α-form mannose molecule (right).*[116]

Furthermore the uridine group of the UDP-Glc was introduced as a model function. Its presence was investigated after the synthesis to prove that the stabilizer molecule remained intact while its sterical influence on the glucose lectin interaction was investigated too. These data were crucial for the application of other, more specific

functionalized uridine phosphates for the synthesis and stabilization of zinc peroxide nanoparticles. For example the integration of sugar functions like N-acetyl-D-lactosamine (LacNac) could lead to specific interactions with galectins present on cancer cell surfaces.[117] This targeting would allow a controlled oxygen release in cancerogenous domains which could lead to new treatment methods.

2.4.2 Chemical Structure of ZnO_2 nanoparticles

The synthesis of the ZnO_2/Glc-1P nanoparticles was carried out in the high pressure impinging jet-reactor and the influence of different reaction times (4min (10 cycles), 8min (20 cycles), 12min (30 cycles) and 16min (40 cycles)) and zinc acetate:Glc-1P ratios (1/1, 2/1, 4/1, 6/1, 8/1 and 10/1) on the crystal structure, the sample compositions, the nanoparticle sizes and morphologies, the oxygen release properties and the protein adsorption properties was investigated analogously to the already discussed nanoparticles. Contrary the synthesis of zinc peroxide nanoparticles stabilized with UDP-Glc was carried out in flask due to the complexation of metal ions through diphosphates.[118] This led to an increased precipitation which influenced the nucleation and growth rate of the nanoparticles and consequently their sizes and morphologies. Therefore sequential additions of UDP-Glc solutions (via syringe pumps) to the reaction solutions were tested to minimize or overcome the complexation of the zinc ions leading to smaller and more uniform nanoparticles. The UDP-Glc injection was started simultaneously with reaction start or with different time delays (3.0, 4.0 or 5.0 minutes) at constant total reaction time of 45 minutes. Furthermore the influence of similar precursor:stabilizer ratios like for the ZnO_2/Glc-1P nanoparticles was investigated. XRD measurements revealed that the typical reflexes for zinc peroxide could be obtained in most cases for both synthesis approaches (Figure 2.4.3). Only the measurement of sample ZnO_2/UDP-Glc (1/1)_4min did not show the typical reflexes which could be assigned to the high UDP-Glc sample content which disturbed the measurement. Therefore only one representative diffractogram is shown for each synthesis approach in comparison to the diffractogram of the zinc peroxide reference (remaining diffractograms see section 7).

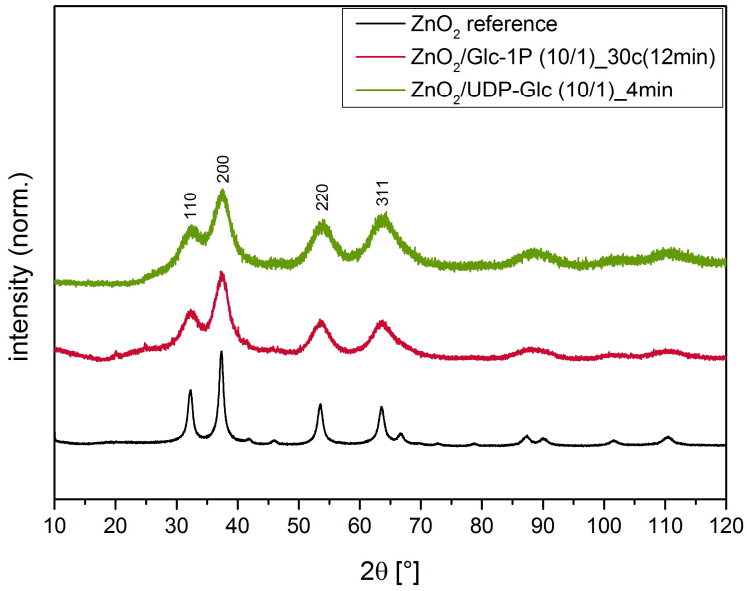

Figure 2.4.3: Representative *XRD measurements of the zinc peroxide nanoparticles stabilized with glucose-1-phospahte (Glc-1P) and uridine 5'-diphosphoglucose (UDP-Glc) in comparison to the zinc peroxide reference.*

The diffractograms showed the typical reflexes for zinc peroxide at 2Θ = 31.0, 36.5, 53.0 and 63.0° which could be allocated to the indexes 111, 200, 220 and 311 which are characteristic for the cubic crystal structure of zinc peroxide. Beside the identification of the typical reflexes it was also possible to detect broadened reflexes indicating the presence of nanoparticles.[78] By measuring the full width at half maximum (FWHM) of the reflexes 220 and 311 it was again possible to calculate the crystallite sizes of the different samples via the Debye Scherrer equation (Equation 5).[79] Crystallite sizes between 1.9±0.3 and 3.3±0.5 nm could be calculated indicating that all samples consisted of small nanoparticles. A more detailed discussion of the nanoparticle sizes can be found in section 2.4.3.

ICP-OES measurements proved that different reaction times (cycle numbers) and zinc acetate:Glc-1P ratios did have an influence on the sample compositions and precursor conversions of the ZnO_2/Glc-1P nanoparticles (Table 2.4.1). The data showed that the sample compositions for the reaction time experiments only slightly changed which was in line with the expectations due to the same synthesis ratios during these experiments. The sample ratios were between 30.35/69.46 and 37.65/62.34 wt% (ZnO_2/Glc-1P) which showed that a relatively high amount of Glc-1P could be immobilized on the nanoparticle surface which could be explained through the high initial amount of stabilizer during the synthesis (precursor:stabilizer ratio 1/1). Additionally, these data indicated that the synthesis was quite reproducible.

Table 2.4.1: *Chemical compositions and precursor conversions of the Glc-1P stabilized zinc peroxide nanoparticles synthesized at different reaction times and $Zn(ac)_2$:Glc-1P ratios determined via ICP-OES.*

Sample	Synthesis ratio $Zn(ac)_2$/Glc-1P	Reaction time [min]	Sample composition [wt%/wt%]	Conversion $Zn(ac)_2$ [%]
ZnO_2/Glc-1P (1/1)_10c(4min)	1/1	4	33.82/66.17	34.3
ZnO_2/Glc-1P (1/1)_20c(8min)	1/1	8	37.65/62.34	38.1
ZnO_2/Glc-1P (1/1)_30c(12min)	1/1	12	30.53/69.46	31.7
ZnO_2/Glc-1P (1/1)_40c(16min)	1/1	16	35.60/64.39	38.3
ZnO_2/Glc-1P (2/1)_30c(12min)	2/1	12	50.89/49.10	20.6
ZnO_2/Glc-1P (4/1)_30c(12min)	4/1	12	73.61/26.38	33.8
ZnO_2/Glc-1P (6/1)_30c(12min)	6/1	12	71.49/28.50	55.9
ZnO_2/Glc-1P (8/1)_30c(12min)	8/1	12	83.47/16.52	47.1
ZnO_2/Glc-1P (10/1)_30c(12min)	10/1	12	93.91/6.08	77.2

It was also possible to observe a correlation between the zinc acetate:Glc-1P ratios and the resulting sample compositions. The sample content of Glc-1P decreased from 69.46 wt% (synthesis ratio 1/1) to 6.08 wt% (synthesis ratio 10/1) while the zinc peroxide sample amount increased from 30.53 wt% to 93.91 wt%. This behavior was in line with the expectations due to the fact that a higher initial synthesis concentration of glucose-1-phosphate should result in more immobilized stabilizer molecules on the nanoparticle surface. Further the precursor conversion increased relative constantly from 31.7 to 77.2 % with decreasing stabilizer concentration at constant reaction time. The experimental XRD and ICP-OES data indicate that the structure, size and chemical composition of Glc-1P stabilized nanoparticles can be tuned by the synthesis parameters. In addition, ICP-OES proved that the amount of glucose-1-phosphate on the nanoparticle surface could be flexibly adjusted by the initial stabilizer concentrations of the reaction mixture.

Additionally ICP-OES measurements proved the influence of different UDP-Glc addition sequences and zinc acetate:UDP-Glc ratios on the sample compositions and precursor conversions of the ZnO_2/UDP-Glc nanoparticles. Preliminary electrophoresis reference measurements (see section 7) of pure UDP-Glc proved that 98.4 % of the stabilizer molecules were intact after treatment at the nanoparticle

synthesis reaction conditions (t = 45 minutes, T = 80.0 °C) which was crucial for the following analyses.

Table 2.4.2: *Synthesis ratios, UDP-Glc addition delays, sample compositions and precursor conversions for the different zinc peroxide nanoparticle samples stabilized with UDP-Glc.*

Sample	Synthesis ratio $Zn(ac)_2$/UDP-Glc	UDP-Glc addition delay [min]	Sample composition [wt%/wt%]	Conversion $Zn(ac)_2$ [%]
ZnO_2/UDP-Glc (8/1)_direct	8/1	direct	58.6/41.4	22.2
ZnO_2/UDP-Glc (8/1)_3min	8/1	3.0	75.1/24.9	41.3
ZnO_2/UDP-Glc (8/1)_4min	8/1	4.0	67.4/32.6	48.6
ZnO_2/UDP-Glc (8/1)_5min	8/1	5.0	70.1/29.9	46.7
ZnO_2/UDP-Glc (1/1)_4min	1/1	4.0	49.6/50.4	46.7
ZnO_2/UDP-Glc (2/1)_4min	2/1	4.0	54.5/45.5	34.5
ZnO_2/UDP-Glc (4/1)_4min	4/1	4.0	60.2/39.8	37.9
ZnO_2/UDP-Glc (6/1)_4min	6/1	4.0	65.6/34.4	35.8
ZnO_2/UDP-Glc (10/1)_4min	10/1	4.0	78.0/22.0	45.4

The measurements showed no clear trend for the sample compositions of the different sequence variation samples (Table 2.4.2). For example increased the zinc peroxide sample content from 58.6 to 75.1 wt% with increasing delayed addition of UDP-Glc from directly to 3.0 minutes while further delayed additions of 4.0 or 5.0 minutes resulted in zinc peroxide sample contents of 67.4 respectively 70.1 wt%. The increase could be explained through a longer unopposed zinc peroxide seed formation for sample ZnO_2/UDP-Glc (8/1)_3min compared to sample ZnO_2/UDP-Glc (8/1)_direct. The seeds could be formed freely during the first 3.0 minutes without any possible zinc ion complexation through UDP-Glc which results in more controlled growth processes. Contrary the zinc peroxide sample content decrease for sample ZnO_2/UDP-Glc (8/1)_4min and ZnO_2/UDP-Glc (8/1)_5min did not fit to this explanation. Furthermore different delayed additions of UDP-Glc did also have an influence on the conversion of the precursor zinc acetate. The conversion increased from 22.2 to 48.6 % with increasing delays from directly to 4.0 minutes. This increase was in line with the expectations due to the zinc ion complexation properties of the UDP-Glc.[118] Like already mentioned should a more delayed addition of UDP-Glc lead to a more controlled seed formation and growth resulting in higher precursor conversions.

Also different precursor:stabilizer ratios ratios influenced the sample compositions and precursor conversions. A continous zinc peroxide sample content increase from 49.6 to 78.0 wt% could be observed with decreasing initial stabilizer concentration from 0.018 to 0.0018 mol/L. This showed that the final sample composition could be simply adjusted by varying the initial educt amounts. In contrast the precursor conversions showed no clear trend. Values between 48.6 (ZnO_2/UDP-Glc (8/1)_4min) and 34.5 % (ZnO_2/UDP-Glc (2/1)_4min) could be determined. These data could indicate problems during the purification process which could influence the conversion calculations.

2.4.3 Size and Morphology of ZnO_2 nanoparticles

The crystallite size calculations from XRD data done via the Debye Scherrer equation revealed that small and uniform crystallites could be obtained for all synthesized samples. This was a first evidence for the presence of small and uniform nanoparticles. Transmission electron microscopy measurements (TEM) were done to proof this assumption (Figure 2.4.4, representative examples (all other images are shown in section 7)). The measurements showed that indeed small and uniform nanoparticles could be obtained for the ZnO_2/Glc-1P samples, which could be assigned to the used impinging jet reactor and the efficient stabilization through the stabilizer molecule glucose-1-phosphate. Contrary TEM measurements showed that mostly all ZnO_2/UDP-Glc samples exhibited a bimodal size distribution. Small (<10.0 nm) and bigger nanoparticles (between 17.5±8.7 and 32.6±13.0 nm) could be detected in all cases. The average particle sizes and standard deviations of the different samples were determined by measuring over 100 separate nanoparticles for every sample followed by standard deviation calculation (Figure 2.4.4, Table 2.4.3).

It could be observed that the ZnO_2/Glc-1P nanoparticle sizes were dependent on the reaction times (cycle numbers). The nanoparticle diameter decreased from 9.4±5.2 to 5.0±1.5 nm by increasing the reaction time from 4 to 12min. An additional increase to 16min resulted contrary in an increase of the particle diameter to 6.3±1.8 nm.

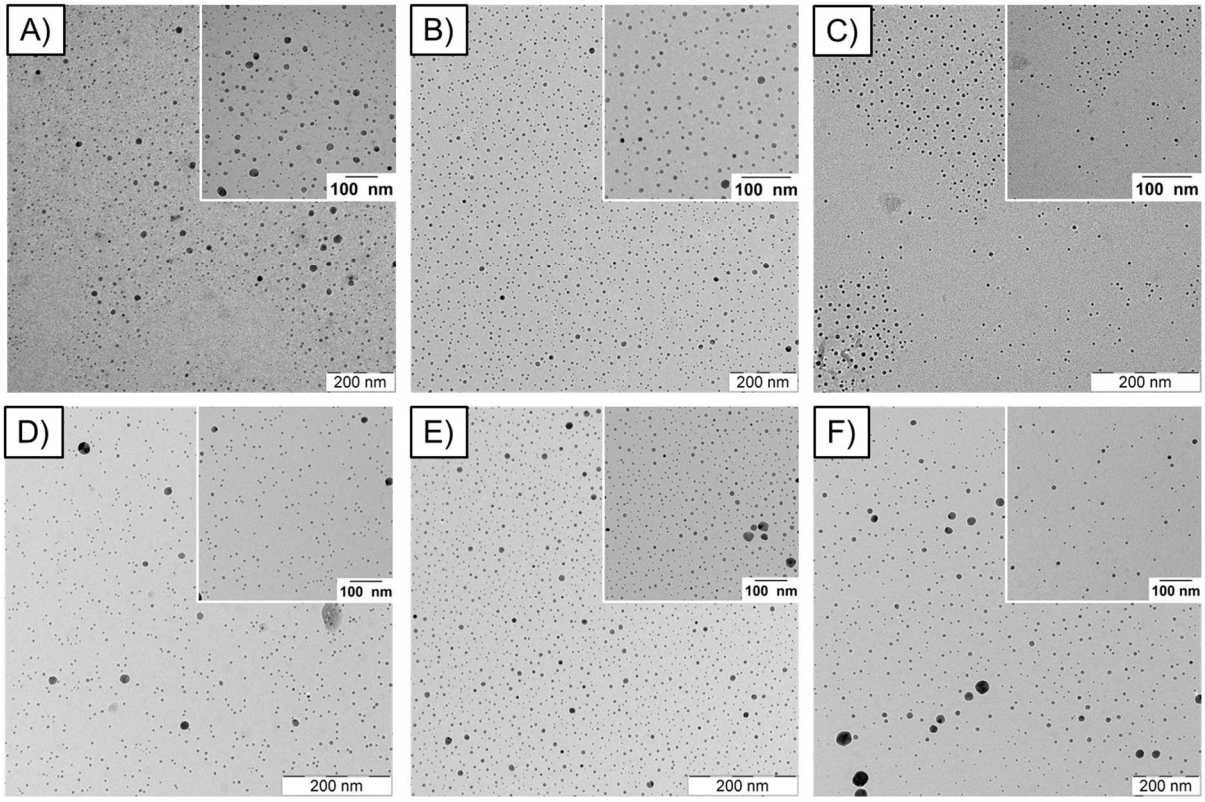

Figure 2.4.4: *TEM images of the different ZnO_2/Glc-1P and ZnO_2/UDP-Glc samples: A) ZnO_2/Glc-1P (1/1)_10c(4min), B) ZnO_2/Glc-1P (1/1)_20c(8min), C) ZnO_2/Glc-1P (1/1)_30c(12min), D) ZnO_2/UDP-Glc (1/1)_4min, E) ZnO_2/UDP-Glc (4/1)_4min, F) ZnO_2/UDP-Glc (10/1)_4min.*

The decrease of the nanoparticle sizes can be explained through the longer exposition of the particles to the shear and impact forces inside the reaction chamber which is supported by the standard deviation decrease from ±5.2 to ±1.5 nm showing that more uniform particles were formed during longer reaction times. The following increase at 16min reaction time did not correspond to the expectations. This behavior can maybe be explained through Ostwald ripening taking place at the highest reaction time which was already observed for other nanoparticle systems.

Different synthesis ratios between 1/1 and 10/1 ($Zn(ac)_2$/Glc-1P) were tested with aspect on the decrease of the Glc-1P amount. ICP-OES measurements showed (section 2.4.2) that these experiments led to a continuous decrease of the stabilizer amount in the resulting samples. A decrease of the stabilizer amount should result in larger or more polydisperse nanoparticles due to a lack of stabilization. But in case of the ZnO_2/Glc-1P nanoparticles nearly no dependence of the sizes to the amount of stabilizer could be found based on TEM investigations.

Table 2.4.3: *Nanoparticle diameters and crystallite sizes with corresponding standard deviations for the different Glc-1P and UDP-Glc stabilized ZnO_2 samples.*

Sample	Particle diameter small size fraction [nm] (TEM)	Particle diameter big size fraction [nm] (TEM)	Crystallite sizes [nm] (XRD)
ZnO_2/Glc-1P (1/1)_10c(4min)	9.4±5.2	---	3.3±0.5
ZnO_2/Glc-1P (1/1)_20c(8min)	6.3±2.2	---	3.1±0.4
ZnO_2/Glc-1P (1/1)_30c(12min)	5.0±1.5	---	3.3±0.4
ZnO_2/Glc-1P (1/1)_40c(16min)	6.3±1.8	---	3.1±0.3
ZnO_2/Glc-1P (2/1)_30c(12min)	4.5±1.2	---	2.3±0.2
ZnO_2/Glc-1P (4/1)_30c(12min)	4.2±1.3	---	2.8±0.1
ZnO_2/Glc-1P (6/1)_30c(12min)	4.1±1.4	---	2.8±0.2
ZnO_2/Glc-1P (8/1)_30c(12min)	4.8±1.7	---	2.8±0.1
ZnO_2/Glc-1P (10/1)_30c(12min)	4.0±1.2 + aggregates	---	2.7±0.2
ZnO_2/UDP-Glc (8/1)_direct	Aggregates	Aggregates	2.3±0.3
ZnO_2/UDP-Glc (8/1)_3min	4.6±1.4	24.3±6.4	2.6±0.5
ZnO_2/UDP-Glc (8/1)_4min	5.1±1.3	32.6±13.0	2.5±0.6
ZnO_2/UDP-Glc (8/1)_5min	Aggregates	Aggregates	2.4±0.2
ZnO_2/UDP-Glc (1/1)_4min	7.0±1.7	18.4±6.3	---
ZnO_2/UDP-Glc (2/1)_4min	4.8±1.2	17.5±8.7	1.9±0.3
ZnO_2/UDP-Glc (4/1)_4min	3.4±1.1	32.0±15.1	2.0±0.3
ZnO_2/UDP-Glc (6/1)_4min	5.2±1.5	25.5±9.7	2.7±0.3
ZnO_2/UDP-Glc (10/1)_4min	6.8±2.0	24.4±9.3	2.4±0.1

Nanoparticle diameter between 4.1±1.4 and 4.8±1.7 nm could be detected for the different educt ratio experiments 2/1, 4/1, 6/1 and 8/1 (Table 2.4.3) showing no difference in nanoparticle sizes with aspect on the nearly similar standard deviations. Only the samples 1/1 and 10/1 showed a divergent behavior. Especially the 10/1 sample showed beside small nanoparticles also aggregates/agglomerates indicating that a stabilizer sample amount of 6.08 wt% was not high enough to prevent the nanoparticles fully from aggregation/agglomeration. These data showed that glucose-1-phosphate seemed to be a very effective stabilizer in combination with the impinging jet reactor due to the fact that even a stabilizer sample amount of 16.52 wt% led to uniform and small nanoparticles with a diameter of 4.8±1.7nm. This good stabilizer property could be assigned to the glucose ring of the molecule, which could introduce a quiet steric function to the nanoparticle surface.

Furthermore the measurements showed for the ZnO_2/UDP-Glc nanoparticles that the sequential addition of the stabilizer UDP-Glc had a significant influence on the sizes and morphologies of the formed zinc peroxide particles. For example only big and undefined aggregates/agglomerates could be detected for the samples ZnO_2/UDP-Glc (8/1)_direct and ZnO_2/UDP-Glc (8/1)_5min while small and uniform respectively bigger nanoparticles could be found for the samples ZnO_2/UDP-Glc (8/1)_3min (4.6±1.4 nm/24.3±6.4 nm) and ZnO_2/UDP-Glc (8/1)_4min (5.1±1.3 nm /32.6±13.0 nm). The formation of aggregates and agglomerates for sample ZnO_2/UDP-Glc (8/1)_direct could be caused through the uncontrolled complexation of the zinc ions through the immediate addition of the stabilizer. Contrary the occurrence of bigger clusters for sample ZnO_2/UDP-Glc (8/1)_5min could indicate that the addition of the stabilizer after 5.0 minutes reaction time did not lead to a sufficient stabilization of the already formed nanoparticle seeds anymore. The increase of the average sizes/standard deviations of the bigger nanoparticles from sample ZnO_2/UDP-Glc (8/1)_3min to sample ZnO_2/UDP-Glc (8/1)_4min would support this assumption indicating a more uncontrolled particle growth.

It could also be proven that different precursor:stabilizer ratios did influence the sizes of the ZnO_2/UDP-Glc nanoparticles similar to the BMEP, citrate and AOT stabilized nanoparticles. The average diameter of the small nanoparticles decreased from 7.0±1.7 to 3.4±1.1 nm with decreasing initial UDP-Glc concentration from 0.018 (ZnO_2/UDP-Glc (1/1)_4min) to 0.0045 mol/L (ZnO_2/UDP-Glc (4/1)_4min). A further stabilizer concentration decrease down to a value of 0.0018 mol/L (ZnO_2/UDP-Glc (10/1)_4min) contrary caused again bigger nanoparticles with diameters up to 6.8±2.0 nm. The decrease could again be allocated to higher local precursor supersaturations at lower stabilizer concentrations, while the increase was caused through a lack of stabilization or Ostwald ripening. In contrast the bigger nanoparticles formed during the different syntheses did not show a similar clear trend. Average nanoparticle diameter between 18.4±6.3 (ZnO_2/UDP-Glc (1/1)_4min) and 32.6±13.0 nm (ZnO_2/UDP-Glc (8/1)_4min) could be detected but no significant dependence on the initial zinc acetate:UDP-Glc ratio could be observed. This indicated more uncontrolled particle growth processes maybe caused through Ostwald ripening.[23] However the TEM investigations led to the qualitative assumption that the fraction of smaller nanoparticles was way larger than the fraction of the

bigger particles, but the share of the bigger particle fraction increased with decreasing stabilizer concentration.

The crystallite size calculations via Debye Scherrer equation supported the assumptions made based on the TEM images. Crystallite sizes between 1.9±0.3 and 3.3±0.5 nm could be calculated which indicated that the ZnO_2/Glc-1P nanoparticles consisted mostly of two or three crystallites each while the small respectively big ZnO_2/UDP-Glc nanoparticles consisted of two or three respectively nine to sixteen crystallites (Table 2.4.3).

2.4.4 Chemical Composition of ZnO_2 Nanoparticles Surface

TEM images and crystallite size calculations proved that nanoparticles could be obtained for both synthesis approaches. This indicated that both stabilizing molecules must have interacted with the nanoparticle surface, especially in case of the ZnO_2/UDP-Glc nanoparticles. A synthesis carried out in flask can only lead to a nanoparticulate product with stabilizing agents interacting with the product surface. Solid state 31-phosporous nuclear magnetic resonance measurements (^{31}P-NMR) were performed to investigate changes of the surrounding of the phosphorous atom of the Glc-1P in dependence of the presence of zinc peroxide. One representative synthesized sample (ZnO_2/Glc-1P (1/1)_30c(12min)) and the reference substance Glc-1P were measured and the comparison of the different ^{31}P-NMR signals enabled the enlightenment of the type of interaction between the Glc-1P and the nanoparticle surface (Figure 2.4.5). Further FTIR measurements of one representative sample (ZnO_2/UDP-Glc (2/1)_4min) proved the interaction between the diphosphate function of the UDP-Glc with the zinc peroxide nanoparticle surface (Figure 2.4.6), while pH dependent zeta potential measurements supported for both nanoparticle systems the interaction investigations (Figure 2.4.7).

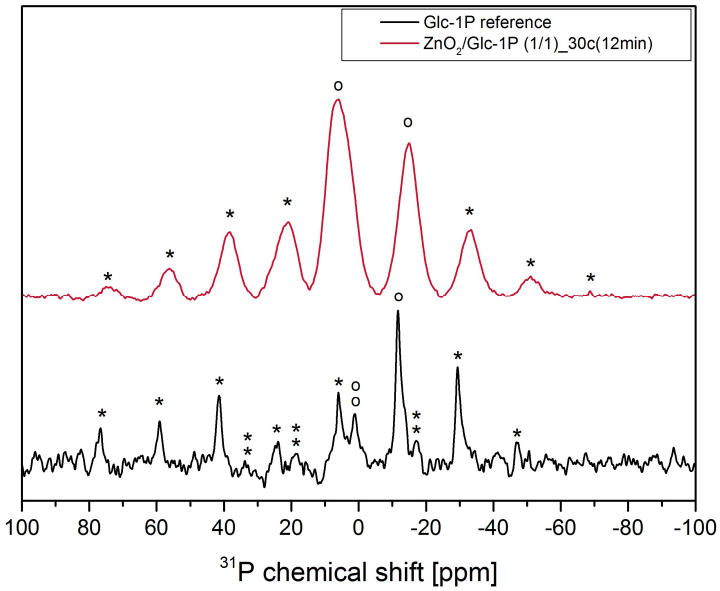

Figure 2.4.5: *^{31}P solid state NMR measurements of ZnO_2/Glc-1P (1/1)_30c(12min) and the reference substance Glc-1P with the phosphate signal (o), internal standard signal (oo) and their corresponding side bands (* and **).*

The reference substance measurement showed one signal at -11.59 ppm which could be assigned to the phosphor atom and several signals at -47.24, -29.52, 5.90, 24.49, 41.33, 59.27 and 76.33 ppm which were the corresponding side bands of the phosphor signal caused through the magic angle spinning (MAS) at 5 kHz. Additionally the signal at 0.87 ppm could be assigned to residues of the internal standard compound (ammonium phosphate) with its spinning side bands at -16.84, 18.38 and 33.66 ppm. It can be seen that the phosphate signal at -11.59 ppm was quiet discrete (signal width 5.43 ppm) indicating that only one confirmation of the O-P-O bond angle of the phosphate function was present.[119] Contrary to this the ^{31}P-NMR spectra of the synthesized sample showed many differences. For example showed the sample spectra not only one but two signals for the phosphor atom at -14.59 and 6.08 ppm with the corresponding side bands at -69.01, 51.07, 32.52, 21.28, 38.60, 56.24 and 74.48 ppm. These two signals were broadened (signal widths: 17.63 and 18.02 ppm) compared to the reference signal indicating a change of the O-P-O bond angle and the presence of different binding sites and modes of the phosphate function which was caused through the interaction of the Glc-1P with the zinc peroxide surface.[119,120] Additionally an upfield shift (lower ppm) of -3.0 ppm and a downfield shift (higher ppm) of +17.6 ppm was observed for the two different phosphor signals compared to the one reference signal. Previous studies showed that an upfield shift is mostly caused through the chemisorption of phosphate ligands

via the P-OH function on metal oxide surfaces resulting in mono-, bi- or trident bondings.[121] Considering the relatively low upfield shift of -3.0 ppm a mono dentate bonding of the Glc-1P on the nanoparticle surface is most likely. The strong downfield shift of +17.6 ppm can be explained through the interaction between the P=O function and hydroxyl functions present on the nanoparticle surface (physisorption).[121] This two different types of interaction are in good correlation to the broadening of the NMR signals mentioned above and proved clearly the binding of Glc-1P on the nanoparticle surface.

Furthermore figure 2.4.6 shows the FTIR spectra of the analyzed sample ZnO_2/UDP-Glc (2/1)_4min and the reference substance UDP-Glc. The comparison of these two spectra allowed the interpretation of the interaction between the particles and the stabilizer molecules. The detected signals could all be assigned to the functional groups of UDP-Glc.

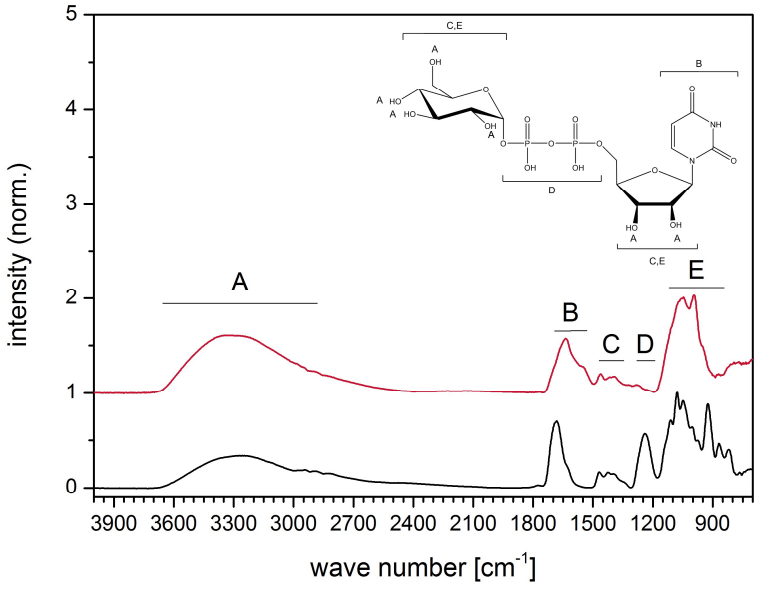

Figure 2.4.6: *FTIR measurements for the synthesized sample ZnO_2/UDP-Glc (2/1)_4min (red) and the UDP-Glc reference substance (black).*

For example was the broad peak between 3715 and 2632 cm^{-1} (A) caused through the hydroxyl functions (-OH) of the glucose ring and the uridine function while the relatively discrete signal at 1684 cm^{-1} (B) could be assigned to the tertiary amine of the uracil ring. Further a small shoulder at 1626 cm^{-1} could be observed which was allocated to the deformation vibration of the secondary amine of the uracil ring. Additionally the signals between 1500 and 1306 (C) and 1172 and 767 cm^{-1} (E) were allocated to the C-O and C-O-C vibrations of the glucose and ribofuranose rings

while the signal at 1243 cm^{-1} (D) was characteristic for the P=O stretching vibration of the diphosphate function of the UDP-Glc. The sample spectrum showed overall the same signals with exception of the diphosphate signal (D) which could not be detected for the sample spectrum. This showed that the chemical environment of this function changed which could indicate the interaction of the diphosphate function with the nanoparticle surface resulting in its stabilization. Furthermore a broadening and shift (50 cm^{-1}) of signal B could be detected for the sample spectrum which could have been caused through different packing densities of the UDP-Glc for the synthesized sample compared to the reference substance.[82]

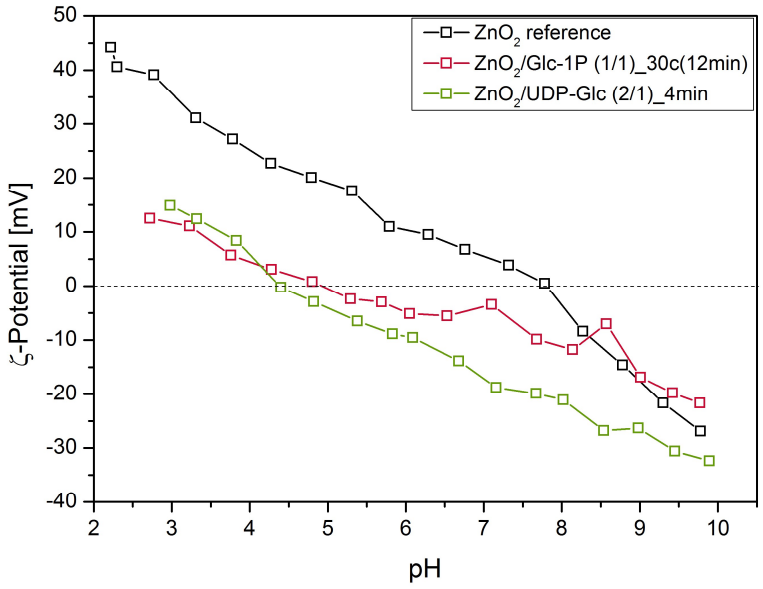

Figure 2.4.7: *pH dependent zeta potential measurements of ZnO_2/Glc-1P (1/1)_30c(12min), ZnO_2/UDP-Glc (2/1)_4min and the reference substance zinc peroxide.*

Additionally pH dependent zetapotential measurements were performed to validate and support the assumptions made based on the ^{31}P solid-state NMR and FTIR measurements (Figure 2.4.7). A modification of the zinc peroxide surface by the bio molecules Glc-1P and UDP-Glc should result in a variation of the surface charge of the synthesized nanoparticles. The comparison with a reference measurement of unmodified zinc peroxide revealed that indeed differences occurred. An ampholyte behavior could be observed for both functionalized nanoparticles and the reference substance but the isoelectric points were shifted from 8.00 to 4.88 (ZnO_2/Glc-1P) and 4.43 (ZnO_2/UDP-Glc) in comparison with the zinc peroxide reference. Additionally a decrease of the surface charge could be observed. For example showed the measurements for the Glc-1P stabilized nanoparticles a difference in surface charge of approximately 30.00 mV at pH = 2.50 while at a pH value of 8.20 the difference

between the modified nanoparticles and the reference zinc peroxide was nearly not existing. Similar to this was the surface charge of the UDP-Glc functionalized nanoparticles shifted to maximum values of 14.9 and -32.4 mV. This divergent and approaching behavior can be explained through the glucose ring of the two different stabilizers. This contains four hydroxide functions which can be protonated and deprotonated similar to the hydroxide functions of the unmodified zinc peroxide. But due to the modification of the nanoparticle surface and the steric demanding of the glucose ring a significant decrease of the accessible surface hydroxide functions was achieved in comparison to unmodified zinc peroxide. This decrease caused the lower surface charge in acidic and lightly basic media and explained the approaching of the measured curves in stronger basic media.

2.4.5 Oxygen Release Properties of ZnO_2 Nanoparticles

The pH induced oxygen release of the Glc-1P and UDP-Glc functionalized zinc peroxide nanoparticles was investigated by long time measurements in aqueous media comparable to the already discussed nanoparticle samples. Different nanoparticle samples (ZnO_2/Glc-1P (1/1)_30c(12min), ZnO_2/Glc-1P (4/1)_30c(12min), ZnO_2/Glc-1P (8/1)_30c(12min), ZnO_2/Glc-1P (10/1)_30c(12min), ZnO_2/UDP-Glc (1/1)_4min, ZnO_2/UDP-Glc (4/1)_4min and ZnO_2/UDP-Glc (10/1)_4min) and unmodified zinc peroxide were measured and compared at constant pH value (pH = 6.5) while further the influence of different pH values (pH = 6.5, 7.5 and 8.5) on the oxygen release properties of two representative samples (ZnO_2/Glc-1P (8/1)_30c(12min) and ZnO_2/UDP-Glc (10/1)_4min) was investigated too (Figure 2.4.8 and Table 2.4.4).

The data showed for all samples a constant oxygen release for at least four days resulting in a saturation curve which can be explained through the measurement setup (see section 2.2.5). Further the investigations of the different ZnO_2/Glc-1P and ZnO_2/UDP-Glc samples at a constant pH value of 6.5 revealed that the amount of released oxygen was dependent on the sample compositions and the nanoparticle sizes (Figure 2.4.8a and c).

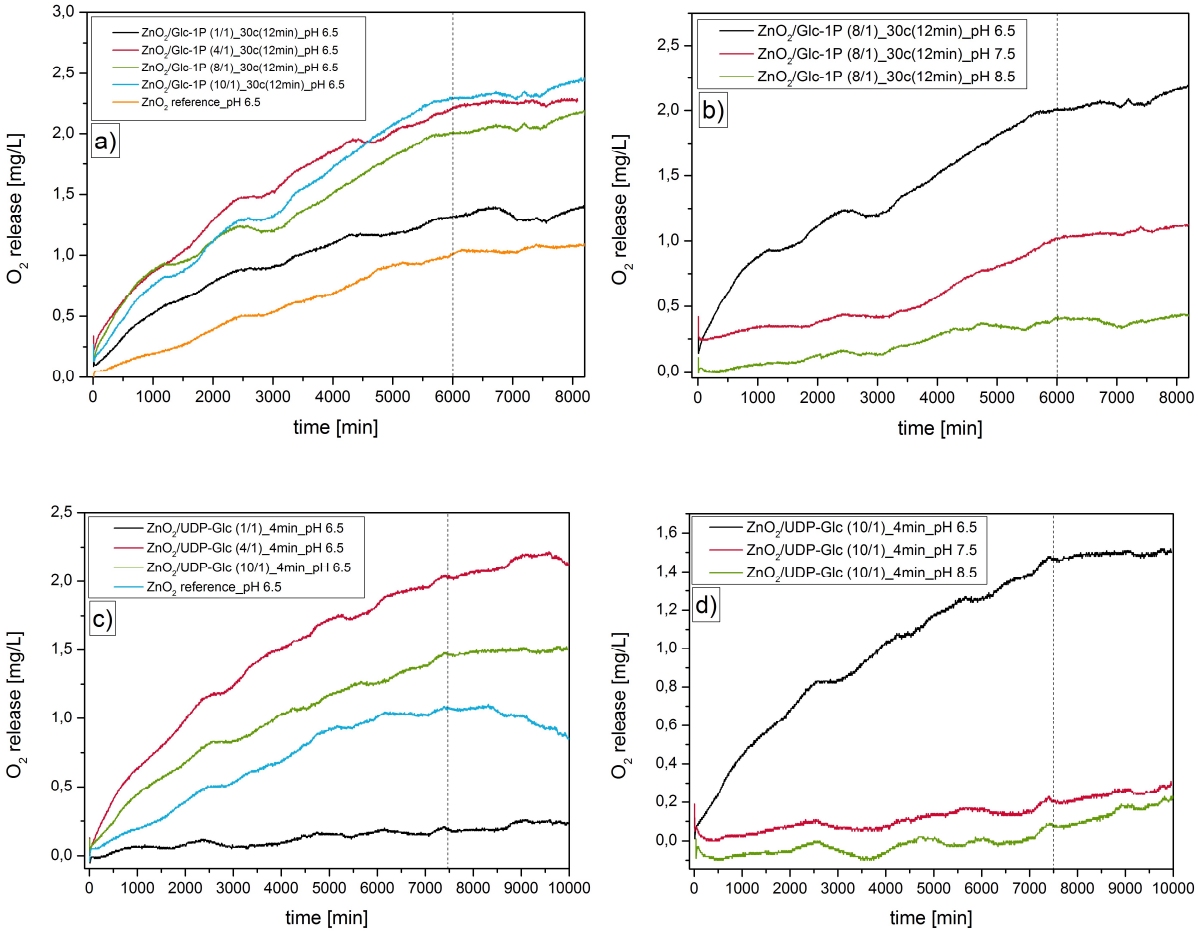

Figure 2.4.8: *Time dependent oxygen release measurements in aqueous media for different ZnO_2/Glc-1P and ZnO_2/UDP-Glc samples at constant pH value (a and c) and for two representative samples at different pH values (b and d); (T=23-24 °C).*

The amount of released oxygen increased with increasing zinc peroxide sample content and/or with decreasing nanoparticle diameter. For example released the sample ZnO_2/Glc-1P (1/1)_30c(12min)_pH 6.5 1.38 mg/L oxygen while the sample ZnO_2/Glc-1P (10/1)_30c(12min)_pH 6.5 already released 2.33 mg/L. This increase correlated with the corresponding zinc peroxide contents of 30.53 and 93.91 wt% as well with the nanoparticle diameter of 5.0±1.5 and 4.0±1.2 nm. A significant higher sample amount of zinc peroxide logically must lead to a higher oxygen release while slightly smaller nanoparticles improve the surface reactivity which additionally should increase the release properties. A size dependent activity trend could also be found for the UDP-Glc samples ZnO_2/UDP-Glc (4/1)_4min_pH 6.5 and ZnO_2/UDP-Glc (10/1)_4min_pH 6.5. Smaller nanoparticles were obtained for the (4/1) sample (3.4±1.1 nm) than for the (10/1) sample (6.8±2.0 nm) leading to higher surface activities which caused higher oxygen release amounts (2.04 and 1.47 mg/L) despite the lower zinc peroxide content for the (4/1) sample (60.2 wt%) compared to the

(10/1) sample (78.0 wt%). The sample ZnO_2/Glc-1P (4/1)_30c(12min)_pH 6.5 did not fit to this expectations. This sample showed a higher oxygen release of 2.26 mg/L compared to the sample ZnO_2/Glc-1P (8/1)_30c(12min)_pH 6.5 (2.06 mg/L) despite its lower zinc peroxide content (73.61 wt%) compared to the 8/1 sample (83.47 wt%) and comparable nanoparticle diameter (4.2±1.3 and 4.8±1.7 nm). The measurements showed also that all synthesized samples released more oxygen than the measured bulk reference substance (0.93 mg/L) with exception of sample ZnO_2/UDP-Glc (1/1)_4min_pH 6.5 which released only 0.21 mg/L oxygen. No significant zinc peroxide reflexes could be detected for the (1/1) sample during the crystal structure investigations (see section 2.4.2) which could explain the inferior release. Nevertheless these observations supported the assumption that smaller particles were capable of releasing more oxygen because of their increased surface activity.

Table 2.4.4: *pH induced oxygen release amounts of the ZnO_2/Glc-1P and ZnO_2/UDP-Glc nanoparticles at different sample compositions and pH values.*

Sample	Oxygen release [mg/L]
ZnO_2/Glc-1P (1/1)_30c(12min)_pH 6.5	1.38
ZnO_2/Glc-1P (4/1)_30c(12min)_pH 6.5	2.26
ZnO_2/Glc-1P (8/1)_30c(12min)_pH 6.5	2.06
ZnO_2/Glc-1P (10/1)_30c(12min)_pH 6.5	2.33
ZnO_2/Glc-1P (8/1)_30c(12min)_pH 7.5	1.05
ZnO_2/Glc-1P (8/1)_30c(12min)_pH 8.5	0.39
ZnO_2/UDP-Glc (1/1)_4min_pH 6.5	0.21
ZnO_2/UDP-Glc (4/1)_4min_pH 6.5	2.04
ZnO_2/UDP-Glc (10/1)_4min_pH 6.5	1.47
ZnO_2/UDP-Glc (10/1)_4min_pH 7.5	0.21
ZnO_2/UDP-Glc (10/1)_4min_pH 8.5	0.08
ZnO_2 reference_pH 6.5	0.93

In addition to the influence of the sample composition and the particle size of ZnO_2 nanoparticles on the amount of released oxygen, the influence of different pH values was investigated. Different pH dependent measurements (pH = 8.5, 7.5, 6.5) of the samples ZnO_2/Glc-1P (8/1)_30c(12min) and ZnO_2/UDP-Glc (10/1)_4min showed that with decreasing pH value the oxygen release increased (Figure 2.4.8b and d). The amount of released oxygen increased constantly from 0.39 to 1.05 and 2.06 mg/L for the Glc-1P stabilized particles and from 0.08 to 0.21 and 1.47 mg/L for the UDP-Glc

stabilized nanoparticles with changing pH value from 8.5 to 7.5 and 6.5. These observations were in line with the already observed behavior of other zinc peroxide nanoparticles which was caused through the nature of the pH induced oxygen release.

2.4.6 Protein/Biofunctionalized Nanoparticle Interaction

After demonstration that the glucose-1-phosphate and the uridine 5'-diphosphoglucose could be immobilized on the nanoparticle surface the recognition of the glucose functions by the lectin Concanavalin A (ConA) was investigated via fluorescence measurements. Lectins are present on every cell surface and are mostly responsible for cell-cell interactions by combining with complementary carbohydrates like glycoproteins, glycolipids and polysaccharides on apposing cells.[122,123] ConA is specific for the α configured gluco- and mannopyranosides. This interaction is mostly based on the formation of hydrogen bonds and hydrophobic interactions while the strength of the interaction is mostly dependent on the position of the oxygen and carbon atoms of the pyranose ring.[114]

Two different types of fluorescent measurements were performed to investigate the interaction specificity between the ConA and the functionalized nanoparticles (Figure 2.4.9). First, the quantification of the interaction between the ConA and the different synthesized samples was investigated followed by an inhibition measurement of one representative sample. The quantification of the immobilized ConA on the nanoparticle surface was achieved through it's labeling with the fluorescent dye Oregon Green. Additionally to these measurements a reference measurement (ZnO_2-Ref) of comparable zinc peroxide nanoparticles (d = 6.1±2.9 nm) stabilized with the organic molecule dioctyl sulfosuccinate (AOT) was performed too (characterization see section 2.3). The surface charge of these particles was nearly neutral (-2.0 mV) at the used measurement conditions like for the Glc-1P and UDP-Glc stabilized particles, but contrary these particles should not show any binding of ConA due to absence of glucose or mannose molecules on the nanoparticle surface.

The fluorescence measurements for the different synthesized samples (Figure 2.4.9a and b) showed clearly a dependence of the ConA binding properties of the nanoparticles to the sample composition and the presence of the stabilizers glucose-

1-phosphate and .uridine 5'-diphosphoglucose. All biofunctionalized nanoparticles showed a significant higher fluorescence compared to the reference nanoparticles stabilized with the surfactant AOT. The reference measurement showed only a minor fluorescence caused through unspecific adhered ConA on the nanoparticles surface like already observed for similar systems in which nanoparticles stuck to cells or proteins.[124]

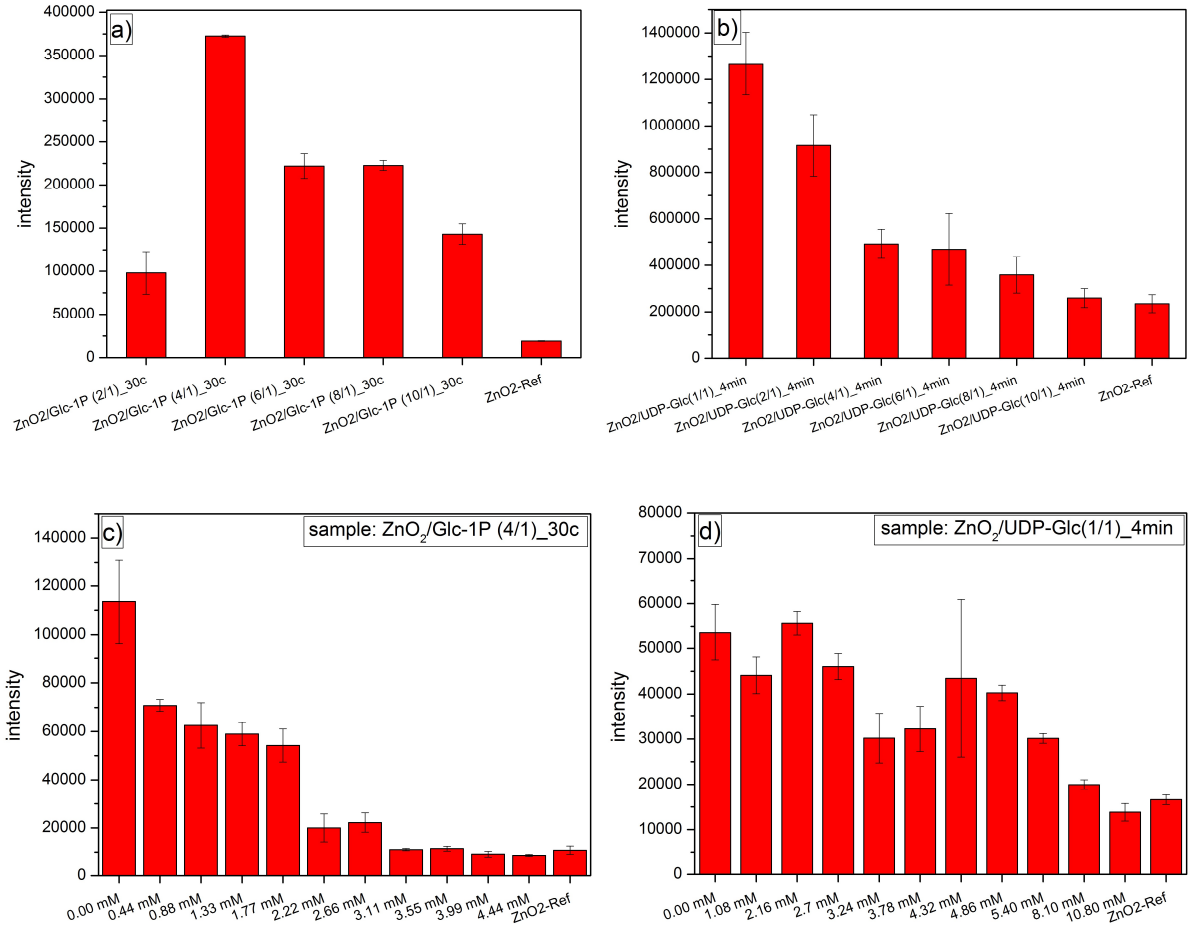

Figure 2.4.9: *Fluorescence measurements for the investigation of the ConA binding to ZnO_2 surface: for the different synthesized samples stabilized with Glc-1P (a) and UDP-Glc (b); inhibition measurements for two representative samples at different mannose concentrations (ZnO_2/Glc-1P: c) and ZnO_2/UDP-Glc (d)).*

The significant higher fluorescence of the other samples can only be explained through a higher amount of immobilized ConA indicating the specific interaction of the ConA with the accessible glucose rings on the biofunctionalized nanoparticles surface.[114] Additionally the interaction between the nanoparticles and the ConA was dependent on the sample compositions but did not show fully the expected trend for the Glc-1P functionalized nanoparticles (Figure 2.4.9a). A higher sample content of Glc-1P should result in a better immobilization of the ConA and subsequently in a

higher fluorescence but the sample ZnO_2/Glc-1P (2/1)_30c(12min) with the highest Glc-1P amount of 49.10 wt% showed the lowest fluorescence of the Glc-1P functionalized nanoparticles. In contrast to that the sample ZnO_2/Glc-1P (4/1)_30c(12min) (Glc-1P amount = 26.38 wt%) showed the highest fluorescence followed by a continuously decrease in fluorescence (fewer immobilization of ConA) with decreasing Glc-1P content for the other samples. An explanation for lower binding of ConA to the ZnO_2/Glc-1P (2/1)_30c(12min) sample could be that the accessibility of the glucose rings was inhibited due to the high amount of stabilizer (higher packing density) which could cause a different orientation of the Glc-1P molecules on the nanoparticle surface compared to the other samples. Similar results were achieved for the stabilization of gold nanoparticles with different carbohydrates. The investigations showed that carbohydrates with longer spacer units provided a better immobilization of Con A due to the better accessibility of the mannose rings.[125]

Contrary the fluorescence measurements showed for the different ZnO_2/UDP-Glc nanoparticles a direct correlation between the UDP-Glc sample content and the quantitative immobilization of ConA (Figure 2.4.9b). The fluorescence decreased constantly with decreasing UDP-Glc sample content from 50.4 (ZnO_2/UDP-Glc (1/1)_4min) to 22.0 wt% (ZnO_2/UDP-Glc (10/1)_4min) showing that fewer ConA molecules could be immobilized on the nanoparticle surface. Higher UDP-Glc sample contents did not seem to disturb the immobilization of the lectin like for the Glc-1P stabilized nanoparticles. An explanation could be that the orientation of the UDP-Glc could not be so easily disturbed due to its higher steric demand compared to the Glc-1P. Furthermore the significant intensity differences compared to the reference measurement proved also the specific interaction between the UDP-Glc stabilized nanoparticles and the lectin. Only sample ZnO_2/UDP-Glc (10/1)_4min showed a similar fluorescence compared to the reference measurement indicating a more unspecific interaction via adhesive effects caused through the lower stabilizer content.[124]

To support the assumption that the ConA specifically interacted with the glucose ring of the Glc-1P and UDP-Glc additionally two inhibition measurement was performed for the samples ZnO_2/Glc-1P (4/1)_30c(12min) and ZnO_2/UDP-Glc (1/1)_4min (Figure 2.4.9c and d). The difference to the previous measurements was that different amounts of mannose were added to the measurement solution before the

addition of the ConA. Through the higher specific affinity of the ConA to the mannose than to the glucose a steady decrease of the ConA binding to the nanoparticles should be observed with increasing mannose concentration. The higher affinity of the mannose to the ConA is mostly based on the geometrical position of it's hydroxyl group oxygen atom. For example are eighteen atoms within the ConA binding pocket in a range of 4 Å to this oxygen atom while for the glucose hydroxyl group oxygen atom only five atoms are in the same range. This results in the formation of more extensive van der Waals forces for the mannose causing a higher affinity.[126,127] The fluorescence measurements showed exactly this behavior for the Glc-1P stabilized nanoparticles (Figure 2.4.9c). The fluorescence of the particles decreased with increasing mannose concentration showing that fewer ConA molecules were immobilized on the nanoparticle surface. A critical point was reached at a mannose concentration of 2.22 mM at which the fluorescence decreased strongly. After this point the Glc-1P functionalized nanoparticles showed nearly the same fluorescence like the reference nanoparticles indicating that no ConA was immobilized specifically after this point anymore and that it reacted with the mannose and was washed away during the cleaning process.

The UDP-Glc functionalized nanoparticles showed a similar behavior but the trend was not completely consistent (Figure 2.4.9d). Especially the measurements at mannose concentrations of 2.16, 4.32 and 4.86 mM showed too high intensities. In case of the measurement at mannose concentration of 4.32 mM very high errors were obtained which explained the deviating intensity. Additionally the uridine function could have influenced the interaction between the lectin and the glucose function resulting in some unspecific effects. Such effects could have disturbed the favored interaction of ConA with the mannose molecules compared to the functionalized nanoparticles leading to more immobilized ConA molecules on the nanoparticle surfaces (higher intensities). The fact that higher mannose concentrations were needed in comparison to the Glc-1P stabilized nanoparticles to obtain a competition between the mannose and the UDP-Glc could support this assumption.

These measurements showed that the functionalization of the zinc peroxide nanoparticles with Glc-1P lead to specific interactions with ConA and represents a proof of principal for the application of the nanoparticles in biological systems.

2.4.7 Summary

It was possible to synthesize zinc peroxide nanoparticles stabilized with the biomolecules glucose-1-phosphate (Glc-1P) and uridine 5'-diphosphoglucose (UDP-Glc). Transmission electron microscopy (TEM) measurements revealed that in case of the Glc-1P stabilized nanoparticles the sizes could be influenced via different reaction times (cycle numbers). Nanoparticle diameter between 9.4±5.2 and 5.0±1.5 nm could be obtained by varying the reaction time from 4 minutes to 16 minutes while the smallest particles could be obtained at 12 minutes. The decrease of the nanoparticle sizes and their corresponding standard deviations could be explained by the longer exposure of the particles to the shear and impact forces inside the reaction chamber which caused more abrasion. The contrary diameter increase at 16 minutes however could be contributed to Ostwald ripening. Different precursor:stabilizer ratios had only a slightly influence on the nanoparticle diameter. A significant variation of the particle morphology could only be observed by reducing the sample amount of Glc-1P to 6.08 wt%. At this point also bigger aggregates occurred beside the small and uniform nanoparticles indicating that the Glc-1P amount was not high enough to completely stabilize the particles. Contrary the synthesis of UDP-Glc functionalized nanoparticles always led to a bimodal distribution. Small (<10.0 nm) and bigger nanoparticles (between 17.5±8.7 and 32.6±13.0 nm) could be detected. Additionally the diameter of the small size fraction could be tuned through different initial synthesis ratios. The nanoparticle sizes decreased from 7.0±1.7 to 3.4±1.1 nm with decreasing initial stabilizer concentration while a further stabilizer concentration decrease led again to bigger particles with diameter up to 6.8±2.0 nm. Crystallite size calculation done via Debye Scherrer equations supported the assumptions made based on the TEM images. Crystallite sizes between 1.9±0.3 and 3.3±0.5 nm could be calculated indicating that the obtained ZnO_2/Glc-1P nanoparticles consisted of two or three crystallites each while the small ZnO_2/UDP-Glc nanoparticles mostly consisted of two or three crystallites each while the bigger nanoparticles consisted of approximately nine to sixteen crystallites..

The used biomolecules Glc-1P and UDP-Glc interacted with the nanoparticle surface via their phosphate respectively diphospahte function resulting in a stabilization of the nanoparticles. Solid state 31-phosporous nuclear magnetic resonance measurements (^{31}P-NMR) revealed that the interaction with Glc-1P took place via chemi- and physisorption. Two phosphorous signals occurred with shifts of -3.0 and

+17.6 ppm for the sample spectrum in comparison to one phosphorous signal for the reference spectrum of Glc-1P. The upfield shift (lower ppm) was a sign for the formation of a monodentate bonding between the phosphate function and the nanoparticle surface while the downfield shift (higher ppm) indicated the formation of a hydrogen bonding. Additionally showed the signals of the sample spectrum increased signal widths of 17.63 and 18.02 ppm compared to the reference spectrum signal (signal width 5.43 ppm) caused through a change of the O-P-O bond angle and the presence of different binding sites and modes of the phosphate function. Further die interaction between the UDP-Glc molecules and the zinc peroxide surface could be proven via FTIR measurements. The disappearance of the characteristic P=O stretching vibration of the diphosphate function (1243 cm^{-1}) for the IR sample spectrum indicated a conformational change of this chemical function which was caused through the immobilization of UDP-Glc on the nanoparticle surface.

The investigation of the surface charge of the synthesized nanoparticles via pH dependent zeta potential measurements supported the assumptions made based on the ^{31}P-NMR and FTIR measurements. The differences to the reference measurement of unmodified zinc peroxide proved the immobilization of the Glc-1P and the UDP-Glc. For example showed the measurements for the ZnO_2/Glc-1P nanoparticles a difference in surface charge of approximately 30.00 mV at pH = 2.50 while at a pH value of 8.20 the difference between the modified nanoparticles and the reference zinc peroxide was nearly non existing. The ZnO_2/UDP-Glc nanoparticles showed a similar ampholyte behavior with shifted maximum values of 14.9 and -32.4 mV. This differences could be explained through the decreased number of accessible hydroxide functions on the nanoparticle surface caused through the present Glc-1P and UDP-Glc molecules.

The biomolecules were not only used as stabilizing agents but should also act as linker to biological systems. Thereby can the glucose ring interact specifically with lectins which are present on every cell surface. The interaction of the particles with the model lectin ConA was investigated via fluorescence measurements. The measurements showed that the interaction with the ConA was specific and dependent on the sample composition. For example showed the reference zinc peroxide nanoparticles nearly no immobilization of the ConA, while the Glc-1-P and UDP-Glc functionalized particles showed a significant increase in fluorescence and

immobilization of the ConA. A maximum of immobilized ConA could be achieved for the ZnO_2/Glc-1P nanoparticles at a Glc-1P sample content of 26.38 wt% while with further decrease of Glc-1P the immobilization of the ConA constantly decreased. The same trend was observed for the ZnO_2/UDP-Glc nanoparticles. The fluorescence decreased constantly with decreasing UDP-Glc content from 50.4 to 2.0 wt%. Inhibition measurements showed additionally that the interaction with the ConA was specific. It could be observed that with increasing amount of mannose the fluorescence of the nanoparticles decreased indicating a decreasing immobilization of ConA.

Further the pH induced oxygen release could be proven for both nanoparticle systems. Long time measurements (approximately 7 days) revealed that the nanoparticles released constantly oxygen for approximately four/five days and that the release was dependent on the sample composition, the nanoparticle sizes and the pH value of the dispersion media. The measurements showed for the ZnO_2/Glc-1P nanoparticles that with increasing ZnO_2 sample content (30.53 to 93.91 wt%) and decreasing particle sizes (5.0±1.5 to 4.0±1.2 nm) the oxygen release increased from 1.38 to 2.33 mg/L. Additionally the oxygen release of the ZnO_2/UDP-Glc nanoparticles decreased from 2.04 to 1.47 mg/L with increasing nanoparticle diameter from 3.4±1.1 to 6.8±2.0 nm. It was also proven that with increasing pH value the oxygen release decreased. For example at a pH value of 6.5 a release of 2.06 respectively 1.47 mg/L could be detected while at a pH value of 8.5 the release only accounted 0.39 respectively 0.08 mg/L.

2.5 Antibacterial Activity of ZnO_2 Nanoparticles*

2.5.1 Introduction

The previous investigations proved that the synthesized zinc peroxide nanoparticles are capable of releasing oxygen at moderate conditions (room temperature, pH values of 7.5 and lower). This makes the nanoparticles suitable for biomedical applications.

Oxygen is a crucial element for all living beings and is needed for many biological processes inside biological systems. Especially the growth, production or decomposition of cells is dependent on the presence and concentration of oxygen.[128,129] Preliminary studies showed that different oxygen concentrations stressed different types of cells in different ways. For example prokaryotes like *Escherichia coli* B, *Streptococcus faecalis*, *Saccharomyces cerevisiae* or *Bacillus subtilis* showed a rapid growth inhibition during the exposure to oxygen concentrations of 1, 4.2 and 20 atm of O_2.[130–132] It was concluded that the enzyme aconitase was effected by molecular oxygen which caused a decrease in respiration resulting from a limited electron flow from the substrates to the oxygen.[133] Contrary a successive increase of the cell growth rate of E. coli and an increase of the productivity of the recombinant human growth hormone (rhGH) in E. coli could be achieved at moderate increased oxygen concentrations of 0.40 or 0.93 atm of O_2 revealing the dependence of the cell growth behavior to the oxygen concentration.[134] Eukaryotes on the other hand showed a much higher sensitivity to elevated oxygen concentrations above 0.08 atm of O_2 compared to the prokaryotes.[135,136] For example human myeloid leukemia U-937 cells showed alternation of the mitochondrial respiratory chain, lactate and alanine accumulation and strong growth inhibition at 0.11 atm of O_2. Other studies revealed that the cell growth rate of Chinese hamster ovary (CHO) cells decreased strongly together with a 65% higher glutathione accumulation during the exposure to 0.17 atm of O_2. And for mouse-mouse hybridoma cells a cell growth stop and an association between DNA strand breakage and hyperoxia was observed for oxygen concentrations of 0.42, 0.63 and 0.99 atm of O_2.[136,137]

Beside the influence on the production and growth of cells the oxygen concentration is also crucial for the production of reactive oxygen species (ROS) inside cells. These

*Reproduced from Christian Bergs, Lisa Brück, Ruben R. Rosencrantz, Georg Conrads, Lothar Elling, Andrij Pich; *Biofunctionalized ZnO_2 nanoparticles as active oxygen source and antibacterial agents* (submitted).

species fulfill many different tasks depending on their concentrations. For example can high concentrations of ROS induce autophagy processes by directly modifying proteins like Atg 4, Atg 5 and Beclin. These processes can cause diabetes mellitus, neurodegenerative diseases or different types of cancer.[138,139] But moderate ROS concentrations produced through moderate oxygen concentrations can provide many different beneficial properties. Preliminary studies showed that low levels of ROS act as paracrine signaling mediators which are essential for the proper growth and differentiation of the myocardium.[140–142] Additionally ROS can improve the sensitivity for insulin via the dephoshorylation of phosphatidylinositol-3,4,5-triphospate (PIP3). This regulation is of high importance due to the fact that insulin controls several physiological functions like the glucose metabolism, lipid metabolism and protein synthesis.[143] It also can protect the host from infections through the ROS derived NADPH oxidase which can stop the growth of bacteria.[144–146] These highly flexible ROS are foremost built in vivo inside the mitochondria via a continuous chain reaction mode (Figure 2.5.1).[147]

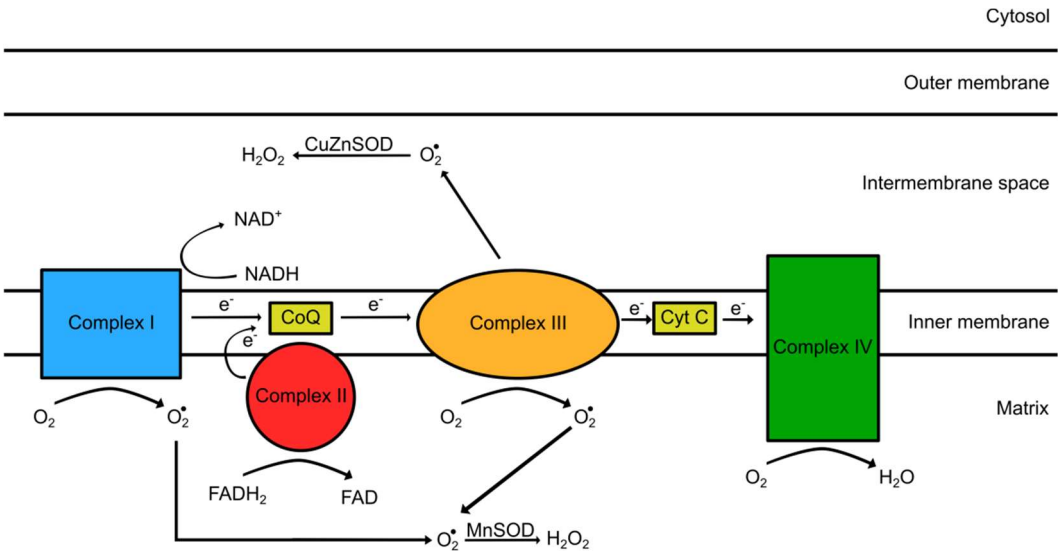

Figure 2.5.1: *Schematic illustration of the ROS formation via respiratory chain inside the mitochondria (MnSOD: manganese superoxide dismutase, CuZnSOD: copper/zinc superoxide dismutase, CoQ: coenzyme Q10, Cyt C: cytochrome C).*[148]

During this reaction the extracellular oxygen diffuses into the cells and abstracts electrons from reduced flavoenzymes which results in the production of reduced oxygen species like superoxide (O_2^-) or hydrogen peroxide (H_2O_2).[149–152] The specific reaction sites are four multiprotein complexes (complex I to IV) which have in total eight reaction sites, from which seven sites liberate the generated ROS into the matrix (innermost membranes of the mitochondria) and one site liberates the ROS

into the intermembrane space.[153,154] The so built ROS can easily cross the mitochondrial membrane through which it can participate more in cellular signaling or biochemical processes.[155]

Furthermore oxygen can act as antibacterial agent against facultative anaerobes and microaerophilic aerobes. Previous studies proved that the bacterial load in infected tissues decreased constantly with increasing oxygen concentration.[156–160] This observation was explained through the metabolization of oxygen into ROS species through the continuous chain reaction mode and leukocytes present in the blood. The transformation of leukocytic superoxide anions to oxygen derivatives like hydrogen peroxide, hydroxyle radicals or oxygen radicals (ROS) is highly oxygen concentration dependent and one of the most important host defenses against bacterial infections.[161] Facultative anaerobes, microaerophilic aerobes but especially obligate anaerobes lack many or even all of the antioxidant defenses like superoxide dismutase, catalase and peroxidase. Therefore ROS species can impair bacterial amino acids, disturb their metabolic substrate transport, inhibit bacterial enzymatic activities by oxidizing the sulphydryl groups of amino acids or stop the bacterial reproduction by blockage of RNA transcriptions and DNA syntheses.[162]

The majority of bacterial infections are treated through antibiotics in our days. These drugs are essential in many medical treatments like chemotherapy, organ transplantation and surgical procedures and reduced the human mortality and morbidity drastically.[163,164] However the number of antibiotic resistant microorganisms increases globally. This resistance can occur through intrinsic effects, mutations in chromosomal genes or horizontal gene transfers.[165] For example can bacteria reduce their cell wall permeability which causes a drug concentration reduction inside the bacterial cells which reduces the drug efficiency.[166,167] Further Gram-negative and -positive bacteria posses transport proteins (effex pumps (EP)) in the cytoplastic membrane. These pumps remove toxic compounds from the bacterial cell without alteration or degradation of the particular molecule. The EP’s can specifically remove one substrate or transport a variety of substances which can increase the antibiotic resistance.[167,168] Another mechanism which increases the resistance is the destruction of the active components of antibiotics. Bacteria can inactivate antibiotics via three different ways: group transfer, redox processes or enzymatic hydrolysis.[163] Among them the enzymatic hydrolysis is the most effective mechanism. A variety of

antibiotics possess hydrolytically sensitive chemical groups like esters and/or amides whose integrity is crucial for their biological activity.[169] Additionally bacteria can increase their resistance through mutations of their target groups. Most of the antibiotics specifically recognize these target groups and even small mutations can lead to a decreased or even inhibited affinity of the antibiotic to the bacterial cell. Such mutations can take place through chromosomal mutations leading to single or multiple amino acid alterations, or homologous recombinations with exogeneous DNA containing gene segments which encode proteins with low antibiotic affinity.[163,170] Further the formation of bacterial biofilms represents a highly effective method against antibiotics. Such biofilms adhere normally to external surfaces and are embedded within an exopolysaccharide matrix.[171] This matrix can consist of ions, extracellular enzymes (proteases, polysaccharases and β-lactamases) and nutrients from the environment. The biofilm itself acts as a diffusion barrier and neutralizer against antibiotics which minimizes the intracellular antibiotic concentration.[172,173] Further the decreasing nutrient gradient between the biofilm surface and its deeper layers influences the metabolic activity of the bacteria resulting in a slower or stationary growth. This growth decrease also influences the efficiency of most antibiotics which cytotoxic properties are directly dependent on the growth rate of the bacteria.[173–175] Additionally the bacterial mutation rates and horizontal gene transmissions are significantly higher in biofilms compared to planktonic bacterial cells, which causes further antibiotic resistances.[176,177]

Therefore new antibacterial materials have to be developed. For example antimicrobial peptides which can disrupt the bacteria cell wall causing leakage of the cellular content were tested on mammalian cells.[178] Further antisense oligonucleotides were used to influence the gene expression directly at the RNA. The nucleotides consist typically of 10-30 residues which are complementary to the mRNA of interest. Thereby the nucleotides can block genes which are essential for the survival of the bacteria.[179,180] Also antibacterial polymers were developed and tested. Polyhexamethylene biguanide (polyhexanide) showed antibacterial properties against Gram-positive and –negative bacteria. The antibacterial activity of the cationic polymer is based on the interaction of the biguanide groups with the cytoplasmic membrane, the lipopolysaccharide and the peptidoglycan of the bacterial cell wall resulting in membrane destabilization and cellular leakage.[181] Especially antibacterial nanomaterials are highly interesting due to their high surface activity.

Recently, functional aqueous nanogels decorated with a controlled amount of surface-drafted antimicrobial isoeugenol molecules have been developed by our group.[182] These nanogels showed antibacterial activity against different Gram-positive and Gram-negative pathogens and cell-adhesive as well as tissue-cell growth promoting properties. The antimicrobial properties of silver have been known to cultures all around the world for many centuries. It is thought that silver atoms bind to thiol groups (-SH) in enzymes and subsequently cause the deactivation of enzymes. Recently, silver nanoparticles with diameter of 7.1±1.2 nm were synthesized via a protein mediated bioreduction and their influence on the growth of *E. scherichia* and *P. seudomonas* was investigated. It could be shown that the antibacterial properties were dependent on the nanoparticle concentration and that the interaction with the bacteria caused rupture of the cell membrane resulting in cell death.[183] Further silver nanoparticles can disrupt the cell envelope, oxidize cell components and inactivate the respiratory chain enzymes, which leads to the production of reactive oxygen species.[184–189] The immobilization of silver and iron oxide nanoparticles on a graphene oxide surface led to an antibacterial nano-compound. The compound material showed higher antibacterial properties against *E. coli* and *S. taphylococcus* compared to pure silver nanoparticles, which was caused through hydrophobic domains on the graphene oxide sheets. This increased the contact between the immobilized silver nanoparticles and the bacteria leading to higher activities. Furthermore laser treatment of the compound material increased the antibacterial properties further through photothermal effects of the immobilized iron oxide nanoparticles.[190–195] Also zinc oxide nanoparticles possess antibacterial properties. Previous studies could show that the activity increased with decreasing nanoparticle diameter and increasing nanoparticle concentrations.[196,197] Smaller particles can more easily adhere to (or even penetrate into) bacterial membranes due to their larger interfacial area which increases the efficiency. Further it was shown that the photocatalytic generation of ROS is the major contributor to the antibacterial properties of zinc oxide nanoparticles. Zinc oxide generates electrons and holes under UV or visible light irradiation which can interact with water forming hydroxyl and/or superoxide anions which can induce bacteria cell death.[198] Another recent antibacterial approach was the synthesis of hollow mesoporous silica nanoparticles loaded with the antituberculosis drug Isoniazid. Particle diameter of approximately 100.0 nm could be achieved and the antibacterial properties against *M. smegmatis*

were investigated. It could be proven that the loaded nanoparticles were more effective compared to the pure drug which was explained through increased intrabacterial accumulation of Isoniazid and the nonspecific adsorption of the positively charged nanoparticles on the negatively charged bacteria. This interaction led to bacteria injury, incomplete cell walls and even cell rupture and death.[199–201]

Functional zinc peroxide nanoparticles represent a promising and nearly uninvestigated oxygen releasing material which could be used for these various oxygen related biomedical applications.

2.5.2 ZnO_2/Glc-1P Nanoparticles as Antibacterial Agents

Glc-1P stabilized zinc peroxide nanoparticles were used for antibacterial proof of principal experiments. To prove their antibacterial properties four pathogenic bacterial species with different degrees of oxygen tolerance were selected: 1) *Enterococcus faecalis*, a gram-positive, facultative anaerobic species which tolerates different atmospheric conditions and is frequently isolated from a variety of infectious processes. It most commonly infect the urinary tract, bloodstream, endocardium, burn and surgical site wounds, abdomen, biliary tract, catheters and other implanted medical devices and is used as pathogenic model organism. It is generally recognized as a robust organism and can be found in the oral cavity attached to implants; 2) *Aggregatibacter actinomycetemcomitans*, a gram-negative, capnophilic and fastidious organism which tolerates and needs a little amount of oxygen (microaerophilic). Together with the species mentioned below it is involved in the initiation and progression of human marginal periodontitis or periimplantitis (inflammation around teeth or titanium implants in the oral cavity); 3) *Porphyromonas gingivalis* and 4) *Prevotella intermedia*, both gram-negative, obligate anaerobic rods with almost no (*P. gingivalis*) or very little (*P. intermedia*) oxygen tolerance. The latter three species (*A. actinomycetemcomitans*, *P. gingivalis* and *P. intermedia*) were chosen because one application of zinc peroxide nanoparticles might be to form a protective layer around the subgingival part of 1) teeth, preventing periodontitis or 2) dental implants, preventing peri-implantitis.

The microbiological results are presented in Figure 2.5.2 for the two tested samples ZnO_2/Glc-1P (2/1)_30c(12min) (50.89/49.10 wt% ZnO_2/Glc-1P) and ZnO_2/Glc-1P

(1/1)_30c(12min) (30.53/69.46 wt% ZnO_2/Glc-1P) with a measurement pH value of 7.4±0.2. The efficiency of the nanoparticles against bacteria was determined through the calculation of the minimum inhibitory concentration (MIC). The MIC is the lowest concentration of an antibacterial agent required to inhibit further growth of a particular bacterium.

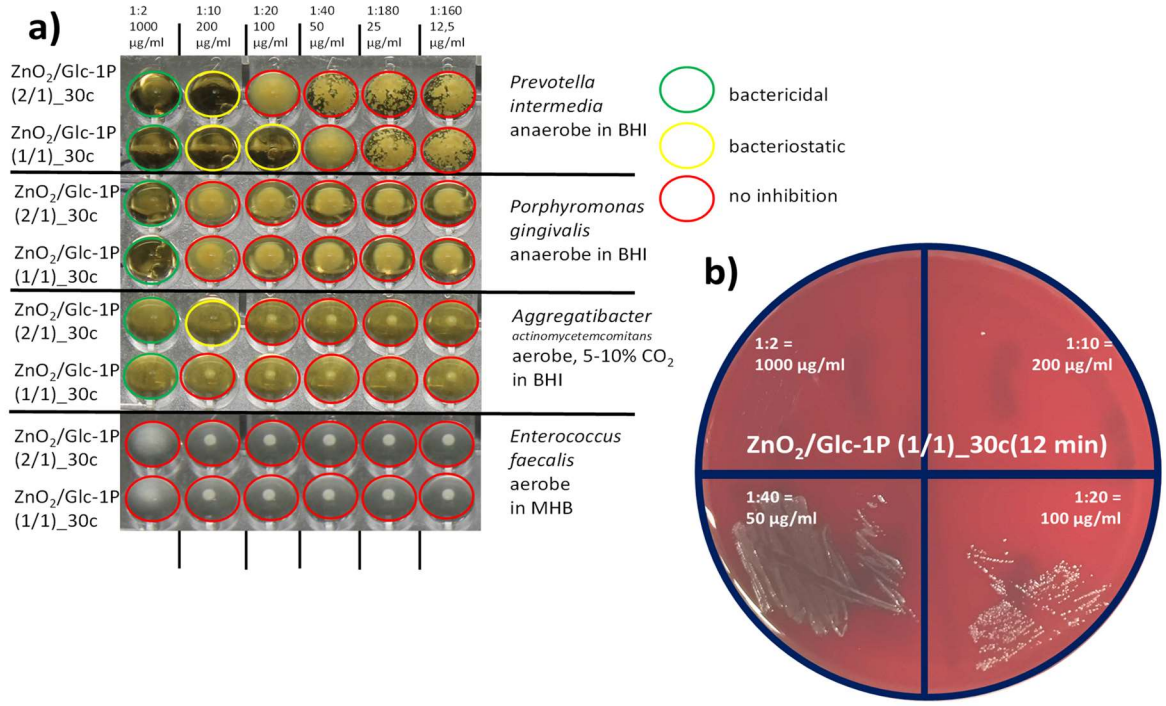

Figure 2.5.2: *Antimicrobial properties of zinc peroxide nanoparticles ZnO_2/Glc-1P (2/1)_30c(12min) and ZnO_2/Glc-1P (1/1)_30c(12min): a) Microbroth dilution testing to determine the minimal inhibitory concentration (MIC) of different zinc peroxide nanoparticles and concentrations by serial dilutions 1:2 - 1:160 (corresponding to 1000 µg/ml – 12,5 µg/ml) in microtiter plates. Test-strains, atmospheric conditions of growth and broth medium (BHI Brain Heart Infusion Broth pH 7.4±0.2; MHB Mueller Hinton Broth, pH 7.4±0.2) are indicated and the circles in different colors indicate complete killing (bactericidal), inhibition (bacteriostatic) or no inhibitory effect. b) Determination and proof of the minimal bactericidal concentration (MBC) of ZnO_2/Glc-1P (1/1)_30c(12min) and Prevotella intermedia as test strain. Striking of 30 µl suspension from the microtiter-wells shown in a) on Trypticase Soy Agar with blood and incubation overnight in appropriate atmosphere disclosed the killing effect of zinc peroxide nanoparticles. In this case, ZnO_2/Glc-1P (1/1)_30c(12min) in a concentration of 1000 µg/ml killed all bacterial cells whereas in a concentration 200 µg/ml (dilution 1:10) a single cell (better: colony forming unit) could still survive.*

Susceptibility to both nanoparticles was not observed for the robust and aero-tolerant Gram-positive species *Enterococcus faecalis*. *Aggregatibacter actinomycetemcomitans* was tested with a minimal inhibitory concentration (MIC) of 200 µg/ml against ZnO_2/Glc-1P (2/1)_30c(12min) and 1000 µg/ml against ZnO_2/Glc-1P (1/1)_30c(12min). *Porphyromonas gingivalis* was tested with a minimal inhibitory concentration (MIC) of 1000 µg/ml against both nanoparticles ZnO_2/Glc-1P

(2/1)_30c(12min) and ZnO_2/Glc-1P (1/1)_30c(12min). The most susceptible species was found to be *Prevotella intermedia*, which was tested with a minimal inhibitory concentration (MIC) of 200 µg/ml against ZnO_2/Glc-1P (2/1)_30c(12min) and even down to 100 µg/ml against ZnO_2/Glc-1P (1/1)_30c(12min). The minimal bactericidal concentration (MBC) for both zinc peroxide nanoparticles was found to be 1000 µg/ml for all fastidious bacterial species but not for *E. faecalis*.

These results are in line with the expectation, that the more aerotolerant (resistant to ROS) a bacterial species is, the more it is tolerant to oxygen releasing nanoparticles. Thus, the most susceptible species can be found among obligate anaerobe species such as *P. gingivalis* and *P. intermedia*. Interestingly, *P. intermedia*, known as slightly more aerotolerant than *P. gingivalis*, was more susceptible (MIC 100-200 µg/ml). This might be due to a higher initial inoculum chosen for *P. gingivalis* (10^5 instead of otherwise 10^4 cells) to guarantee the principal growth of this very fastidious organism. Also unexpectedly, *P. intermedia* was slightly more susceptible against ZnO_2/Glc-1P (1/1)_30c(12min) with a MIC of 100 µg/ml than ZnO_2/Glc-1P (2/1)_30c(12min) with a MIC of 200 µg/ml. This could be evidence for the fact that adherence mediated by the Glc-1P outer layer plays a very important role in the biological activity of the composed nanoparticles as the Glc-1P concentration is 69.46 wt% versus 49.10 wt% and thus 41.4% higher. However, this finding has to be verified with additional obligate anaerobic (both Gram-negative and –positive) bacterial species and further ZnO_2/Glc-1P samples with a varying composition. The antimicrobial tests should also be repeated with different pH values as lower pH increases the oxygen release. However, as a pH of 7.4±0.4 is optimal for most microorganisms the physiological range for testing is rather limited.

3 Incorporation of ZnO_2 Nanoparticles into Recycled PET*

3.1 Introduction

The interest in recycling of polymers like polyesters and polyolefines increased very strongly in the last decades. Poly(ethylene terephthalate) (PET) plays a very important role in the recycling industry. PET is the most important polyester due to its excellent properties like high tensile and impact strength, clarity, good processability, high chemical resistance and high thermal stability. In addition, PET has also very good recycling properties. The great interest in the recycling of PET is, furthermore, influenced by its high consumption. The worldwide usage of PET was $37.85 \cdot 10^6$ tons in 2012 and more than 1.59 million tons of PET were collected for recycling application in 2011.

Different recycling methods for PET are possible such as thermal, chemical and mechanical recycling.[202–205] Mechanical recycling is the most important process in which separated and washed PET wastes are extruded into PET pellets which can be used for further applications like fibers or bottles.[206] For the bottle-to-bottle recycling, the intrinsic viscosity of PET has to be increased. Therefore, a solid-state polycondensation process (SSP) of PET is usually run to increase its intrinsic viscosity. This process increases the molar mass of polyesters by condensation and evaporation of water with ethylene glycol or low weight oligomers as byproducts. High temperatures in the range of 200 and 240 °C and long reaction times of more than eight hours are needed for the SSP process of poly(ethylene terephthalate).[207,208]

However, the recycling of PET with the aid of the SSP process may also lead to problems. In addition to the high costs of the process due to high energy consumptions also increased gray discoloration of the recycled PET (r-PET) occurs, which may cause problems in the production of fibers for white or pastel shade textiles or papers. The discoloration was observed by several authors during the repeated heating of recycled PET.[209–212] The gray discoloration of reprocessed PET is caused mainly by present polycondensation catalysts. In the polycondensation synthesis of poly(ethylene terephthalate) a variety of catalysts are used. More than 90 % of PET is manufactured with the help of antimony compounds.[213–215]

*Reproduced from Dennis Berg, Christian Bergs, Karola Schäfer, Andrij Pich, Martin Möller; *Zinc Peroxide Particles as Bleaching Agents to Improve the Color of Postconsumer Poly(ethylene terephthalate)* (submitted).

Furthermore, titanium compounds like titanium tetraisopropoxide and germanium compounds like GeO_2 are also used as catalysts in PET synthesis.[216–218] The most common antimony catalysts are antimony trioxide (Sb_2O_3), antimony (III) acetate ($Sb[OOC\text{-}CH_3]_3$) and antimony(III) glycolate ($Sb(C_2H_4O_2)_3$).[210,219–223] Especially, antimony(III) compounds (for example Sb_2O_3) can be reduced to elemental gray antimony (Sb^0) during repeated thermal treatment in recycling processes such as SSP process or extrusion processes causing the discoloration of the recycled PET.[210,212] Further reasons for the discoloration of recycled PET during reprocessing could be the presence of pigments, dyes, foreign polymers such as poly(vinyl chloride) (PVC), carbon particles which are used as IR-absorbers or the occurrence of black specs (degraded polymer residues attached to the walls of the equipment).[209,211,224]

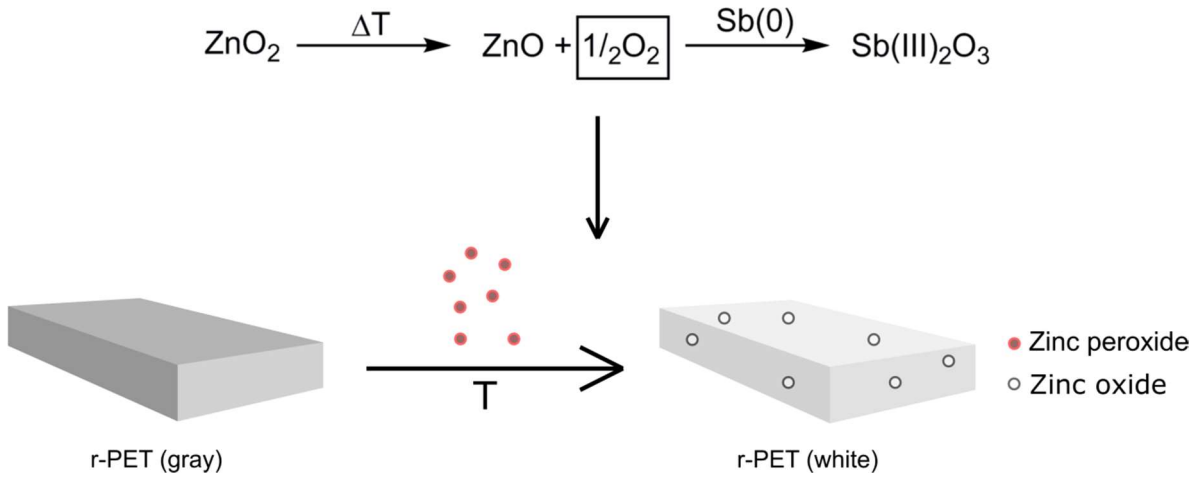

Figure 3.1.1: *Schematic illustration of the decomposition mechanism of the zinc peroxide nanoparticles and the oxidation of the elementary antimony causing the bleaching of recycled PET.*

One possibility to improve the color of recycled PET is the oxidative treatment of the polymer during the extrusion process. The oxidative bleaching of PET can for example be achieved through the use of peroxides but not all peroxides are applicable for the bleaching. For example aqueous hydrogen peroxide solutions cannot be used as polyesters are prone to hydrolysis even if trace amounts of water are present.[221] Organic peroxides like peroxy(di)carbonates, diacyl peroxides, peroxy esters or hydroperoxides could be used but these compounds are thermally unstable and decompose even at lower temperatures and could cause explosions during the decomposition. The used extrusion temperature of 280.0 to 300.0 °C makes the application of these compounds also unlikely. This initial situation led to the investigation of the bleaching potential of inorganic peroxides. These peroxides can

decompose at elevated temperatures under the release of reactive oxygen species and the formation of the corresponding oxide compound. The oxygen can oxidize the elementary antimony while the formed oxide can act as a white pigment which both decreases the discoloration of recycled PET (Figure 3.1.1).

The previous investigations proved that zinc peroxide nanoparticles decomposed at temperatures above 190.0 °C under elimination of specific amounts of oxygen (see section 2.2 and 2.3) which made the synthesized nanoparticles suitable for the bleaching of recycled PET.

3.2 Bleaching of Recycled PET through Oxygen Release

Zinc peroxide nanoparticles stabilized with BMEP and *o*-PEA were used for the bleaching of recycled postconsumer poly(ethylene terephthalate) (r-PET). The zinc peroxide particles should be applied to the melt of PET in the extrusion process which is performed at temperatures of about 300 °C. It could be shown that these nanoparticles release different amounts of oxygen in dependence on the different sample compositions at temperatures above 190.0 °C (see section 2.2). Additionally, macroscopic zinc peroxide ground with a cryomill was used as reference. The zinc peroxide was added as powder in different amounts (0.0 to 1.0 wt%) to the r-PET polymer melt during the extrusion process. The bleaching effect of the different peroxides was determined by colorimetry and color value calculations based on the CIE-L*a*b system. The L, a, and b values represent different color axes which can be used to evaluate the overall color of a material. For example, the L*-value represents the lightness of a material (L*=0 indicates black, L*=100 white), while the a*-value corresponds to the green-red axis, where negative a*-values document green and positive a*-values red materials. Furthermore, the b*-value represents the blue-yellow axis, where negative b*-values document blue and positive b*-values yellow substances.

At first, the bleaching of r-PET in the extrusion process was performed with the ground zinc peroxide reference. The average diameter of the ground zinc peroxide amounted 60.7±51.1 nm and the temperature induced oxygen release lay at 3.2 mmol O_2/g sample (Table 3.2.1). The results of the colorimetry showed that a bleaching effect was achieved (Figure 3.2.1a). A L*-value of 79.1 was measured for

the untreated gray r-PET, while its L*-value decreased to 76.2 after thermal treatment during the extrusion process under nitrogen atmosphere without any additives. Contrary the extrusion of the r-PET with different amounts of zinc peroxide resulted in an increase of the L*-value. For example, the L*-value of r-PET increased from 79.1 to 81.4 with increasing zinc peroxide amount up to 0.2 wt% indicating the bleaching effect of the zinc peroxide.

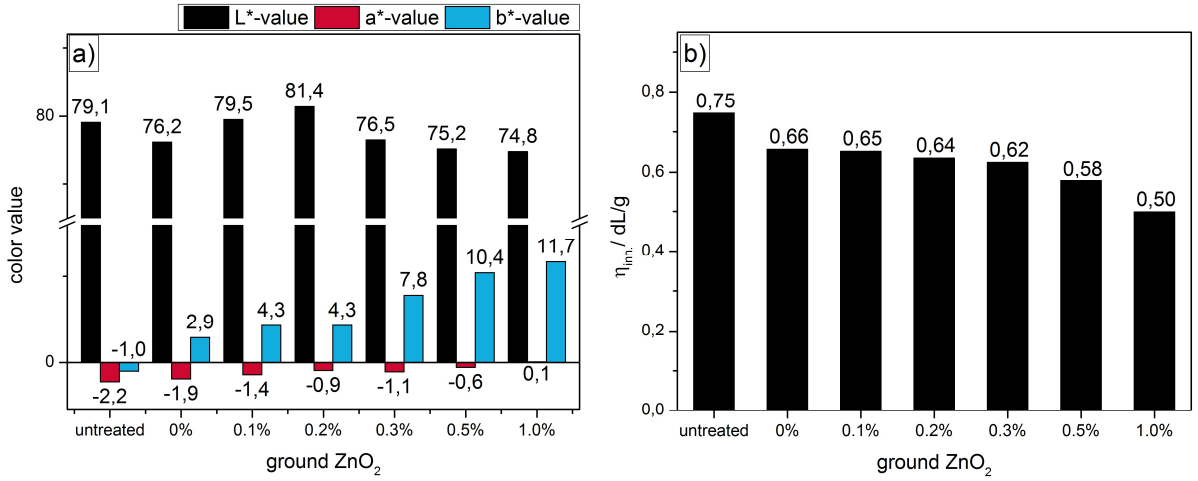

Figure 3.2.1: *Color values (L*-, a*-, and b*-values according to CIE-L*a*b*) (a) and inherent viscosities (b) of a gray reprocessed PET (r-PET) after treatment with different amounts of ground zinc peroxide (0.0 to 1.0 wt%) in the extrusion process in comparison to the untreated r-PET.**

A further increase of the zinc peroxide amount to 1.0 wt%, however, led to a decrease of the L*-value to 74.8 indicating a more colored polymer. The decrease of the L*-value can be explained by the simultaneous increase of the b*-value (from -1.0 to 11.7) with increasing zinc peroxide amount. The increase of the b*-value documented the yellowing of the polymer which suppressed the bleaching effect of the zinc peroxide resulting in lower L*-values. Therefore, only moderate amounts of zinc peroxide have a beneficial effect on the whitening of r-PET.

The increased yellowing of the r-PET with increasing zinc peroxide amount can be explained through the thermally induced degradation of the polymer. The released oxygen did not only oxidize the elementary antimony but did also degrade the r-PET leading to shorter polymer chains and the formation of quinones and stilbene quinones.[225,226] Inherent viscosity measurements supported this assumption (Figure 3.2.1b). While the addition of 0.1 wt% ZnO_2 caused minor degradation of PET ($\eta_{inh.}$= 0.65 dL/g) compared to 0.0 % ZnO_2 ($\eta_{inh.}$= 0.66 dL/g), the addition of higher amounts of ZnO_2 led to stronger degradation (up to 0.50 dL/g).

*These measurements were performed by the cooperation partner and doctoral student colleague Dennis Berg. Additionally these measurements are shown in our joint paper (see footnote on first page of this chapter) and will appear in Dennis Berg's doctoral thesis.

Beside the investigations of the bleaching of r-PET with ground zinc peroxide, studies with zinc peroxide nanoparticles stabilized with *o*-PEA and BMEP were performed. The samples ZnO_2/*o*-PEA (5/1)_20c(8 min) and ZnO_2/BMEP (5/1)_20c_9min with nanoparticle diameters of 2.4±0.7 and 3.3±0.9 nm and oxygen release amounts of 3.5 and 3.7 mmol O_2/g sample (Table 3.2.1) were used for the bleaching experiments due to their similar properties. This allowed the investigation of the influence of different stabilizer molecules on the bleaching effect. The used untreated r-PET showed a L*-value of 76.0 before and 74.7 after the extrusion without the addition of zinc peroxide nanoparticles (Figure 3.2.2a).

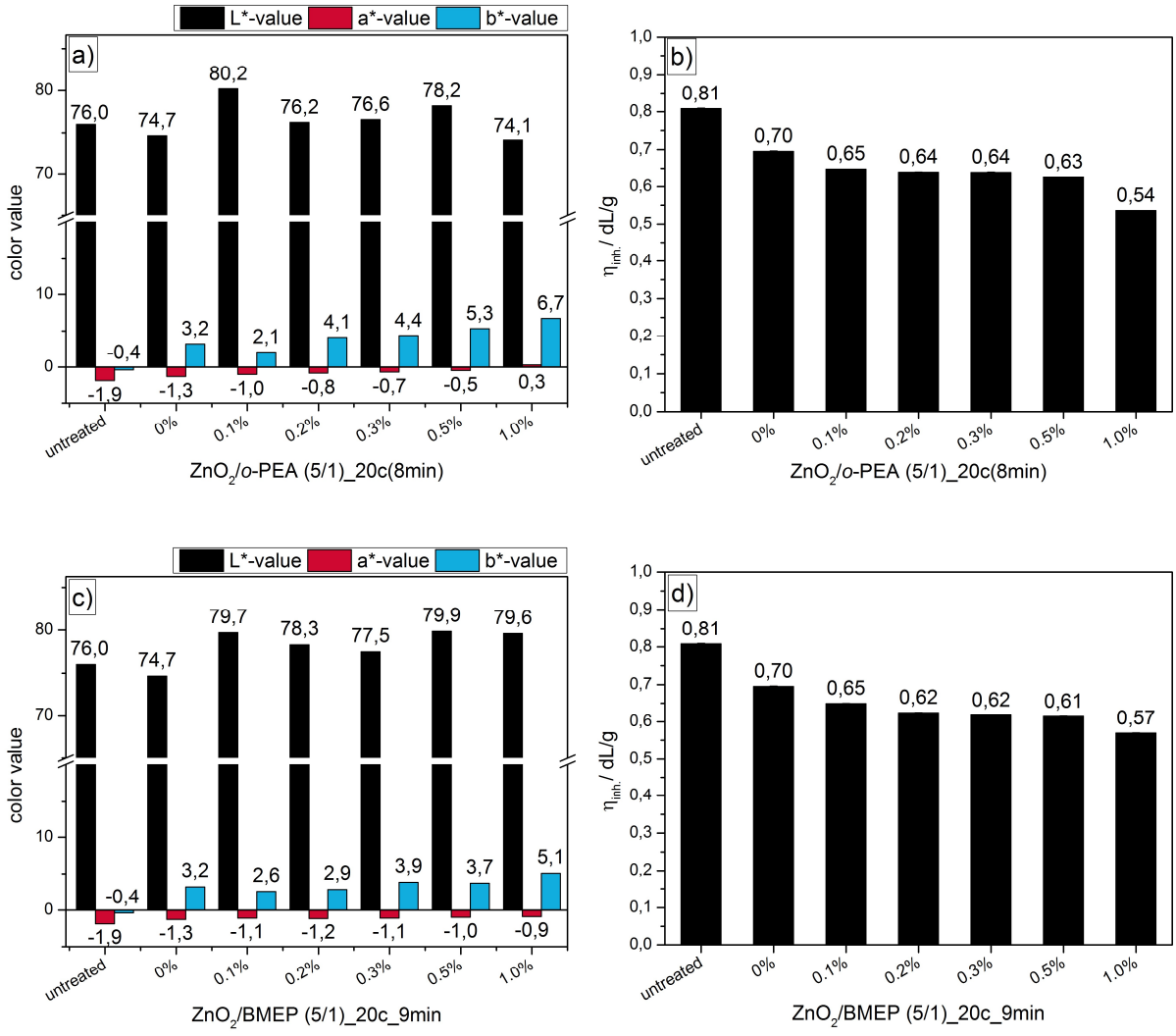

Figure 3.2.2: *Colorimetric results (L*-, a*- and b*-value according to CIE-L*a*b*) of a gray reprocessed PET after treatment with different amounts of zinc peroxide nanoparticles stabilized with o-PEA (0.0 to 1.0 wt%) (a); inherent viscosities of r-PET treated with ZnO_2/o-PEA nanoparticles (b); colorimetric results of r-PET treated with ZnO_2/BMEP nanoparticles (c); inherent viscosities of r-PET treated with ZnO_2/BMEP nanoparticles (d) – all in comparison to the untreated r-PET.**

The addition of 0.1 wt% of ZnO_2/*o*-PEA (5/1)_20c(8 min) during the extrusion process led to an increase of the L*-value to 80.2 (starting from 76.0) while a further increase

*These measurements were performed by the cooperation partner and doctoral student colleague Dennis Berg. Additionally these measurements are shown in our joint paper (see footnote on first page of this chapter) and will appear in Dennis Berg's doctoral thesis.

of the zinc peroxide nanoparticle amount again led to a decrease of the L*-value as already observed for the ground zinc peroxide. This showed the enhanced bleaching activity of the nanoparticles compared to the ground zinc peroxide due to the fact that the addition of 0.1 wt% of ground zinc peroxide resulted only in a L*-value of 79.5 (starting from 79.1). These observations could be explained by the better distribution of the nanoparticles in the r-PET melt and the higher oxygen release of the nanoparticles. Furthermore, no consistent trend could be observed for the L*-value which could be due to the presence of the stabilizer *o*-PEA. This compound decomposes at temperatures above 263.9 °C which could influence the L*-value of PET negatively. Additionally, an increase of the b*-value from 2.1 to 6.7 was observed for increasing zinc peroxide contents like for the ground zinc peroxide. However, the yellowing effect of the nanoparticles stabilized with *o*-PEA was weaker compared to the ground sample. For example a b*-value of 2.1 was measured for PET after bleaching with 0.1 wt% ZnO_2/*o*-PEA (5/1)_20c(8 min), while already a b*-value of 4.3 was obtained for the bleaching with 0.1 wt% ground zinc peroxide. This indicated that a smaller amount of the r-PET polymer chains were decomposed during extrusion with added ZnO_2 nanoparticles. Inherent viscosity measurements were performed to investigate the degradation of the r-PET caused by the presence of ZnO_2/*o*-PEA nanoparticles (Figure 3.2.2b). The assumption that fewer polymer chains were decomposed by the nanoparticles compared to the ground zinc peroxide could not be fully confirmed. Higher inherent viscosities were only obtained for the polymers extruded with higher amounts of zinc peroxide nanoparticles (0.3, 0.5 an 1.0 wt%).

Table 3.2.1: *Particle diameter, sample compositions and oxygen release amounts of the different zinc peroxide samples used for the bleaching experiments.*

Sample	Particle diameter [nm]	Sample composition [wt%/wt%]	Oxygen release [mmol O_2/g sample]
Ground ZnO_2	60.7±51.1	100/-	3.2
ZnO_2/*o*-PEA (5/1)_20c(8 min)	2.4±0.7	68.1/31.9	3.5
ZnO_2/BMEP (5/1)_20c_9min	3.3±0.9	71.5/28.5	3.7

The zinc peroxide nanoparticles stabilized with BMEP showed a comparable but more consistent bleaching effect as the nanoparticles stabilized with *o*-PEA (Figure

3.2.2c). The L*-value of r-PET increased from 76.0 to a maximum of 79.9 after extrusion with a zinc peroxide content of 0.5 wt%. Furthermore the L*-value did not decrease strongly with increasing nanoparticle content as in case of the *o*-PEA stabilized nanoparticles. An explanation could be that the slightly higher oxygen release of 3.7 mmol O_2/g sample combined with the weaker increase of the b*-value from 2.6 to 5.1 (instead of 2.1 to 6.7 for the ZnO_2/*o*-PEA samples). The overall lower b*-values indicated a less pronounced decomposition of r-PET which could not be proven through inherent viscosity measurements (Figure 3.2.2d). The measured viscosities were in most cases lower compared to the viscosities of the polymers treated with nanoparticles stabilized with *o*-PEA. Another explanation for the lower b*-values could be a different decomposition behavior of the stabilizer BMEP (start at T=208.2 °C) compared to *o*-PEA which has minor influence on the yellowing of r-PET.

3.3 Summary

The beneficial influence of zinc peroxide on the bleaching of r-PET could be proven by colorimetry measurements. Ground zinc peroxide and zinc peroxide nanoparticles stabilized with *o*-PEA or BMEP were used during the extrusion of r-PET and the influence of their oxygen release on the bleaching of the polymer investigated. It could be shown that the L*-value (whiteness) of the r-PET could be improved through the addition of zinc peroxide. The values increased from 79.1 respectively 76.0 to maximum values of 81.4 (ground ZnO_2), 80.2 (ZnO_2/*o*-PEA) and 79.9 (ZnO_2/BMEP). It could be shown that the overall L*-value increase was higher for the nanoparticles than the ground zinc peroxide caused through the better distribution of the nanoparticles inside the polymer melt and the increased oxygen release. Additionally the influence of different amount of zinc peroxide on the bleaching of r-PET was investigated. It could be shown that with increasing zinc peroxide amount (0.1 to 1.0 wt%) the L*-value decreased in most cases (except for the ZnO_2/BMEP samples). Simultaneously the b*-value increased constantly. This behavior could be explained through the decomposition of the r-PET. The oxygen released from the particles did not only oxidize the elementary antimony (responsible for the discoloration of the r-PET) but also decomposed the r-PET resulting in a yellowing of the polymer (higher b*-values). The higher b*-values subsequently influenced the L*-values negatively.

Inherent viscosity measurements were performed to investigate the decomposition of the r-PET. The measurements revealed that with increasing amount of zinc peroxide the viscosity of the polymer decreased indicating the presence of shorter polymer chains caused through its decomposition. The investigations revealed that moderate amounts of zinc peroxide nanoparticles (0.1 or 0.2 wt%) increased the whitening of the r-PET while the degradation of the polymer could be reduced to a minimum. Additionally the *o*-PEA stabilized nanoparticles showed the best results of all samples with a L*-value of 80.2 and a b*-value of 2.1 at the lowest zinc peroxide amount of 0.1 wt%.

4 Incorporation of ZnO_2 Nanoparticles into Microgels

4.1 Introduction

4.1.1 Microgels: Structures, Syntheses and Properties

Microgels can be defined as colloidal polymer particles consisting of intramolecular cross-linked polymer networks with particle sizes between 10 and 1000 nm.[227] The cross-linked structure provides characteristically different properties like swelling capabilities in suitable solvents and topological integrity compared to common colloidal polymer particles like latex particles.[228–230] The most common crosslinker for microgel formation is the bifunctional monomer N, N'-methylenebisacrylamide (BIS) which has in most cases a higher reactivity than the used main monomers which results in it's faster conversion. This leads to an inhomogeneous distribution inside the microgels. Investigations could prove that the cross-linker concentration decreased from the core to the surface of the microgel.[227,230–232] Further the cross-linked nature of the microgels causes volume phase transition properties induced through environmental changes like temperature, pH, type of solvent, ionic strength or surfactants present in the dispersion (Figure 4.1.1a).[233–239] For example microgels consisting of poly(N-isopropylacrylamide) (PNIPAm) or poly(N-vinylcaprolactam) (PVCL) change their sizes drastically at elevated temperatures close to the lower critical solution temperature (LCST) of the corresponding linear polymer.[240,241] This characteristic point is known as the volume phase transition temperature (VPTT) of microgels. A typical microgel is swollen by solvent (for example water) at temperatures below the VPTT, while the microgel shrinks at temperatures above the VPTT due to water ejection caused through hydrogen bond cleavages between water and the polymer and increased hydrophobic interactions.[240,242] Additionally microgels which contain charged groups can be sensitive to pH variations of the dispersion media. For example can microgels containing the co-monomer vinylimidazole (VIm) be ionized through a pH decrease from 6.0 to 4.0 which causes higher swelling degrees due to increasing repulsions between the positive charged groups.[243]

Typical microgel synthesis approaches can be distinguished in three different classes: 1) the polymerization from monomers and cross-linkers in homogenous phase or micro-droplets, 2) post crosslinking of already synthesized polymers in

homogenous phase or micro-droplets, 3) mechanical grinding of synthesized macrogels.[227] The most controllable way to synthesize microgels is the polymerization of monomers and cross-linkers while such reactions are normally initiated through ionic radical initiators. Two of the most frequently used initiators are the cationic molecule 2, 2'-azobis(2-methylpropionamidine) dihydrochloride (AMPA) and the anionic molecule 2, 2'-azobis(N-(2-carboxyethyl)-2-methyl-propionamidine) (ACMA). For example AMPA is an effective initiator for the synthesis of nonionic microgels while ACMA is more preferred for the synthesis of anionic microgels due to the possible coagulation of AMPA molecules with anionic co-monomers.

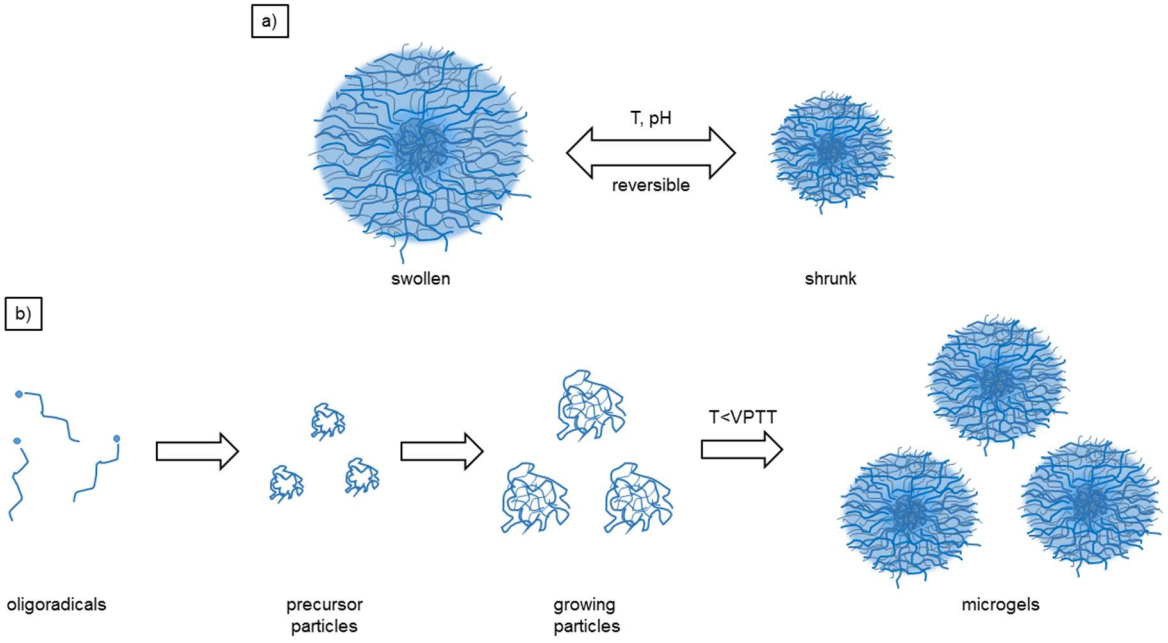

Figure 4.1.1: *Schematic illustration of the phase transition behavior of typical microgels (a); postulated microgel formation via precipitation polymerization (b).*[244]

The temperature-responsive microgels (PVCL and PNIPAm based microgels) used for this study were synthesized via precipitation polymerization, which represents an easy and highly versatile way to synthesize different types of microgels. It provides good control over parameters like particle size, cross-linking-density, particle charge and polydispersity.[243,245–249] Such a polymerization is carried out at temperatures between 50 and 80 °C at which the used initiator decomposes into free radicals which can attack the monomers initiating the polymerization.[250] Further the used reaction temperature is much higher than the LCST of the formed polymers (32 °C for both PVCL and PNIPAm) which leads to their precipitation when a critically chain length is reached.[227,251,252] The so formed precursor particles can grow in two

different ways: through aggregation with other precursor particles forming larger stable colloids and/or through the addition of other monomer or macroradical molecules. Additionally these growing particles are shrunk and electrostatically stabilized during the synthesis. After the polymerization the microgels change to a swollen state during the cool down and their colloidal stability is mostly influenced through the formation of hydrogen bonds between the polymer and the water molecules (Figure 4.1.1b).[228,242]

PVCL and PNIPAm based microgels were intensively investigated over the last few years and can especially be used for application fields like pharmacy, therapeutics and biomedicine due to their biocompatibility and low cytoxicity.[253–255] Furthermore the modification of such microgels was possible through the incorporation of different co-monomers like acetoacetoxyethyl methacrylate (AAEM), acrylic acid (AAc), vinylimidazole (VIm), vinylpyridine, poly(ethylenglycol)-methylethermethacrylate (PEGMA), itaconic acid, N-succinimidyl methacrylate (Suma) or poly(2-methoxyethyl acrylate) (PMEA).[256–264]

For example were pure PVCL-microgels used as carrier systems for drugs like Nadonol, Propranolol and Tacrine.[265] It was shown that the drugs influenced the swelling behavior of the microgels and their thermosensitivity. The Nadolol loaded microgels showed no VPPT anymore while the Propranolol and Tacrine loaded microgels still possessed a VPPT at approximately 30 °C. Further it could be proven that the modified microgels released the drugs constantly for at least 6h and that the interaction between the polymer and the drugs was mostly dependent on hydrophobic and coulombic interactions. Additionally Suma modified PVCL-nanogels proved to be excellent carriers for Doxorubicin (DOX). 91.3 % of the used DOX was bound covalently to the nanogel through coupling with succinimide groups while 8.7 % were immobilized via electrostatic interactions with the carboxyl function of the hydrolyzed esters of the nanogel. It was postulated that the physisorbed DOX could be released in the endosome/lysosome pathway due to increased acidic conditions while the chemisorbed DOX could only be released in the cytosol (target) caused through nanogel degradation due to high glutathione concentrations.[263] Previous studies also presented the synthesis of PVCL/PMEA core-shell-microgels. These colloidal particles could be efficiently endocytosed into HeLa (epithelial cells derived from cervical cancer) cells without altering their viability. Flow cytometric analysis

proved that the unspecific cellular uptake of the modified microgels significantly increased compared to pure PVCL based microgels which is essential for possible drug delivery applications.[264]

Also PNIPAm microgels have been extensively studied in the context of drug delivery. The influence of different functional co-monomers like acrylic acid (AAc), methacrylic acid (MAA), vinylacetic acid (VAA), and fumaric acid (FA) on uptake of different drugs and releases was investigated. It could be observed that the uptake efficiency was dependent on the charge of the microgel respectively of the drug. Further the incorporation of different types and amounts of drugs led to a decrease/increase of the microgel diameter depending if the drug was incorporated into the shell or the core of the microgel.[266] Further the glucose/temperature triggered drug release from poly(N-isopropylacrylamide-co-3-acryl-amidophenylboronic acid) (PNIPAm-PBA)) microgels was investigated. Alizarin red S (ARS) and FITC-insulin were loaded into the micogels and a release increase could be observed with increasing temperature from 15 to 37 °C and with increasing glucose concentration from 0.0 to 50.0 mM. Higher temperatures caused shrinking of the microgels which induced a “squeeze-out” effect while at higher glucose concentrations a binding competition between the glucose respectively drug molecules to the PBA functions of the polymer occurred. The drugs were released due to the higher affinity of the glucose to PBA functions.[267]

These examples show clearly that the biocompatible PVCL and PNIPAm based microgels were good candidates for the incorporation of functionalized zinc peroxide nanoparticles for biomedical applications.

4.1.2 Nanoparticle Immobilization in Microgels

The incorporation of nanoparticles into polymeric structures like microgels has diverse beneficial effects. For example can new functionalities introduced to the microgel, while the cytotoxicity of many nanoparticles can be drastically reduced through their immobilization into polymers. Further the formation of such composite materials offers versatile possibilities for the coating of implants, scaffolds, stents or other carrier structures. Three different microgel/nanoparticle composites can be distinguished: 1) core-shell structures in which the core consists of one or several

nanoparticles which are coated with a microgel-shell, 2) microgels which are loaded statistically with nanoparticles, 3) microgels which are covered with nanoparticles on their most outer shell region.[268] These composites can mainly be synthesized via two different synthesis approaches. On the one hand the nanoparticle precursor can be immobilized in the microgels followed by its in situ precipitation resulting in nanoparticle formation and on the other hand already synthesized nanoparticles can be incorporated into already synthesized microgels (Figure 4.1.2).[244,268] The binding of the nanoparticles can be achieved via chemisorption and/or physisorption.

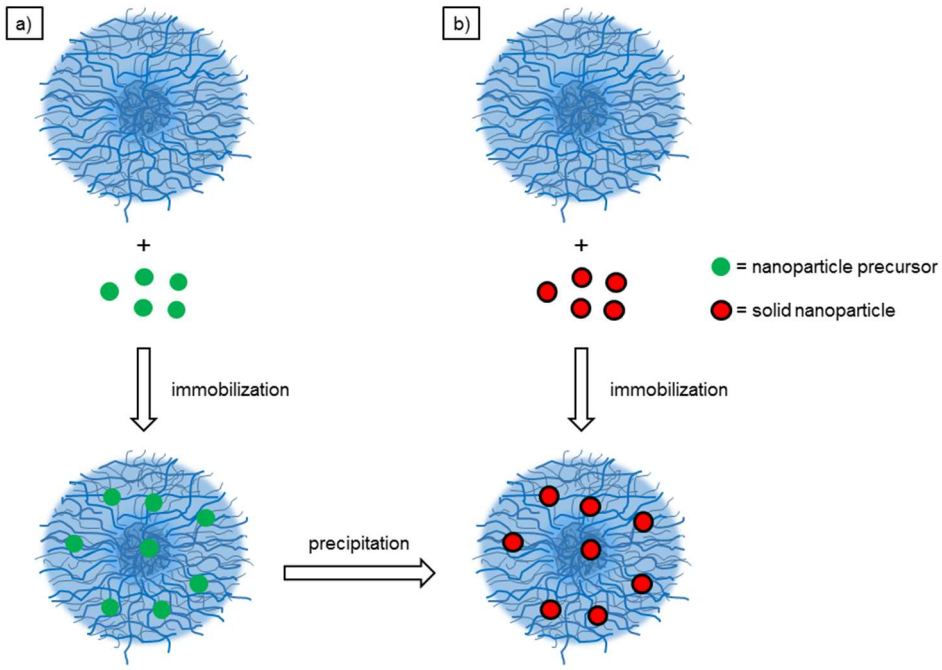

Figure 4.1.2: *Synthesis methods for microgel/nanoparticle composite materials: a) in situ synthesis via precursor precipitation; b) immobilization of pre synthesized nanoparticles.*

Typical examples for the in situ synthesis of nanoparticles inside microgels are the formation of gold, silica or palladium nanoparticles inside different microgel types.[246,269,270] Gold nanoparticles were successfully synthesized in poly(N-vinylcaprolactam-co-acetoacetoxyethyl methacrylate-co-acrylic acid) P(VCL-AAEM-AAc) microgels through the incorporation and reduction of the precursor $HAuCl_4$. It could be proven that the nanoparticle content could be tuned through the initial amount of precursor. Furthermore the precursor reduction was auto-initiated trough the microgel itself via its AAEM functions present in the microgel core. It was postulated that the β-diketone groups of AAEM created a potential reducing environment provided by electron rich oxygen atoms due to keto–enol tautomerization.[271] Further these composites were used for the catalytic reduction of

p-nitrophenol to *p*-aminophenol which represents a highly important substance for the preparation of photographic developers, corrosion inhibitors, wood-staining agents or antipyretic drugs.[272–275] Contrary silica nanoparticles could be synthesized inside poly(N-isopropylacrylamide-co-2-(dimethylamino) ethyl methacrylate) (poly(NIPAm-co-DMC)) microgels. The investigations showed that the silica nanoparticles were mostly formed inside the shell of the microgel with diameter between 5 and 10 nm. This preferred orientation took place due to the DMC functions mostly present in the microgel shell which catalyzed the silicification of the nanoparticle precursor tetramethyl orthosilicate. The so formed composite particles did not show any VPPT anymore, which was used for the immobilization of the drug aspirin. Modified and unmodified microgels showed similar drug loading contents, but the silica containing microgels released the drug constantly for at least 24h while the unmodified microgels released the complete aspirin already after 5h. In this case the silica nanoparticles acted as a barrier against the incorporated drug.[269] Further PNIPAm microgels were used as carriers for palladium nanoparticles. The precursor $PdCl_4^{2-}$ was immobilized inside the microgel through the interaction between its metal ion and the nitrogen atoms of the polymer backbone. The reduction of the precursor led to the deposition of uniform palladium nanoparticles with diameter of 3.8 nm which showed a catalytic activity for the reduction of *p*-nitrophenol.[270]

To incorporate already synthesized nanoparticles into polymeric structures, complementary functional groups must be present on the nanoparticle surface respectively in the polymer backbone. Therefore the choice of nanoparticle stabilizer and type of polymer is crucial for the successful nanoparticle incorporation. For example were photoluminescent europium-doped lanthanum fluoride nanoparticles (LaF_3:Eu-AEP) incorporated into poly(N-vinylcaprolactam-co-glycidyl methacrylate) (PVCL/PGMA) microgels via covalent coupling. The nanoparticles were stabilized with 2-aminoethyl phosphate which interacted with the nanoparticle surface through its phosphate function while the free primary amine could couple with the epoxide functions of the GMA blocks present in the polymer structure. It could be shown that the amount of immobilized nanoparticles was dependent on the GMA content of the microgel. Microgels with lower amounts of GMA provided better conditions for the nanoparticle immobilization due to nanoparticle diffusion processes inside the microgel. The nanoparticles got trapped in the shell of the microgel at high GMA contents, which led to the formation of obstacles causing nanoparticle immobilization

limitations. Further the incorporation of the nanoparticles induced microgel contraction most probably due to the covalent linking to the polymer backbone.[276] Also pre-synthesized gold nanoparticles could be incorporated into polymeric structures. Citrate stabilized nanoparticles with diameter of 4.0 nm mostly physisorbed onto thermoresponsive PNIPAm brushes via the formation of hydrogen bonds between the amide groups of the PNIPAm and the carboxylate functions present on the nanoparticle surface. The investigations showed that the composite brushes collapsed upon heating at temperatures above the LCST which caused a red shift of the gold plasmon band. This phenomenom was explained through the decrease of the interparticle distance in collapsed state.[277]

4.2 Incorporation of ZnO_2 Nanoparticles into Microgels

Two different stabilized zinc peroxide nanoparticles were used for proof of principal incorporation into two different types of microgels. The nanoparticles ZnO_2/*o*-PEA (5/1)_20c(8 min) and ZnO_2/citrate (5/1)_20c(8min) were immobilized into PVCL/GMA- respectively into PNIPAm microgels. The PVCL/GMA microgels contained 10 mol% of glycidyl methacrylate functions (GMA) which could react with the primary amine functions present on the ZnO_2/*o*-PEA nanoparticle surface resulting in covalent bonds between the nanoparticles and the polymer.[276] Further these GMA functions were mostly located in the microgel core, which should result in the preferred nanoparticle immobilization in this domain. Contrary the ZnO_2/citrate nanoparticle incorporation into PNIPAm microgels was driven by electrostatic processes (physisorption) between the carboxylate functions present on the nanoparticle surface and the amide groups of the PNIPAm backbone. This interaction should mostly take place through the formation of hydrogen bonds like already observed for similar systems.[277] Additionally a statistical nanoparticle distribution should be achieved inside the PNIPAm microges due to amide groups present in the whole microgel (Figure 4.2.1)

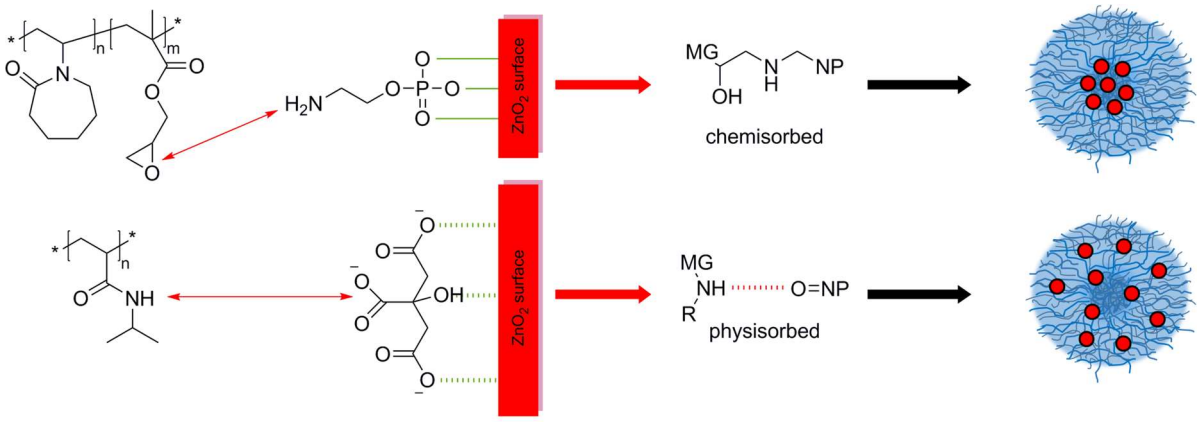

Figure 4.2.1: *Schematic illustration of the interaction between the two different nanoparticles and micorgel types and the resulting postulated nanoparticle distribution inside the different microgels.*

The nanoparticle incorporation was achieved for both systems through mixing of the corresponding reactants at room temperature for 24h. The experiments were performed in tris(hydroxymethyl)-aminomethan buffer (TRIS, pH = 10.2) to make sure that no nanoparticle decomposition occurred while abundant nanoparticles were separated via dialysis after the incorporation. Different amounts of nanoparticles were used (10, 50 and 100 wt% related to the microgel mass) and the influence on the incorporation and the microgel properties was investigated. TGA measurements revealed that different amounts of nanoparticles could be immobilized inside the microgels for both systems, depending on the initial nanoparticle amount (Figure 4.2.2, Table 4.2.1).

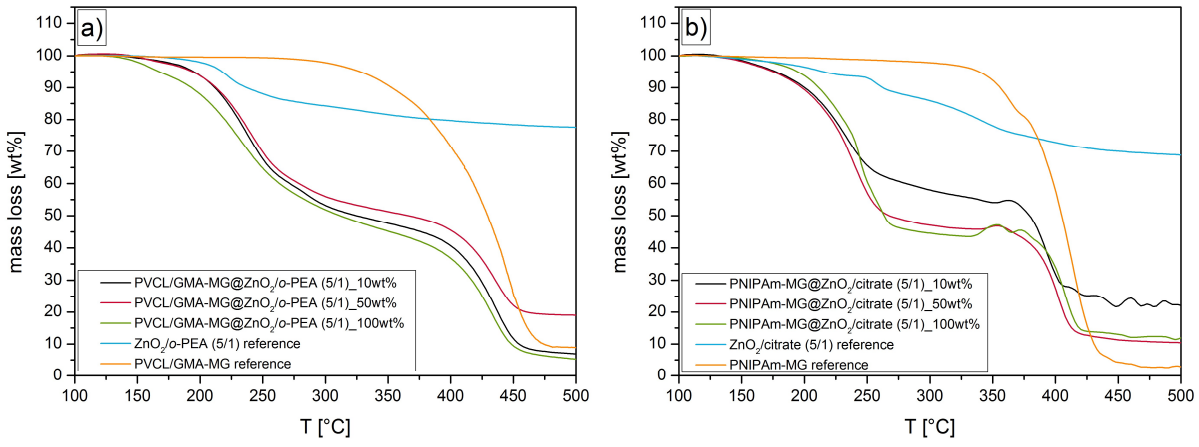

Figure 4.2.2: *Thermogravimetric analysis of the two different microgel/nanoparticle composites: PVCL/GMA microgels with different ZnO_2/o-PEA nanoparticle contents (a); PNIPAm microgels with different ZnO_2/citrate nanoparticle contents (b). Measurements were carried out under nitrogen.*

The measurements showed for all composites two different decomposition steps which could be used for the calculation of the nanoparticle respectively the microgel content of the different samples. For example showed the different

PVCL/GMA@ZnO_2/*o*-PEA samples a first decomposition step at 205.5 (10 wt%), 211.3 (50 wt%) and 204.5 °C (100 wt%) which could be assigned to the decomposition of the ZnO_2/*o*-PEA nanoparticles (T=203.5 °C) incorporated into the microgels (Figure 4.2.2a). The slight shift to higher decomposition temperatures could be explained though the protective polymer around the nanoparticles. Further a second decomposition step at 408.6 (10 wt%), 416.2 (50 wt%) and 406.9 °C (100 wt%) could be detected, which was characteristic for the decomposition of the PVCL/GMA microgel (T=388.0 °C). The shift to higher temperatures could be caused through stabilization effects of the ZnO nanoparticles formed through ZnO_2 decomposition. The PNIPAm@ZnO_2/citrate samples showed similar trends. Decomposition steps at 200.0/381.5 (10 wt%), 208.8/387.6 (50 wt%) and 224.8/334.0 °C (100 wt%) could be measured, which were again allocated to the ZnO_2/citrate nanoparticle (T=195.4 °C) respectively PNIPAm microgel (T=378.4 °C) decomposition (Figure 4.2.2b). Only sample PNIPAm@ZnO_2/citrate (5/1)_100wt% showed more deviated values compared to the reference substances.

Table 4.2.1: *Sample compositions, hydrodynamic radii (r_H) and polydispersity indices (PDI) for the different PVCL/GMA@ZnO_2/o-PEA and PNIPAm@ZnO_2/citrate samples and the corresponding reference microgels.*

sample	Sample composition MG/NP [wt%/wt%]	rH [nm]	PDI
PVCL/GMA@ZnO_2/o-PEA (5/1)_10wt%	65.4/34.6	292.8	0.20
PVCL/GMA@ZnO_2/o-PEA (5/1)_50wt%	62.5/37.5	309.0	0.28
PVCL/GMA@ZnO_2/o-PEA (5/1)_100wt%	56.1/43.9	291.9	0.19
PVCL/GMA reference	100/0	266.2	0.05
PNIPAm@ZnO_2/citrate (5/1)_10wt%	59.4/40.6	178.5	0.22
PNIPAm@ZnO_2/citrate (5/1)_50wt%	53.6/46.4	197.2	0.28
PNIPAm@ZnO_2/citrate (5/1)_100wt%	47.5/52.5	191.8	0.27
PNIPAm reference	100/0	156.7	0.06

The sample content calculations based on these decomposition steps revealed that the content of immobilized ZnO_2/*o*-PEA nanoparticles inside the PVCL/GMA microgels increased from 34.6 to 43.9 wt% with increasing initial nanoparticle amounts from 10 to 100 wt% (in relation to the initial microgel amount). These data

revealed that the nanoparticle content could be tuned through the initial reactant ratios, but that no direct correlation occurred. Lower respectively higher nanoparticle contents were expected for the 10 respectively 100 wt% loadings. An explanation could be that the oxygen released during the zinc peroxide decomposition initiated partial polymer degradation which could have influenced the microgel respectively nanoparticle content calculations. Further investigations have to be performed to validate this assumption. The TGA measurements of the PNIPAm@ZnO_2/citrate samples showed similar trends. A nanoparticle content increase from 40.6 to 52.5 wt% could be observed with increasing initial nanoparticle amounts from 10 to 100 wt%. The lower nanoparticle contents of the PVCL/GMA@ZnO_2/*o*-PEA samples compared to the PNIPAm@ZnO_2/citrate samples could be explained through the GMA position inside the corresponding microgels. These functional groups were only located inside the microgel core which complicated the nanoparticle diffusion towards them, influencing their immobilization. Contrary the necessary amide functions for the ZnO_2/citrate nanoparticle immobilization were statistically distributed over the whole PNIPAm microgel which facilitated the immobilization leading to higher nanoparticle contents.

Furthermore the influence of different nanoparticle loadings on the hydrodynamic radii (r_H) and polydispersities (PDI) of the corresponding microgels was investigated for both systems via dynamic light scattering measurements (Figure 4.2.3, Table 4.2.1). The measurements proved that the hydrodynamic radii as well the PDI's increased with increasing nanoparticle loading up to 37.5 (PVCL/GMA@ZnO_2/*o*-PEA) respectively 46.4 wt% (PNIPAm@ZnO_2/citrate) compared to the corresponding unmodified microgels. Hydrodynamic radii from 266.2 to 309.0 nm and PDI's from 0.05 to 0.28 could be detected for the PVCL/GMA@ZnO_2/*o*-PEA samples while the measurements of the PNIPAm@ZnO_2/citrate samples revealed radii from 156.7 to 197.2 nm and PDI's from 0.06 to 0.28. The radii increase was caused through room demanding effects of the nanoparticles which increased with nanoparticle loading. Surprisingly the two samples with the highest nanoparticle contents of 43.9 (PVCL/GMA@ZnO_2/*o*-PEA (5/1)_100wt%) and 52.5 wt% (PNIPAm@ZnO_2/citrate (5/1)_100wt%) showed decreased radii (291.9/191.8 nm) and PDI's (0.19/0.27) compared to the corresponding 50wt%-samples which was contrary to the other data. Additionally indicated the increased PDI's of all composites that the microgels were not consistently loaded with nanoparticles leading to more polydisperse microgels.

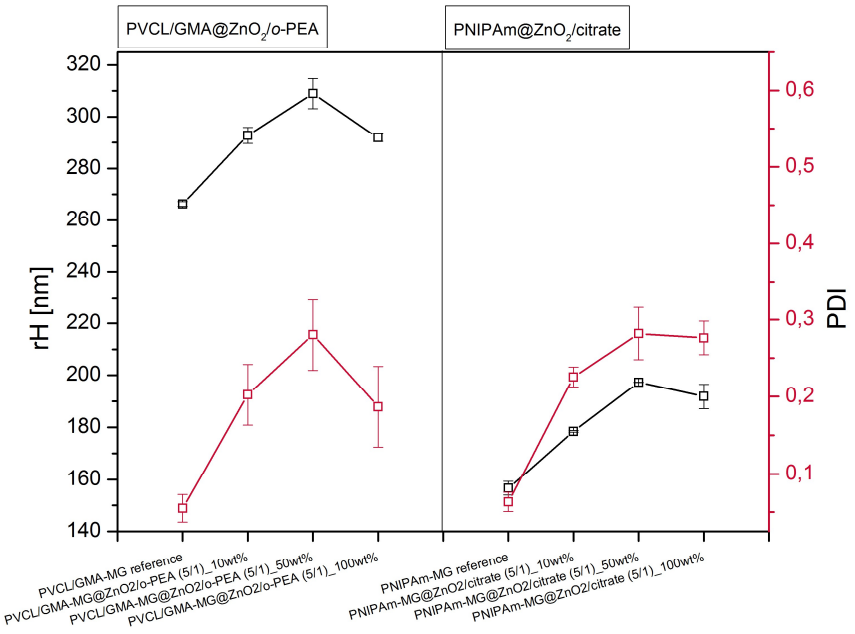

Figure 4.2.3: *Dynamic light scattering measurements for the different PVCL/GMA@ZnO_2/o-PEA and PNIPAm@ZnO_2/citrate samples and the resulting hydrodynamic radii and PDI values in comparison to the unloaded microgels.*

Further the influence of the nanoparticle loading on the temperature responsive properties of the two different microgel types was investigated via temperature dependent dynamic light scattering measurements. The two samples with highest nanoparticle loading (PVCL/GMA@ZnO_2/*o*-PEA (5/1)_100wt% and PNIPAm@ZnO_2/citrate (5/1)_100wt%) were chosen for the representative measurements in comparison to the corresponding unmodified microgels. The measurements were carried out at temperatures between 15.0 and 50.0 °C in aqueous dispersion (pH = 7.4) (Figure 4.2.4). The composites were redispersed immediately before the measurements to minimize possible zinc peroxide decomposition at chosen pH value.

The comparison of the data obtained for the PVCL/GMA@ZnO_2/*o*-PEA (5/1)_100wt% sample and the PVCL/GMA-MG reference revealed that the incorporation of the ZnO_2/*o*-PEA nanoparticles influenced the thermoresponsive properties of the microgels and seemed to increase the overall microgel stability (Figure 4.2.4a). The hydrodynamic radii of the loaded microgels decreased constantly from 300.6 to 162.8 nm with increasing temperature from 15.0 to 50.0 °C while the radii of the unloaded reference decreased from 318.7 to 144.1 nm with an intermediate radii increase at 29.0 °C (284.8 nm). Further the radii and PDI's of the unloaded microgels should have been smaller compared to the loaded ones, like already observed for the room

temperature measurements. The observed deviating behavior of the unloaded microgels could have been caused through the free GMA functions which induce hydrophobic domains inside the microgel which can influence the microgel stability at changing temperatures. These GMA functions were deactivated through the coupling with the ZnO_2/*o*-PEA nanoparticles which increased the microgel stability leading to a more homogenous temperature responsive behavior.

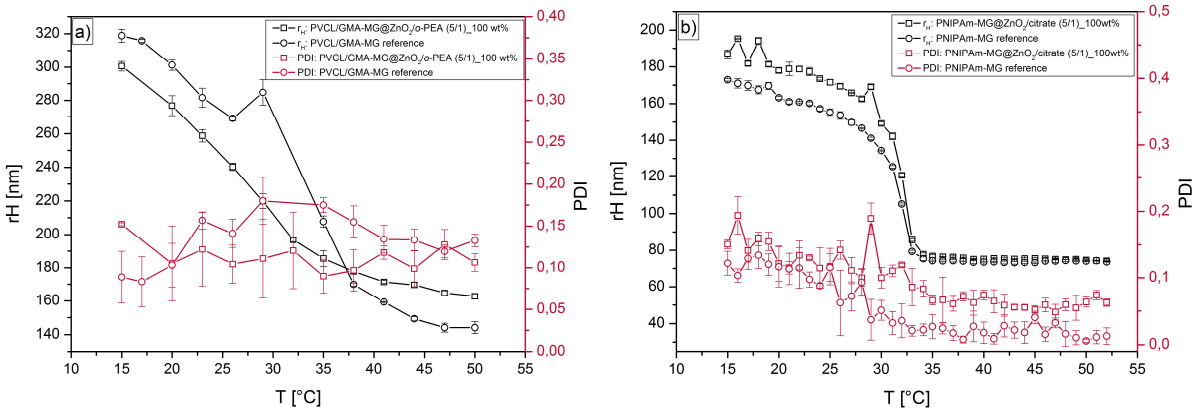

Figure 4.2.4: *Hydrodynamic radii and PDI's determined via temperature dependent dynamic light scattering measurements for the PVCL/GMA@ZnO_2/o-PEA (a) and PNIPAm@ZnO_2/citrate samples (b) in comparison to the corresponding unloaded microgels.*

Contrary the PNIPAm@ZnO_2/citrate (5/1)_100wt% sample showed nearly the same temperature responsive behavior like the corresponding unmodified microgel (Figure 4.2.4b). Identical VPPT's of 31.9 and 32.0 °C could be calculated for both samples and only an initial size difference of 13.8 nm could be measured at 15.0 °C. This size increase was again caused through the nanoparticle incorporation.

These investigations revealed the successful introduction of a proof of principal nanoparticle incorporation procedure. It was possible to incorporate different functionalized zinc peroxide nanoparticles into different types of microgels via specific interactions between corresponding functional groups. Additionally the nanoparticle content inside the microgels could be tuned via initial reactant ratios and the thermoresponsive properties of the microgels could be preserved. However further investigations have to be performed to validate the obtained data and to incorporate other functionalized nanoparticles into other microgel types.

5 Outlook

Zinc peroxide nanoparticles were successfully synthesized and stabilized with different functional molecules. Most of these molecules, beside BMEP and AOT, were already used as linker between the functionalized nanoparticles and different polymers or biological systems. Therefore BMEP could be used to incorporate the corresponding nanoparticles into polymers in prospective experiments. The methacrylate functions present on the nanoparticle surface could participate in radical polymerization processes leading to covalently bound nanoparticles in the resulting polymeric structures. Additionally these nanoparticles could also act as a crosslinking agent due to several methacrylate functions presented on the zinc peroxide surface.

Further other stabilizing molecules could be used to establish new specific interactions between the zinc peroxide nanoparticles and other systems. For example could the UDP-Glc molecules be substituted through other glycol-conjugates like the UDP-disaccharide UDP-LacNAc. This molecule can specifically interact with galectins mostly present on cancer cells which could lead to new oxygen driven anti-cancer treatment methods.

Also the incorporation of the ZnO_2/*o*-PEA and ZnO_2/citrate nanoparticles into PVCL/GMA and PNIPam microgels has to be investigated more in detail. More incorporation variations have to be performed to validate the already obtained data. Additionally the oxygen release properties of these microgel/nanoparticle composites in aqueous media have to be investigated in dependence of composite concentration and/or pH value. Furthermore the loaded microgels could be applied in electro spinning experiments resulting in oxygen releasing microgel-based fibres. This synthesis approach could lead to antibacterial and biocompatible materials which have an extremely high potential for biomedical applications.

Generally the shown antibacterial properties of the zinc peroxide nanoparticles have to be investigated more in detail. Further bacteria types could be tested and the influence of different pH values on the antibacterial properties of the nanoparticles has to be observed.

6 Experimental

6.1 Materials

All following chemicals were used without further purification.

Table 6.1.1: *Used chemicals, the corresponding producers, CAS numbers and purities.*

Chemical	Producer	CAS number	Purity [%]
1,1,1,3,3,3-hexafluoropropane-2-ol (HFIP)	Fluorochem	38701-74-5	---
2-Amino-2-(hydroxymethyl)-1,3-propanediol (TRIS)	Sigma	77-86-1	≥99.9
4-(2-hydroxyethyl)-1-piperazineethanesulfonic acid (HEPES)	Sigma	7365-45-9	≥99.5
Bis[2-(methacryloyloxy)ethyl] phosphate (BMEP)	Aldrich	32435-46-4	---
Calcium chloride	Sigma	10043-52-4	≥96.0
Concanavalin A	Vector Labs	---	99.0
Demineralized water	---	---	---
Dioctyl sulfosuccinate (AOT)	Aldrich	577-11-7	98.0
D-Mannose	Sigma	3458-28-4	≥99.0
Glucose-1-phosphate	P.&L.	59-56-3	---
Hydrogen chloride	Merck	7647-01-0	100.0
Hydrogen peroxide	VWR	7722-84-1	33.0
Methanol	Sigma	67-56-1	≥99.8
o-phosphorylethanolamine (*o*-PEA)	Sigma	1071-23-4	---
Oregon Green 488 NHS-ester	ThermoFischer	198139-51-4	99.0
Polysorbate 20 (Tween 20)	Sigma	9005-64-5	---
r-PET	---	---	---
Sodium chloride	Fluka	7647-14-5	≥99.0
Sodium hydroxide	Merck	1310-73-2	100.0
Trisodiumcitrate dihydrate	Sigma	6132-04-3	≥99.9
Uridine diphosphate glucose	Carbosynth	28053-08-9	98.0
Zinc acetate dihydrate	Sigma	5970-45-6	≥99.0
Zinc peroxide	Aldrich	1314-22-3	50-60

6.2 Analytical Methods

6.2.1 X-Ray Diffraction (XRD)

The crystal structures of the zinc peroxide nanoparticles were characterized via X-Ray-diffraction measurements (XRD) on a PANalytical Empyrean X-Ray-diffractometer (PANalytical B.V., Netherlands), using a $CuK_{\alpha 1}$ radiation (λ = 0.1542 nm). The sample powder was placed on the sample holder as a thin film and the measurement was performed between angles of 0.0 and 120.0°. Temperature dependent XRD measurements were performed in situ in a capillary furnance on a STOE STADI PM diffractometer (STOE & Cie GmbH, Germany) using a $CuK_{\alpha 1}$ radiation (λ = 0.15056 nm).

6.2.2 Thermo Gravimetric Analysis (TGA)

The thermal behaviors of the samples were determined through thermo gravimetric analysis (TGA) on a Thermo-Microscale TG 209C (Netzsch-Gerätebau GmbH, Germany). Simultaneously thermogravimetry and mass spectroscopy (TGA-MS) investigations combined with differential scanning calorimetry (DSC) measurements were performed on a Netsch STA 449CD Skimmer calorimetric setup. Approximately 5.0 mg sample powder was used for each measurement.

6.2.3 Transmission Electron Microscopy (TEM)

The morphology and sizes of ZnO_2 nanoparticles were investigated with transmission electron microscopy (TEM) on a Libra 120 from Zeiss (Carl Zeiss AG, Germany), while HR-TEM measurements were performed by a CM 200 FEG/ Lorentz at 200 kV (FEI, Netherlands) at 200kV acceleration voltage at a nominal point resolution of 0.24 nm and line resolution of 0.20 nm. HRTEM data were analyzed by using the Digital Micrograph software (Gatan company, USA). One nanoparticle dispersion droplet (c = 3.0 g/L) was placed on 400 mesh carbon coated copper grid (EMS, USA) and dried over night for each measurement.

6.2.4 pH Dependent Zeta Potential Measurements

Zeta potential measurements were done with a Malvern Zetasizer Nano ZS (Malvern Instruments Ltd, England) combined with an autotitrator MPT-2. The pH value of the measurement dispersion (c = 1 g/L) was automatically adjusted with hydrochloric acid and sodium hydroxide solutions (c = 1 mol/L). The measurements were performed in a pH range from 2.0 to 10.0.

6.2.5 Raman Spectroscopy

Raman spectroscopy measurements were performed on a Bruker RFS 100/S (Bruker Corporation, USA). 1000 scans were performed for each sample with a Nd:YAG laser with a wavelength of λ = 1064.0 nm and a spectral resolution of 4.0 cm^{-1}. The samples were measured in dry state by Dr. Walter Tillmann.

6.2.6 Fourier Transformed Infrared Spectroscopy (FTIR)

FTIR measurements were performed on a Nicolet Nexus 470 (Thermo Fisher Scientific, USA). The sample powder was analyzed as a KBr pellet by Dr. Walter Tillmann.

6.2.7 ^{31}P High Resolution Magic-Angle Sample Spinning Spectroscopy (^{31}P-HRMAS)

High-power proton decoupled ^{31}P high-resolution magic-angle sample spinning NMR spectra were measured at 23.0°C temperatures with a Bruker Avance III HD 700 (Bruker Corporation, USA). The spinial64 pulse sequence was applied to proton frequency for ^{31}P-^{1}H heteronuclear decoupling and NMR spectrometer frequency for ^{31}P was 283.367 MHz. All the ^{31}P-HRMAS spectra were externally referenced to ammonium phosphate monobasic that has the ^{31}P resonance at +1 ppm relative to phosphorous acid 85% in H_2O used as zero ppm reference. The rotor frequency was 5 kHz, the recycle delay was 7 s, the radio-frequency pulse length was 4 µs (75 W), while the dwell time was 4 µs, and the number of scans was 2016. The time domain data were 4k and the zero filling was done with 16k. The relative spectral integral

intensities of the peaks were measured using TopSpin 3.2 Bruker software. The measurements were performed by Prof. Dr. Dan Demco.

6.2.8 Inductively Coupled Plasma Atom Emission Spectroscopy (ICP-OES)

Inductively coupled plasma atom emission spectroscopy (ICP-OES) measurements were done on a Spectroflame D (SPECTRO Analytical Instruments GmbH, Germany). 1.0 mg of each sample were dispersed in 2.0 mL Milli-Q water followed by addition of 0.5 mL hydrochloric acid (c = 1.0 mol/L). The obtained solution was stirred for five days and afterwards measured by Heike Bergstein.

6.2.9 pH Dependent Oxygen Release Measurements

The pH dependent oxygen release of the different nanoparticle samples was determined via long term measurements (6 to 7 days) under argon atmosphere with an optical oxygen sensor FDO®925 from WTW (Xylem Analytics Germany Sales GmbH & Co. KG, Germany). This sensor can quantify the amount of dissolved oxygen in aqueous media via time dependent fluorescence measurements. The sealed sensor head consists of a membrane containing a fluorescent dye and a pulsed laser which generates low energy radiance (green light). The laser irradiates the fluorescent dye inside the membrane which causes the emission of longer wavelength light during its relaxation which then is measured by the sensor. When oxygen is present in the measurement solution it diffuses through the membrane and shortens the emission duration of the fluorescent dye depending on the oxygen concentration which leads to the quantification of the oxygen. A specific amount of each sample (10.0 or 5.0 mg) was dispersed in 10.0 mL Milli-Q water with the corresponding pH value (6.5, 7.5 or 8.5). This dispersion was degassed for 45 minutes via nitrogen flow under continuous stirring. Simultaneously a sealed Schlenk tube containing the oxygen sensor was degassed and flooded with argon. The measurement dispersion was transferred into the Schlenk tube afterwards and the measurement was started with a five minute measurement interval.

6.2.10 Fluorescence Measurements

The interaction between the biofunctionalized nanoparticles and the lectin Concanavalin A (ConA) was investigated by fluorescence measurements which were carried out on a Synergy 2 from BioTek (BioTek Instruments Inc., USA). The used ConA was labeled with Oregon Green 488 NHS-Ester by reacting 10 mg ConA with 3 eq. dye in phosphate-bicarbonate buffer at pH 8.3. The reaction was left in the dark overnight. Removal of residual unreacted dye was accomplished by SEC using Sephadex G-25 with PBS as mobile phase. ConA-Oregon Green was stored at 4°C. The fluorescence measurements were carried out with excitation and emission wavelength of 485 and 528 nm, which were used for the quantifications of the immobilized ConA. The immobilization of the ConA on the nanoparticle surface was done by dispersing 0.5 mg of the corresponding sample in 500 µL buffer containing 10.0 mM HEPES, 150.0 mM NaCl and 0.1 mM $CaCl_2$ followed by adding 20 µL (c = 20 µg/mL) of the labeled ConA. This mixture was incubated for 30 minutes and subsequently washed four times with a buffer consisting of 10.0 mM HEPES, 150.0 mM NaCl and 0.1 mM $CaCl_2$, 0.05% Tween-20 to eliminate excessive ConA. Different amounts of mannose (c = 2.0 g/L; 20, 40, 60, 80, 100, 120, 140, 160, 180 and 200 µL) were added to the used buffer for the inhibition measurements, while the following preparation steps were equally to the other fluorescent measurements.

6.2.11 Colorimetry

The color values of PET were measured fivefold for each sample with the aid of the Datacolor Spectraflash SF600 plus CT UV colorimeter (Datacolor, Germany) using the D65 illuminant and the 10° observer. A special specimen container (Datacolor) was used. The color values were calculated with the Datacolor formula based on the CIE-L*a*b* system. In this system, L* represents the lightness (L*=0 indicates black, L*=100 white). The a*-value corresponds to the green-red axis, where negative a*-values document green and positive a*-values red hues. The b*-value represents the blue-yellow axis, where negative b*-values document blue and positive b*-values yellow hues. Furthermore, the yellowness of the PET samples was evaluated according to the yellowness formula of DIN 6167 (G-DIN 6167). Increasing yellowness is indicated by increasing G-DIN 6167 values.

6.2.12 Inherent Viscosity Measurements

The inherent viscosity ($\eta_{inh.}$) of the PET polymers was measured with the help of an Ubbelohde viscosimeter (type 0a) (Schott AG, Germany). About 0.3300 g PET was weighed in a 25 mL graduated flask and dissolved in 1,1,1,3,3,3-hexafluoropropane-2-ol (HFIP). The viscosity of this solution was measured at 25 °C. The inherent viscosity was calculated according to equation [6].

$$\eta_{inh} = \frac{\ln(\eta_{rel})}{\beta} = \frac{\ln(\frac{\eta}{\eta_0})}{\beta} = \frac{\ln(\frac{t}{t_0})}{\beta} \quad [6]$$

with η_{inh} = inherent viscosity, η_{rel} = relative viscosity, β = mass concentration, η = viscosity of the PET solution, η_0 = viscosity of the solvent, t = flow time of the PET solution and t_0 = flow time of the solvent.

6.2.13 Electrophoresis

The one channel electrophoresis measurements were performed by Thomas Fischöder on a G7100A from Agilent (Agilent Technologies, USA). A fused silica capillary with a diameter of 50.0 µm and a length of 64.0 cm was used for the measurements. The nanoparticle dispersions were diluted with a parent solution consisting of 2.0 mM 4-amino-benzoeic acid (PABA), 2.0 mM 4-amino-phtalic acid (PAPA) and 14.0 mM SDS. The used PABA and PAPA acted as internal standards and were used for the area normalization and the identification/quantification of UDP-Glc and its by-products. Furthermore a running buffer consisting of 50.0 mM ammonium acetate and 1.0 mM ethylene diaminetetraacetic acid (EDTA) with a pH value of 9.2 was used. The UPD-Glc concentrations were determined through equation [7].

$$c_{UDP-G} = \left(\frac{\frac{area_{UDP-Glc}}{area_{PABA}}}{0.54} \right) \cdot 2 \quad [7]$$

6.2.14 Antibacterial Measurements

The antibacterial properties of zinc peroxide nanoparticles were determined through the calculation of the minimum inhibitory concentration (MIC). This value was

determined through the exposure of different bacteria types to different zinc peroxide concentrations. The measurements were performed by Prof. Georg Conrads employees.

Zinc peroxide nanoparticles with 50.89 wt% ZnO_2 plus 49.10 wt% Glc-1P (ZnO_2/Glc-1P (2/1)_30c(12min)) and 30.53 wt% ZnO_2 plus 69.49 wt% Glc-1P (ZnO_2/Glc-1P (1/1)_30c(12min)) were used for the initial testing. A stock solution of 2000 µg/ml of both nanoparticles was prepared using appropriate culture media: Mueller-Hinton Broth (MHB) in the case of *E. faecalis*, Brain-Heart-Infusion Broth (BHI) in the case of the three more fastidious organisms. In the case of *P. gingivalis* and *P. intermedia* BHI was further supplemented with hemin and vitamin K1 (both Becton Dickinson, and both 2 wt% end concentration) as well as with isovitalex (Becton Dickinson, 2 v% end concen). From these stock solutions the dilutions 1:2, 1:10, 1:20, 1:40, 1: 80, and 1:160 were prepared in a 96-well-microtiterplate resulting in corresponding final concentrations of the nanoparticles of 1000µg/ml, 200µg/ml, 100µg/ml, 50µg/ml, 25µg/ml, 12,5 µg/ml in a total volume of 200 µl. The dilutions were prepared with culture media (see above) and pre-culture (see below). For the pre-cultures, the bacteria were grown aerobically (E. faecalis) in 5-10% CO_2 (*A. actinomycetemcomitans*) or anaerobically (*P. gingivalis* and *P. intermedia*) 24-48 h at 37°C. With each pre-culture between 10,000-100,000 cells were added to the microtiter wells. By this method the substance-depending minimal inhibitory concentration (MIC) was determined. The minimum inhibitory concentration (MIC) is the lowest concentration of an antibacterial agent required to inhibit further growth of a particular bacterium. From every well of the microtiter plate an aliquot of 3 µl was plated on Trypticase-Soy-Agar with 5 % sheep blood to determine the minimal bactericidal concentration (MBC). In contrast to the MIC, the minimum bactericidal concentration (MBC) is the lowest concentration of an antibacterial agent required to kill a particular bacterium.

6.3 Used Devices

6.3.1 Microfluidizer MRT-CR 5

Most of the nanoparticle syntheses were carried out in the Microfluidizer MRT-CR 5 (Microfluidics, USA). The device consists of an intensifier pump combined with a y-

formed reaction chamber with channel diameter of 75.0 µm. Additionally a z-formed APM module is attached behind the reaction chamber to provide a supporting back pressure to the reaction chamber. Both the reaction chamber and the APM module are coated with a ceramic layer to ensure a sufficient durability. The device can be used as a continuous batch reactor and the flow rate is adjustable through different process pressures (100.0 to 1400.0 bar).

6.3.2 Centrifuge

The purification of the synthesized nanoparticles was done by washing and centrifugation. To separate the nanoparticles from the supernatant a centrifuge 5810 (Eppendorf AG, Germany) was used.

6.3.3 Ultrasonic Bath

An ultrasonic bath Sonorex Digitec DT 100 H (Bandelin electronic GmbH & Co. KG, Germany) was used to solve educts and redisperse certain nanoparticles.

6.3.4 Lyophilization

The lyophilization device LyoQuest (Telstar, Spain) was used to separate the synthesized nanoparticles from the reaction media. The reaction solutions were freeze dried immediately after the synthesis and the frozen reaction media was sublimated at -70.0 °C and 0.01 mbar.

6.3.5 Ultra-Turrax

An ultra-turrax Omni TH-02 (Omni International, USA) was used to redisperse the nanoparticle samples and to prepare measurement dispersion. The maximum rotation speed of 35000 rpm was used in all cases.

6.3.6 Extruder

A Micro 15cc Twin Screw-Extruder (DSM, Netherlands) was used for the incorporation of the zinc peroxide nanoparticles into r-PET.

6.3.7 Cryomill

The grinding of the bleached PET or the macroscopic zinc peroxide was performed in a cryomill 6800 Freezer/Mill (SPEX CertiPrep, Great Britain). The mill was cooled with liquid nitrogen to reduce the abrasion heat during the grinding process.

6.4 Synthesis of Zinc Peroxide Nanoparticles

6.4.1 Synthesis of ZnO_2 Nanoparticles Stabilized with BMEP

Specific amounts of zinc acetate dihydrate and the stabilizer BMEP (Table 6.4.1) were dissolved in 198.5 mL demineralized water. This solution was added into the high pressure impinging jet reactor. Afterwards the aqueous hydrogen peroxide solution (1.5 mL, $1.3 \cdot 10^{-2}$ mol) was added and the reaction was started. Different cycle numbers (reaction times) were chosen depending on the synthesis approach (one cycle = 25.0 seconds). The obtained reaction dispersion was immediately freeze dried and the reaction medium was separated via lyophilization. The resulting solid was washed three times with 30.0 mL methanol and centrifuged at 12000 rpm for 30 minutes. The supernatant was separated through decantation. Afterwards the clean product was dried at room temperature.

Table 6.4.1: *Cycle numbers, zinc acetate and BMEP amounts for the different ZnO_2/BMEP synthesis approaches.*

Sample	Cycle number	n $Zn(ac)_2$ [mol]	n BMEP [mol]
ZnO_2/BMEP (1/1)_5c_2min	5	$5.1 \cdot 10^{-4}$	$5.1 \cdot 10^{-4}$
ZnO_2/BMEP (1/1)_10c_4.5min	10	$5.1 \cdot 10^{-4}$	$5.1 \cdot 10^{-4}$
ZnO_2/BMEP (1/1)_20c_9min	20	$5.1 \cdot 10^{-4}$	$5.1 \cdot 10^{-4}$
ZnO_2/BMEP (1/1)_30c_13min	30	$5.1 \cdot 10^{-4}$	$5.1 \cdot 10^{-4}$
ZnO_2/BMEP (5/1)_20c_9min	20	$2.5 \cdot 10^{-3}$	$5.1 \cdot 10^{-4}$
ZnO_2/BMEP (10/1)_20c_9min	20	$5.1 \cdot 10^{-3}$	$5.1 \cdot 10^{-4}$

6.4.2 Synthesis of ZnO_2 Nanoparticles Stabilized with *o*-PEA

Specific amounts of zinc acetate dihydrate and *o*-PEA (Table 6.4.2) were dissolved in 192.5 mL demineralized water. 1.87 mL (0.016 mol) aqueous hydrogen peroxide solution was added to the reaction solution followed by the reaction start. The obtained product was washed three times with 30.0 mL demineralized water. All other reaction steps were similar to section 6.4.1.

Table 6.4.2: *Cycle numbers, zinc acetate and o-PEA amounts for the different ZnO_2/o-PEA synthesis approaches.*

Sample	Cycle number	n $Zn(ac)_2$ [mol]	n *o*-PEA [mol]
ZnO_2/*o*-PEA (1/1)_5c(2 min)	5	$5.7 \cdot 10^{-3}$	$5.7 \cdot 10^{-3}$
ZnO_2/*o*-PEA (1/1)_10c(4 min)	10	$5.7 \cdot 10^{-3}$	$5.7 \cdot 10^{-3}$
ZnO_2/*o*-PEA (1/1)_20c(8 min)	20	$5.7 \cdot 10^{-3}$	$5.7 \cdot 10^{-3}$
ZnO_2/*o*-PEA (5/1)_20c(8 min)	20	$5.7 \cdot 10^{-3}$	$1.1 \cdot 10^{-3}$
ZnO_2/*o*-PEA (10/1)_20c(8 min)	20	$5.7 \cdot 10^{-3}$	$5.6 \cdot 10^{-4}$

6.4.3 Synthesis of ZnO_2 Nanoparticles Stabilized with Citrate

The synthesis of zinc peroxide nanoparticles stabilized with citrate was performed similar to section 6.4.2 with two exceptions: 7.5 mL (0.065 mol) aqueous hydrogen peroxide was used and the cleaning process was performed three times with 20.0 mL demineralized water.

Table 6.4.3: *Cycle numbers, zinc acetate and citrate amounts for the different ZnO_2/citrate synthesis approaches.*

Sample	Cycle number	n $Zn(ac)_2$ [mol]	n citrate [mol]
ZnO_2/citrate (1/1)_20c(8min)	20	$7.5 \cdot 10^{-3}$	$7.5 \cdot 10^{-3}$
ZnO_2/citrate (1/1)_30c(12min)	30	$7.5 \cdot 10^{-3}$	$7.5 \cdot 10^{-3}$
ZnO_2/citrate (1/1)_40c(16min)	40	$7.5 \cdot 10^{-3}$	$7.5 \cdot 10^{-3}$
ZnO_2/citrate (5/1)_20c(8min)	20	$7.5 \cdot 10^{-3}$	$1.6 \cdot 10^{-3}$
ZnO_2/citrate (10/1)_20c(8min)	20	$7.5 \cdot 10^{-3}$	$0.8 \cdot 10^{-3}$

6.4.4 Synthesis of ZnO_2 Nanoparticles Stabilized with Glc-1P

The synthesis of the zinc peroxide nanoparticles stabilized with glucose-1-phosphate was carried out similar to section 6.4.3.

Table 6.4.4: *Cycle numbers, zinc acetate and glucose-1-phosphate amounts for the different ZnO_2/ glucose-1-phosphate synthesis approaches.*

Sample	Cycle number	n $Zn(ac)_2$ [mol]	n glucose-1-phosphate [mol]
ZnO_2/Glc-1P (1/1)_10c(4min)	10	$7.6 \cdot 10^{-3}$	$7.6 \cdot 10^{-3}$
ZnO_2/Glc-1P (1/1)_20c(8min)	20	$7.6 \cdot 10^{-3}$	$7.6 \cdot 10^{-3}$
ZnO_2/Glc-1P (1/1)_30c(12min)	30	$7.6 \cdot 10^{-3}$	$7.6 \cdot 10^{-3}$
ZnO_2/Glc-1P (1/1)_40c(16min)	40	$7.6 \cdot 10^{-3}$	$7.6 \cdot 10^{-3}$
ZnO_2/Glc-1P (2/1)_30c(12min)	30	$7.6 \cdot 10^{-3}$	$3.8 \cdot 10^{-3}$
ZnO_2/Glc-1P (4/1)_30c(12min)	30	$7.6 \cdot 10^{-3}$	$1.8 \cdot 10^{-3}$
ZnO_2/Glc-1P (6/1)_30c(12min)	30	$7.6 \cdot 10^{-3}$	$1.3 \cdot 10^{-3}$
ZnO_2/Glc-1P (8/1)_30c(12min)	30	$7.6 \cdot 10^{-3}$	$1.0 \cdot 10^{-3}$
ZnO_2/Glc-1P (10/1)_30c(12min)	30	$7.6 \cdot 10^{-3}$	$0.8 \cdot 10^{-3}$

6.4.5 Synthesis of ZnO_2 Nanoparticles Stabilized with UDP-Glc

The synthesis of zinc peroxide nanoparticles stabilized with UDP-glucose was carried out in a flask. Specific amounts of zinc acetate (Table 6.4.5) were dissolved in 36.0 mL demineralized water and placed in a three-neck flask. This solution was heated to 80.0 °C under reflux and continuous stirring (300 rpm). Simultaneously different amounts of UDP-Glc were dissolved in 2.5 mL demineralized water and where placed in a syringe which was attached to a syringe pump (flow rate = 0.25 mL/min). The aqueous hydrogen peroxide solution (1.5 mL, 0.013 mol) was also placed in syringe, which was attached to a second syringe pump (flow rate = 0.09 mL/min). The synthesis was initiated through the injection of the hydrogen peroxide solution to the zinc acetate solution and lasted for 45 minutes. Different synthesis approaches were performed in which the UDP-Glc solution was simultaneously injected compared to the hydrogen peroxide solution or with different time delays (3, 4 and 5 minutes). The synthesis dispersion was immediately freeze dried after the synthesis and the water was separated via lyophilization. The obtained product was washed three times with 20.0 mL demineralized water and centrifuged at 12000 rpm for 30

minutes. The supernatant was decanted and the clean product was dried at room temperature.

Table 6.4.5: *Injection times, zinc acetate and UDP-glucose amounts for the different ZnO_2/ UDP-Glc synthesis approaches.*

Sample	Injection start UDP-Glc solution [min]	n $Zn(ac)_2$ [mol]	n UDP-Glc [mol]
ZnO_2/UDP-Glc (8/1)_direct	direct	$7.3 \cdot 10^{-4}$	$9.0 \cdot 10^{-5}$
ZnO_2/UDP-Glc (8/1)_3min	3	$7.3 \cdot 10^{-4}$	$9.0 \cdot 10^{-5}$
ZnO_2/UDP-Glc (8/1)_4min	4	$7.3 \cdot 10^{-4}$	$9.0 \cdot 10^{-5}$
ZnO_2/UDP-Glc (8/1)_5min	5	$7.3 \cdot 10^{-4}$	$9.0 \cdot 10^{-5}$
ZnO_2/UDP-Glc (1/1)_4min	4	$7.3 \cdot 10^{-4}$	$7.3 \cdot 10^{-4}$
ZnO_2/UDP-Glc (2/1)_4min	4	$7.3 \cdot 10^{-4}$	$3.6 \cdot 10^{-4}$
ZnO_2/UDP-Glc (4/1)_4min	4	$7.3 \cdot 10^{-4}$	$1.8 \cdot 10^{-4}$
ZnO_2/UDP-Glc (6/1)_4min	4	$7.3 \cdot 10^{-4}$	$1.2 \cdot 10^{-4}$
ZnO_2/UDP-Glc (10/1)_4min)	4	$7.3 \cdot 10^{-4}$	$7.2 \cdot 10^{-5}$

6.4.6 Synthesis of ZnO_2 Nanoparticles Stabilized with AOT

The synthesis of zinc peroxide nanoparticles stabilized with AOT was carried out in flask too. Different amounts of zinc acetate and AOT (Table 6.4.6) were dissolved in 150.0 mL methanol and placed in a two-neck flask. The reaction solution was heated to 100.0 °C under reflux and continuous stirring (300 rpm). Aqueous hydrogen peroxide solution (0.33 mL, $2.83 \cdot 10^{-3}$ mol) was added via a syringe pump (flow rate = 7.3 µL/min) to the reaction solution. The reaction was stopped after one hour and the methanol was separated via rotary evaporation at 25 °C. Afterwards the product was lyophilized to obtain a complete dry powder. The product was washed three times with 20.0 mL methanol and centrifuged at 12000 rpm for 30 minutes. The supernatant was decanted and the product was dried at room temperature.

Table 6.4.6: *Zinc acetate and AOTe amounts for the different ZnO_2/ AOT synthesis approaches.*

Sample	n $Zn(ac)_2$ [mol]	n AOT [mol]
ZnO_2/AOT (5/1)	$1.4 \cdot 10^{-3}$	$2.9 \cdot 10^{-4}$
ZnO_2/AOT (10/1))	$1.4 \cdot 10^{-3}$	$1.4 \cdot 10^{-4}$
ZnO_2/AOT (20/1)	$1.4 \cdot 10^{-3}$	$7.3 \cdot 10^{-5}$
ZnO_2/AOT (30/1)	$1.4 \cdot 10^{-3}$	$4.9 \cdot 10^{-5}$

6.5 Incorporation of ZnO_2 Nanoparticles into r-PET

6.5.1 Extrusion of r-PET with ZnO_2 Nanoparticles

The used recycled PET (r-PET) was obtained from normal PET bottles. The bottles were washed with water and the labels/glues were removed with acetone. Afterwards the bottles were cut into pieces and mixed with a laboratory mixer (Snijders Scientific BV, Netherlands). Several mixing steps with two minutes mixing at highest frequency and in between cooling for one minute in an ice bath were needed for optimum comminution. The so obtained r-PET could be used for the bleaching experiments with macroscopic zinc peroxide and zinc peroxide nanoparticles.

The PET was dried at 130.0°C over night for at least ten hours before use. The zinc peroxide treatment was performed in PET melt under nitrogen atmosphere. For this, the Micro 15cc Twin Screw-Extruder (DSM, Netherlands) was used. About 13.0 g r-PET were molten in the extruder at 290.0 °C and mixed with different amounts of zinc peroxide (0.0, 0.1, 0.2, 0.3, 0.5 and 1.0 wt%) for two minutes with 100 rpm screw rotation speed. The DSM Xplore Data Acquisition and Control v1.11 software was used to measure the screw force. After the extrusion, the polymers were grounded in the cryomill (6800 Freezer/Mill, SPEX CertiPrep, Great Britain) to achieve good homogeneity. Three grinding cycles (5 minutes each) were performed with an impact frequency of 10 s^{-1} and the samples were cooled with liquid nitrogen for 5 min in between the grinding cycles.

6.6 Incorporation of ZnO_2 Nanoparticles into Microgels

The used PVCL/GMA (AT-51-0) and PNIPAm (MK 47) microgels were provided by Alexander Töpel and Michael Kather. 3.0 mL of a 1.0 g/L microgel dispersion were mixed with different amounts of ZnO_2/o-PEA (5/1) or ZnO_2/citrate (5/1) nanoparticles (0.3 mg (10 wt%), 1.5 mg (50 wt%) and 3.0 mg (100 wt%). The dispersions were stirred for 24h at room temperature and afterwards dialyzed for 48h. TRIS buffer (pH=10.2) was used for all microgel experiments and dialysis.

7 Appendix

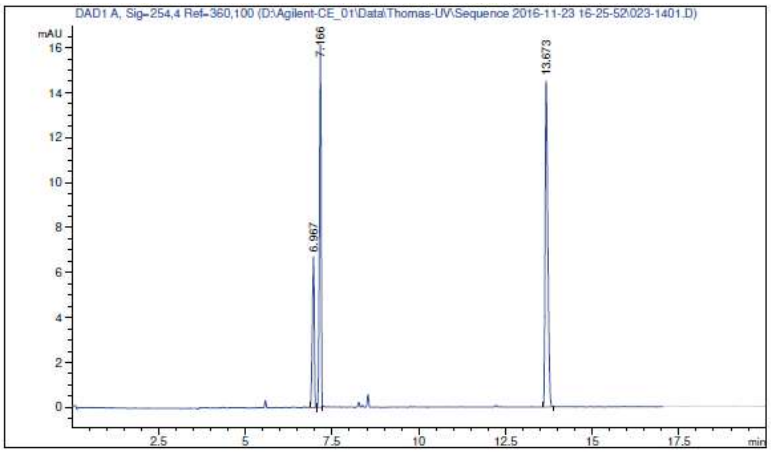


```
================================================================
                    Area Percent Report
================================================================

Sorted By             :      Signal
Area Calculation Mode :      Measured Area
Multiplier            :      1.0000
Dilution              :      1.0000
Do not use Multiplier & Dilution Factor with ISTDs

Signal 1: DAD1 A, Sig=254,4 Ref=360,100

Peak MigTime Type  Width     Area      Height     Area
  #   [min]        [min]   [mAU*s]     [mAU]       %
----|-------|----|-------|----------|----------|--------|
   1   6.967 BV    0.0598   26.45797    6.74581  16.5273
   2   7.166 VV    0.0540   55.68727   16.23889  34.7857
   3  13.673 BB    0.0825   77.94130   14.54230  48.6870
```

Figure 7.1: *Electrophoresis reference measurement for UDP-Glc processed at 80.0 °C for 45 minutes (nanoparticle synthesis conditions). First peak corresponds to UDP-Glc, second peak corresponds to internal PABA standard and third peak corresponds to internal PAPA standard.*

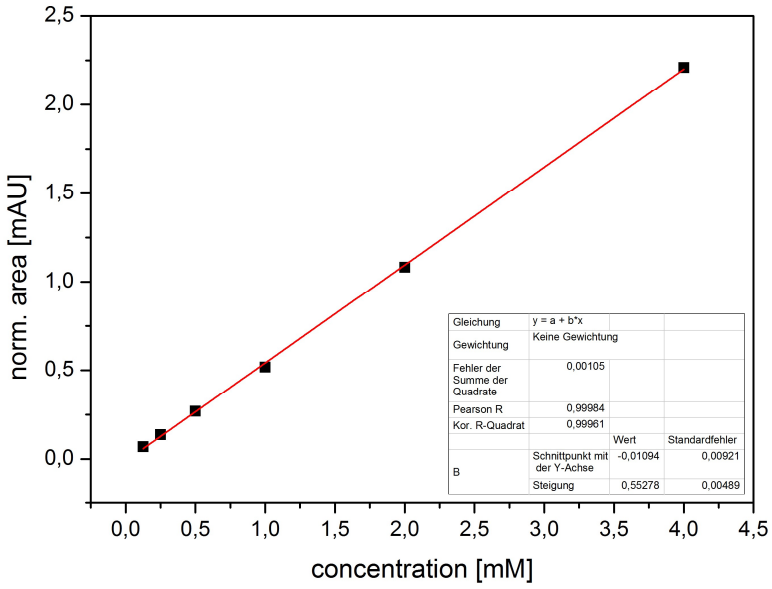

Figure 7.2: *Electrophoresis calibration curve for the quantification of the UDP-Glc concentrations.*

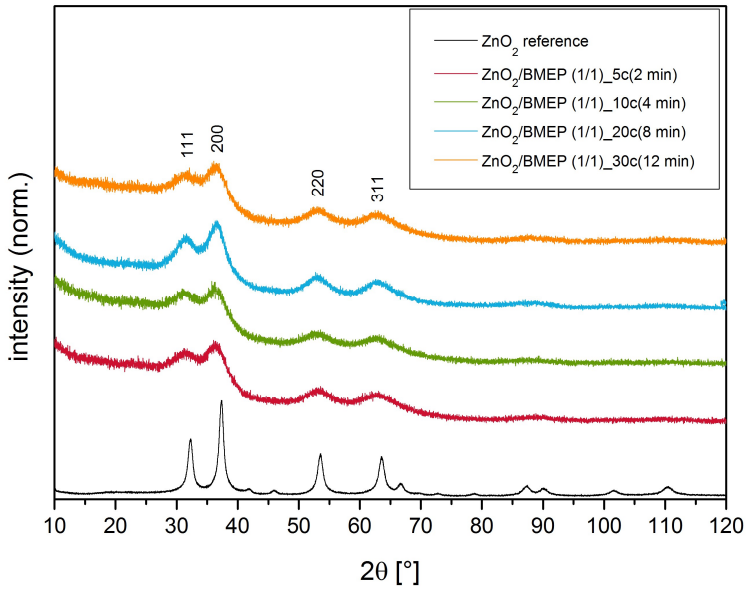

Figure 7.3: *XRD diffractograms of the BMEP stabilized zinc peroxide nanoparticles synthesized at different cycle numbers (reaction times).*

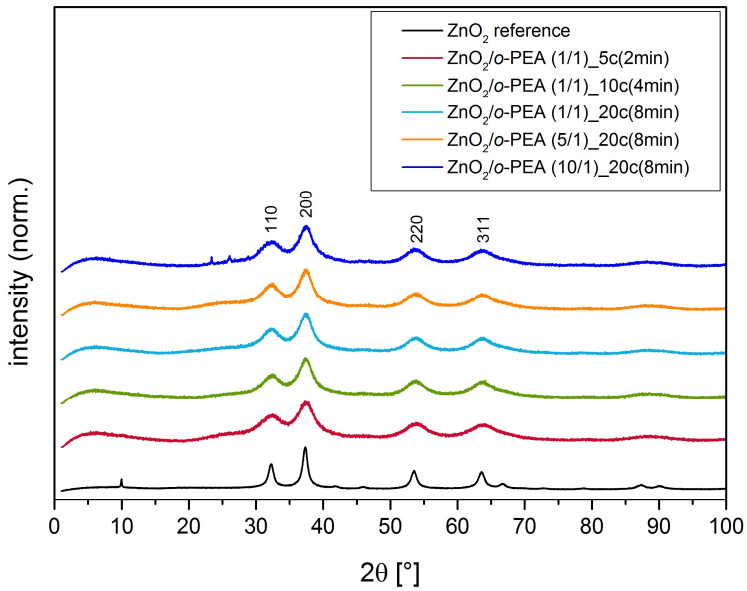

Figure 7.4: *XRD diffractograms of the o-PEA stabilized zinc peroxide nanoparticles synthesized at different cycle numbers (reaction times) and zinc acetate:o-PEA ratios.*

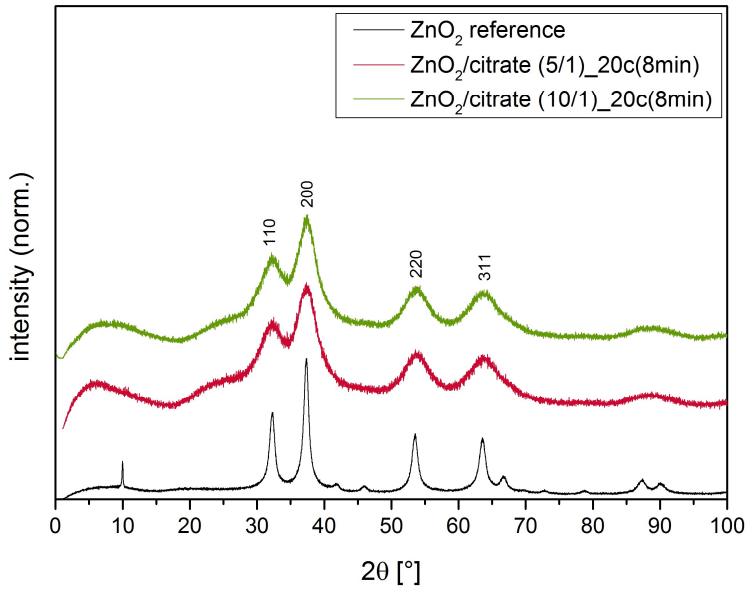

Figure 7.5: *XRD diffractograms of the citrate stabilized zinc peroxide nanoparticles synthesized at different zinc acetate:citrate ratios.*

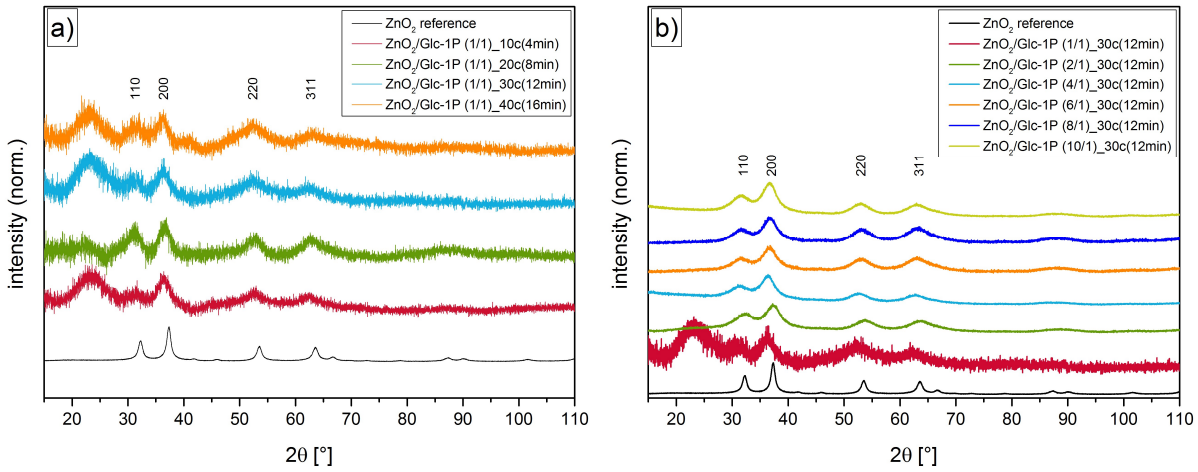

Figure 7.6: *XRD diffractograms of the Glc-1P stabilized zinc peroxide nanoparticles synthesized at different cycle numbers (reaction times) (a) and zinc acetate:Glc-1P ratios (b).*

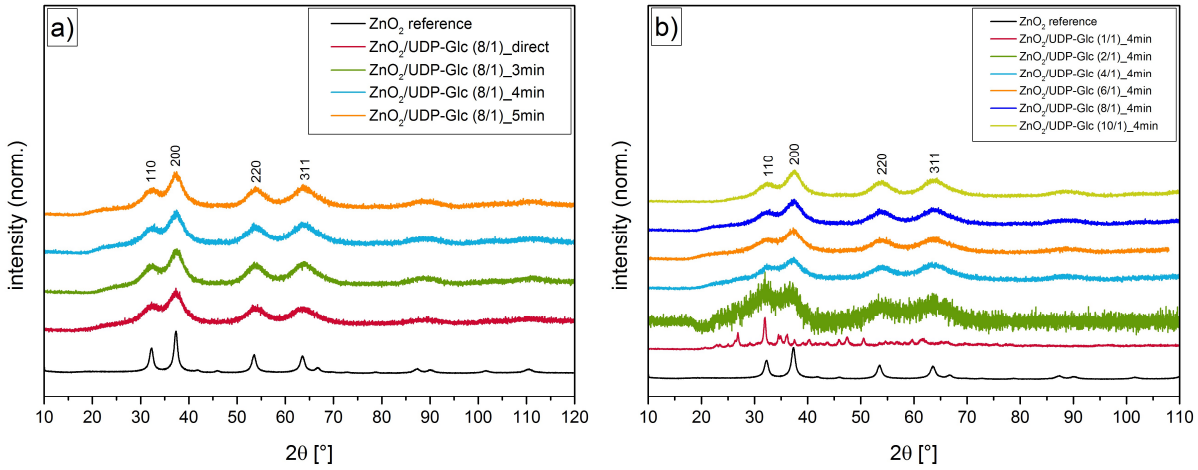

Figure 7.7: *XRD diffractograms of the UDP-Glc stabilized zinc peroxide nanoparticles synthesized at different stabilizer addition times (a) and zinc acetate:UDP-Glc ratios (b).*

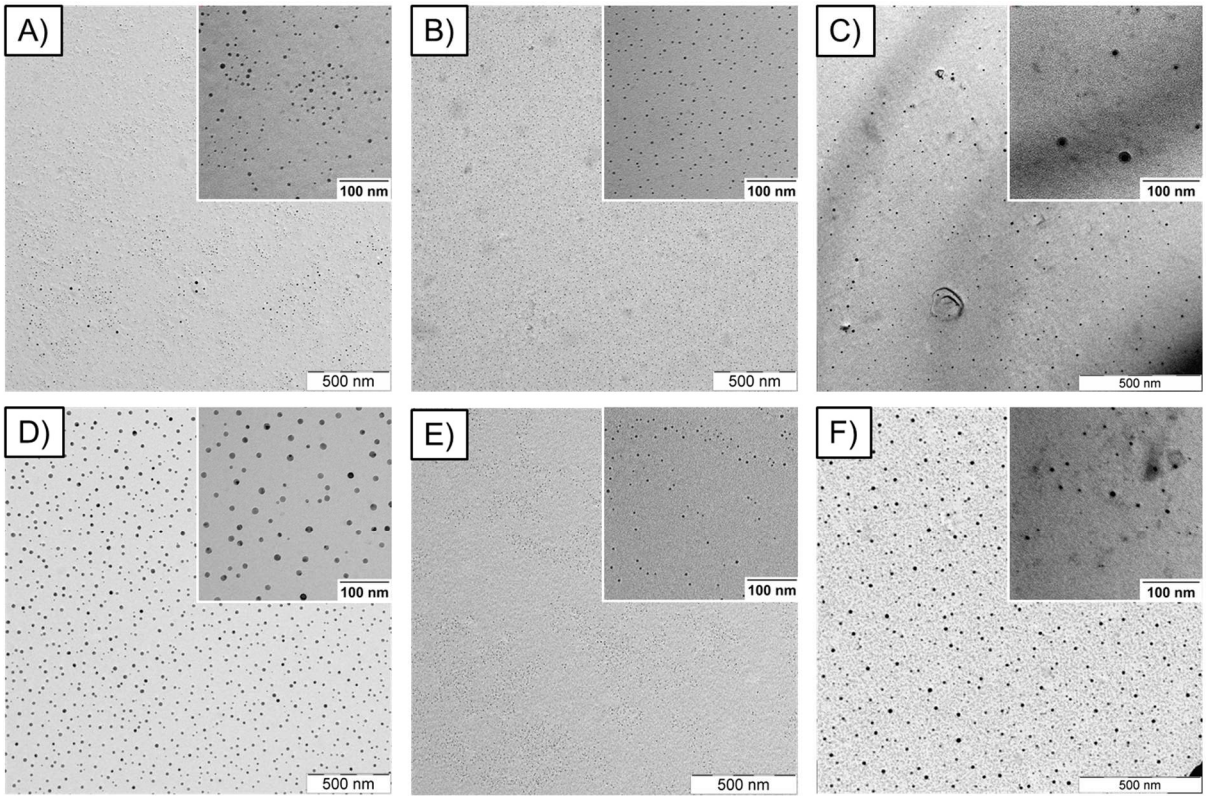

Figure 7.8: *TEM images of the different ZnO_2/BMEP samples; a) ZnO_2/BMEP (1/1)_5c(2min), b) ZnO_2/BMEP (1/1)_10c(4min), c) ZnO_2/BMEP (1/1)_20c(8min), d) ZnO_2/BMEP (1/1)_30c(12min), e) ZnO_2/BMEP (5/1)_20c(8min), f) ZnO_2/BMEP (10/1)_20c(8min).*

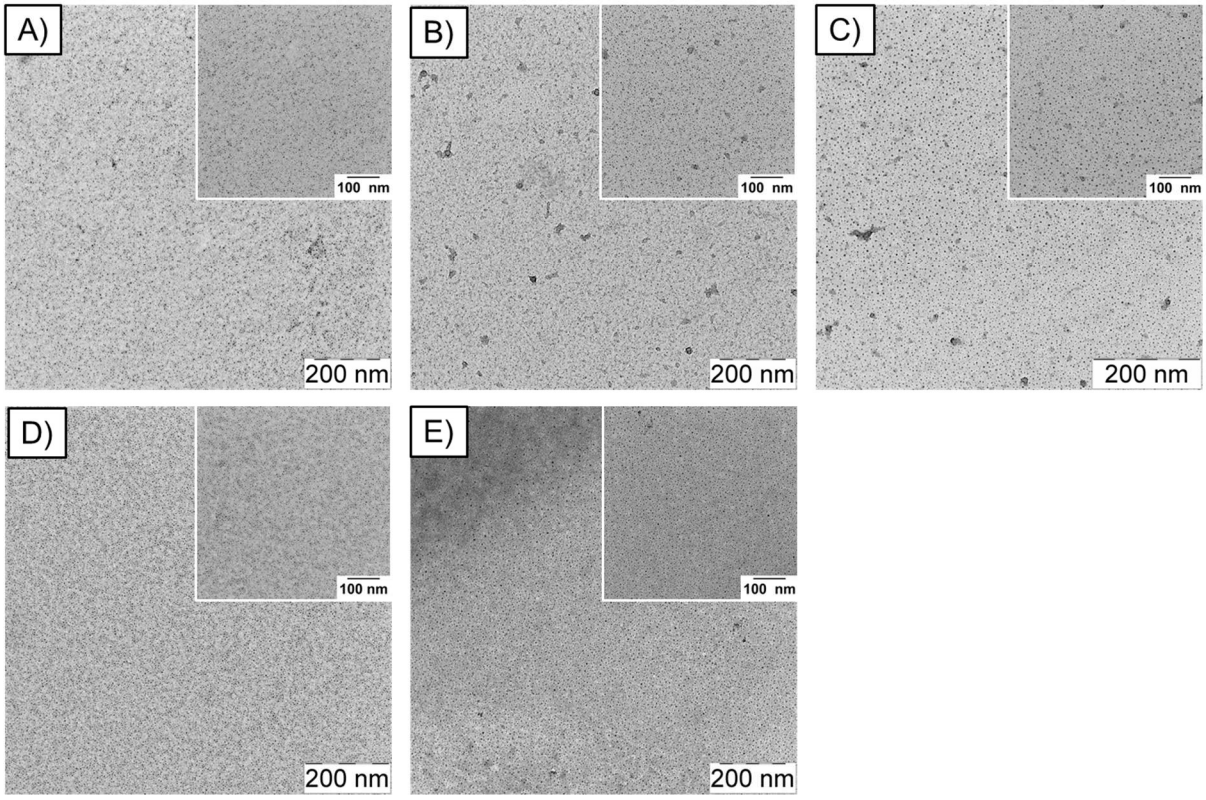

Figure 7.9: *TEM images of the different ZnO_2/o-PEA samples: A) ZnO_2/o-PEA (1/1)_5c(2 min), B) ZnO_2/o-PEA (1/1)_10c(4 min), C) ZnO_2/o-PEA (1/1)_20c(8 min), D) ZnO_2/o-PEA (5/1)_20c(8 min), E) ZnO_2/o-PEA (10/1)_20c(8 min).*

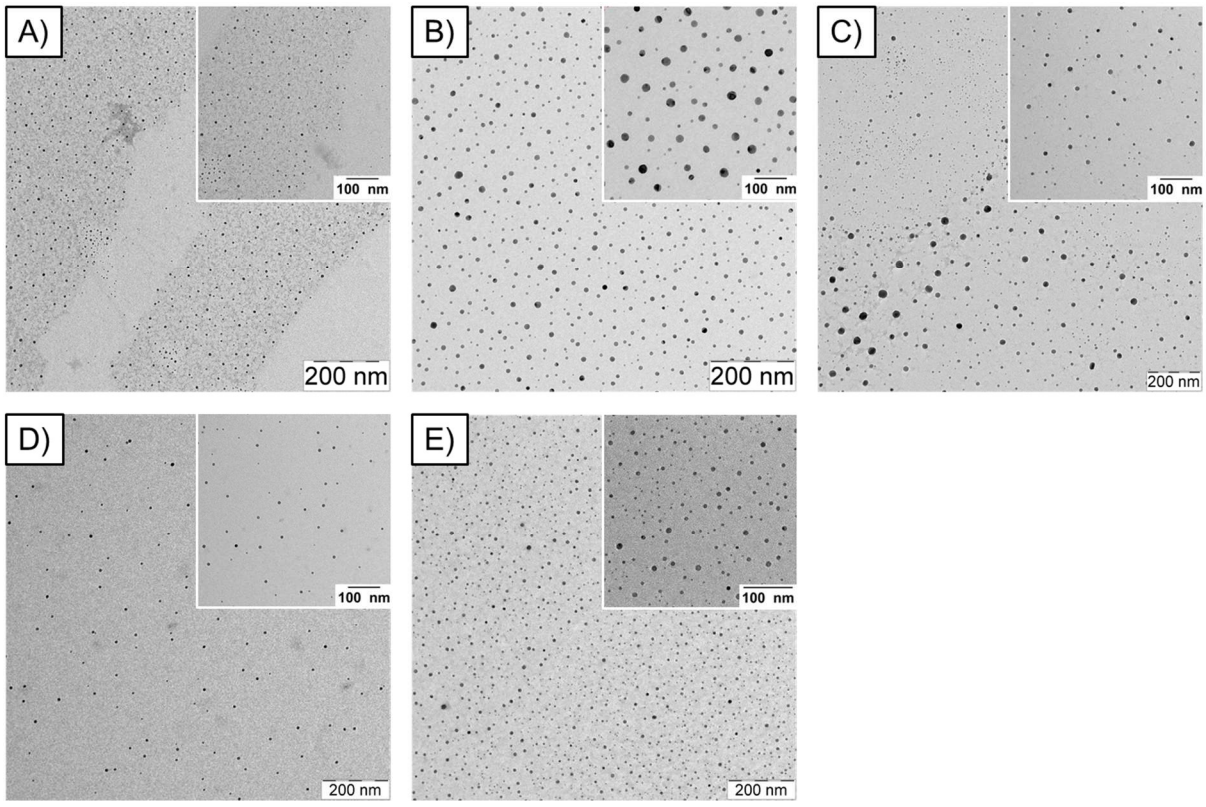

Figure 7.10: *TEM images of the different zinc peroxide nanoparticle samples stabilized with citrate: ZnO_2/citrate (1/1)_20c(8min) (A), ZnO_2/citrate (1/1)_30c(12min) (B), ZnO_2/citrate (1/1)_40c(16min) (C), ZnO_2/citrate (5/1)_20c(8min) (D) and ZnO_2/citrate (10/1)_20c(8min) (E).*

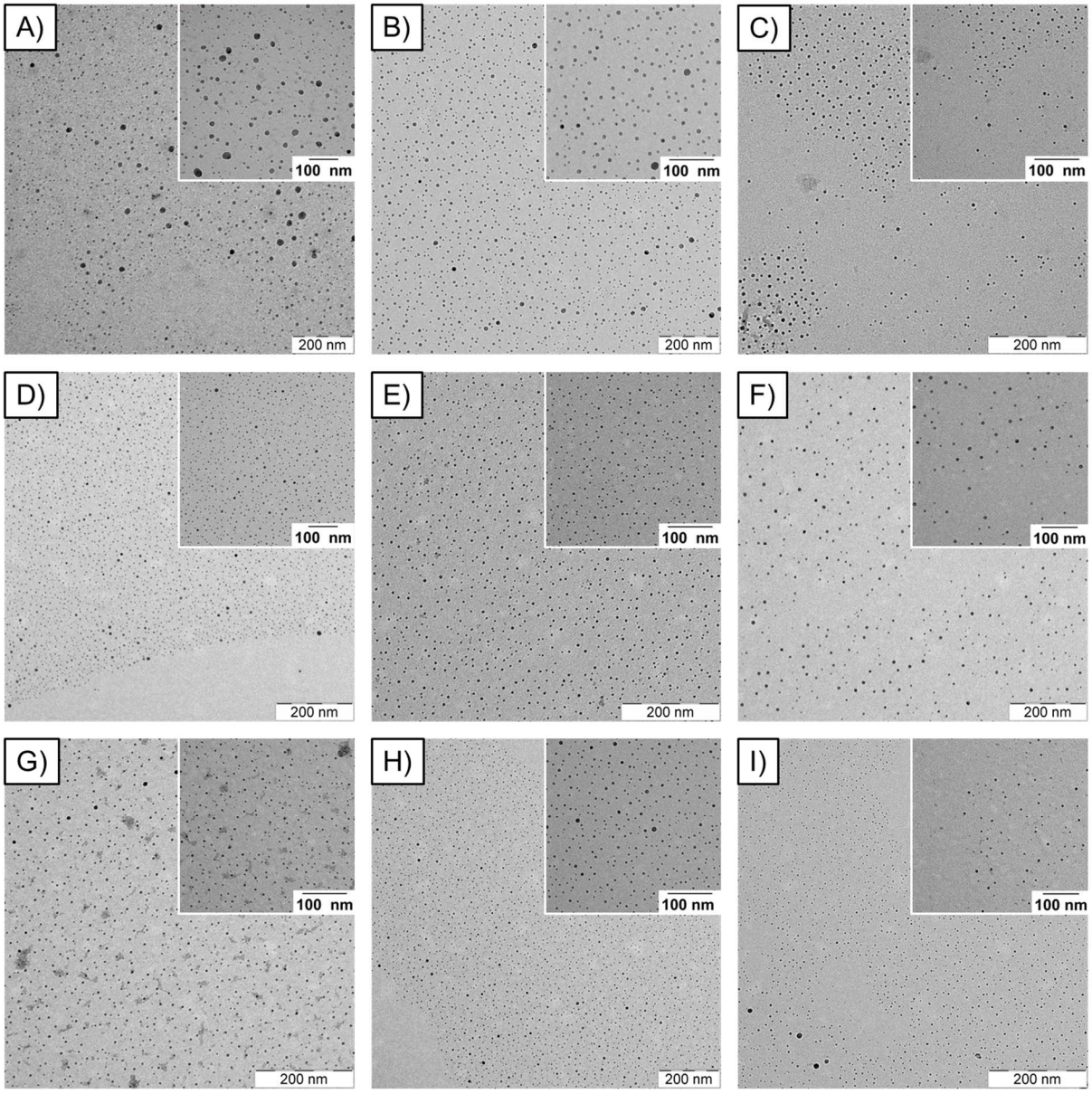

Figure 7.11: *TEM images of the different ZnO_2/Glc-1P samples: A) ZnO_2/Glc-1P (1/1)_10c(4min), B) ZnO_2/Glc-1P (1/1)_20c(8min), C) ZnO_2/Glc-1P (1/1)_30c(12min), D) ZnO_2/Glc-1P (1/1)_40c(16min), E) ZnO_2/Glc-1P (2/1)_30c(12min), F) ZnO_2/Glc-1P (4/1)_30c(12min), G) ZnO_2/Glc-1P (6/1)_30c(12min), H) ZnO_2/Glc-1P (8/1)_30c(12min), I) ZnO_2/Glc-1P (10/1)_30c(12min).*

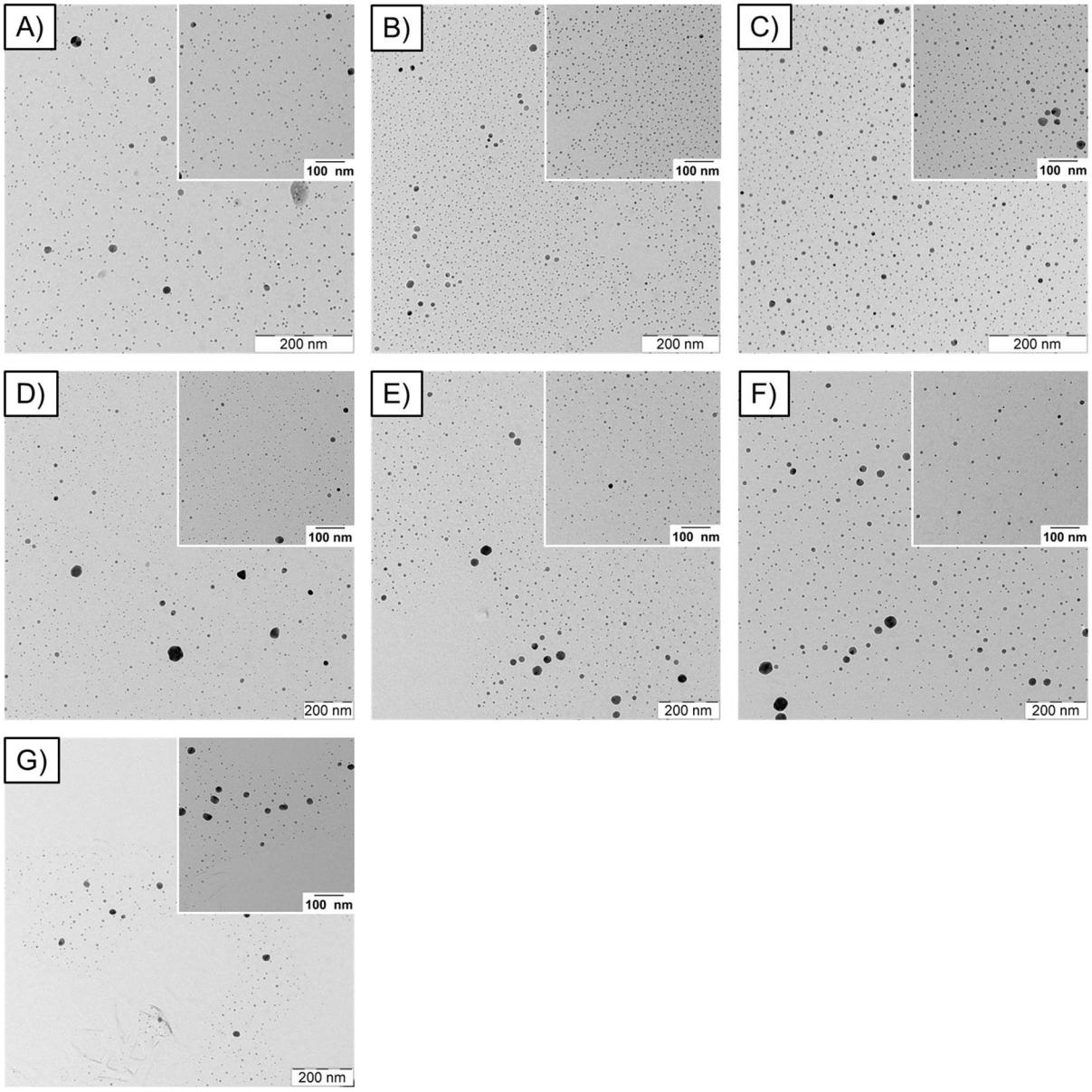

Figure 7.12: *TEM images for the different zinc peroxide nanoparticle samples stabilized with UDP-Glc: ZnO_2/UDP-Glc (1/1)_4min (A), ZnO_2/UDP-Glc (2/1)_4min (B), ZnO_2/UDP-Glc (4/1)_4min (C), ZnO_2/UDP-Glc (6/1)_4min (D), ZnO_2/UDP-Glc (8/1)_4min (E), ZnO_2/UDP-Glc (10/1)_4min (F) and ZnO_2/UDP-Glc (8/1)_3min (G).*

8 References

1 E. Riedel and C. Janiak, *Anorganische Chemie*, Walter De Gruyter GmbH & Co. KG, Berlin/New York, 2011.

2 J. V. Alemán, A. V Chadwick, J. He, M. Hess, K. Horie, R. G. Jones, P. Kratochvíl, I. Meisel, I. Mita, G. Moad, S. Penczek and R. F. T. Stepto, *Pure Appl. Chem.*, 2007, **79**, 1801–1829.

3 A. Gazso and J. Haslinger, *Nano Risiko Governance: Der Gesellschaftliche Umgang Mit Nanotechnologien*, Springer-Verlag, Wien, 2014.

4 80004-2:2015-01 DIN ISO/TS, *Nanotechnologies - Vocabulary - Part 2: Nano-objects*, (ISO/TC 229), 2015.

5 A. Dowling, R. Clift, N. Grobert, D. Hutton, R. Oliver and O. O'Neill, in *London R. Soc. R. Acad. Eng. Rep.*, 2004, pp. 618–618.

6 F. Piccinno, F. Gottschalk, S. Seeger and B. Nowack, *J. Nanoparticle Res.*, 2012, **14**, 1109–1120.

7 A. D. Maynard, in *Woodrow Wilson Int. Cent. Sch.*, 2006, p. 43.

8 P. Shapira and J. Youtie, in *International Symposium on Assessing the Economic Impact of Nanotechnology*, 2012.

9 D. E. Meyer, M. A. Curran and M. A. Gonzalez, *Environ. Sci. Technol.*, 2009, **43**, 1256–1263.

10 P. Buffat and J. P. Borel, *Phys. Rev. A*, 1976, **13**, 2287–2298.

11 A. Rössler, G. Skillas and So. E. Pratsinis, *Chemie unserer Zeit*, 2001, **2001**, 32–41.

12 D. I. Bleiwas, *Potential for Recovery of Cerium Contained in Automotive Catalytic Converters*, 2013.

13 R. Dittmeyer, G. Kreysa and A. Oberholz, *Prozesse und Produkte*, Wiley-VCH, Weinheim, 2004.

14 G. Schmid, A. Eychmüller, U. Banin, S. Dehnen, A. Eichhöfer, J. F. Corrigan and D. Fenske, *Nanoparticles: From Theory to Application*, Wiley-VCH, Weinheim, 2010.

15 M. F. Beckmann, B. S. Gutrath, A. Buchkremer, T. Eckert, J. Timper, A. Leifert, W. Richtering, U. Simon and G. Schmitz, in *2012 IEEE Int. Ultrason. Symp*, 2012, pp. 2336–2339.

16 R. W. Siegel and G. E. Fougere, *Nanostructured Mater.*, 1995, **6**, 205–216.

17 A. Elmarakbi, *Advanced Composite Materials for Automotive Applications: Structural Integrity and Crashworthiness*, John Wiley & Sons, Ltd., New Jersey, 2014.

18 S. Odenbach, *Phys. unserer Zeit*, 2001, **32**, 122–127.

19 S. Breitung-Faes and A. Kwade, *Chemie-Ingenieur-Technik*, 2007, **79**, 241–248.

20 C. Raab, M. Simkó, U. Fiedeler, M. Nentwich and A. Gazso, *Nano Trust Dossiers*, 2008, **6**, 1–4.

21 H. Goesmann and C. Feldmann, *Angew. Chemie*, 2010, **122**, 1402–1437.

22 Y. Xiong and S. E. Pratsinis, *J. Aerosol Sci.*, 1991, **22**, 637–655.

23 M. Köhler, in *Chemische Technik: Prozesse und Produkte*, WILEY-VCH Verlag GmbH & Co. KGaA, Weinheim, 2004, pp. 821–905.

24 D. P. Dufaux and R. L. Axelbaum, *Combust. Flame*, 1995, **100**, 350–358.

25 H. Weller, *Angew. Chemie Int. Ed. English*, 1993, **32**, 41–53.

26 E. Matijević, *J. Eur. Ceram. Soc.*, 1998, **18**, 1357–1364.

27 J. Livage, M. Henry and C. Sanchez, *Prog. Solid State Chem.*, 1988, **18**, 259–341.

28 J. C. Brinker and G. Scherer, *Sol-Gel Science: The Physics and Chemistry of Sol-Gel Processing*, Academic Pree: Boston, Boston, 1998.

29 L. C. Klein, *Sol-Gel Technology for Thin Films, Fibers, Preforms, Electronics, and Specialty Shapes*, Noyes Publications, Park Ridge, 1988.

30 H. Böttcher, C. Jagota, J. Trepte, K. H. Kallies and H. Haufe, *J. Control. Release*, 1999, **60**, 57–65.

31 A. S. Edelstein and R. C. Cammarata, *Nanomaterials: Synthesis, Properties and Applications*, Institute of Physics Publishing, Bristol, 1996.

32 A. Mersmann, *Crystallization Technology Handbook*, Marcel Dekker, New York, 1995.

33 T. Günther, Otto-von-Guericke-Universität Magdeburg, 2008.

34 E. Matijevic, *Chem. Mater.*, 1993, **5**, 412–426.

35 M. Elimelech, *Particle Deposition and Aggregation*, Butterworth- Heinemann, Oxford, 1995.

36 G. Lagaly, O. Schulz and R. Zimehl, *Dispersionen und Emulsionen*, Steinkopf Verlag, Darmstadt, 1997.

37 S. Bhattacharjee, M. Elimelech and M. Borkovec, *Croat. Chem. Acta*, 1998, **71**, 883–903.

38 J. N. Israelachvili, *Intermolecular and Surface Forces*, Academic Press, London, 1992.

39 B. Müller and U. Poth, *Coatings Formulation*, Vincentz Network GmbH & Co.KG, Hannover, 2006.

40 M.-A. Neouze and U. Schubert, *Monatshefte für Chemie - Chem. Mon.*, 2008, **139**, 183–195.

41 N. Adden, L. Gamble, D. Castner, A. Hoffmann, G. Gross and H. Menzel, *Langmuir*, 2006, **22**, 8197–8204.

42 G. P. Holland, R. Sharma, J. O. Agola, S. Amin, V. C. Solomon, P. Singh, D. a. Buttry and J. L. Yarger, *Chem. Mater.*, 2007, **19**, 2519–2526.

43 K. T. Wang, I. Iliopoulos and R. Audebert, *Polym. Bull.*, 1988, **20**, 577–582.

44 X. Wu, H. Liu, J. Liu, K. N. Haley, J. a Treadway, J. P. Larson, N. Ge, F. Peale and M. P. Bruchez, *Nat. Biotechnol.*, 2003, **21**, 41–46.

45 A. Pich, F. Zhang, L. Shen, S. Berger, O. Ornatsky, V. Baranov and M. a Winnik, *Small*, 2008, **4**, 2171–5.

46 H. Bai and X. Liu, *Mater. Lett.*, 2010, **64**, 341–343.

47 M. a. Gondal, Q. a. Drmosh, Z. H. Yamani and T. a. Saleh, *Appl. Surf. Sci.*, 2009, **256**, 298–304.

48 M. Sun, W. Hao, C. Wang and T. Wang, *Chem. Phys. Lett.*, 2007, **443**, 342–346.

49 W. Chen, Y. H. Lu, M. Wang, L. Kroner, H. Paul, H. Fecht, J. Bednarcik, K. Stahl, Z. L. Zhang, U. Wiedwald, U. Kaiser, P. Ziemann, T. Kikegawa, O. C. D. Wu and J. Z. Jiang, *J. Phys. Chem. C*, 2009, **113**, 1320–1324.

50 L. Rosenthal-Toib, K. Zohar, M. Alagem and Y. Tsur, *Chem. Eng. J.*, 2008, **136**, 425–429.

51 L. Y. Yang, G. P. Feng and T. X. Wang, *Mater. Lett.*, 2010, **64**, 1647–1649.

52 T. M. Squires, *Rev. Mod. Phys.*, 2005, **77**, 977–1026.

53 C. Bergs, P. Simon, Y. Prots and A. Pich, *RSC Adv.*, 2016, **6**, 84777–84786.

54 *JCPDS card no. 13-0311.*, .

55 N. Uekawa, N. Mochizuki, J. Kajiwara, F. Mori, Y. J. Wu and K. Kakegawa, *Phys. Chem. Chem. Phys.*, 2003, **5**, 929–934.

56 X. Han, R. Liu, W. Chen and Z. Xu, *Thin Solid Films*, 2008, **516**, 4025–4029.

57 S. Cheng, D. Yan, J. T. Chen, R. F. Zhuo, J. J. Feng, H. J. Li, H. T. Feng and P. X. Yan, *J. Phys. Chem. C*, 2009, **113**, 13630–13635.

58 D. Sebők, T. Szabó and I. Dékány, *Appl. Surf. Sci.*, 2009, **255**, 6953–6962.

59 Y. Wolanov, P. V Prikhodchenko, A. G. Medvedev, R. Pedahzur and O. Lev, *Environ. Sci. Technol.*, 2013, **47 (15)**, 8769–8774.

60 E. H. Bawn, *Catalytic decomposition of hydrogen peroxide on differnt metals.*, 1935.

61 R. Colonia, J. L. Solís and M. Gómez, *Adv. Nat. Sci. Nanosci. Nanotechnol.*, 2014, **5**, 15008.

62 A. Escobedo-Morales, R. Esparza, A. García-Ruiz, A. Aguilar, E. Rubio-Rosas and R. Pérez, *J. Cryst. Growth*, 2011, **316**, 37–41.

63 A. Eisenberg, *Mucromolecules*, 1970, **3**, 147–154.

64 H. P. Brown, *Rubber Chem. Technol.*, 1963, **36**, 931–962.

65 C.-C. Hsu and N. L. Wu, *J. Photochem. Photobiol. A Chem.*, 2005, **172**, 269–274.

66 A. L. Linsebigler, A. L. Linsebigler, J. T. Yates Jr, G. Lu, G. Lu and J. T. Yates, *Chem. Rev.*, 1995, **95**, 735–758.

67 M. P. Doyle and V. Bagheri, *J. Org. Chem.*, 1981, **46**, 4806–4808.

68 F. M. Menger and C. Lee, *Tetrahedron Lett.*, 1981, **22**, 1655–1656.

69 C. K. Lee, B.-S. Koo, Y. S. Lee, H. K. Cho and K.-J. Lee, *Bull. Korean Chem. Soc.*, 2002, **23**, 1667–1670.

70 G. Cainelli and G. Cardillo, *Chromium Oxidants in Organic Chemistry*, Springer, Berlin, 1984.

71 H. B. Ji, K. Ebitani, T. Mizugaki and K. Kaneda, *Catal. Commun.*, 2002, **3**, 511–517.

72 K. Yamaguchi and N. Mizuno, *Angew. Chemie - Int. Ed.*, 2002, **41**, 4538–4542.

73 B. Zhan, M. A. White, T. Sham, J. A. Pincock, J. Doucet, K. V. R. Rao, K. N. Robertson, T. S. Cameron, M. Ii and C. Phen, *J. AM. CHEM. SOC.*, 2003, **125**, 2195–2199.

74 V. R. Choudhary, A. Dhar, P. Jana, R. Jha and B. S. Uphade, *Green Chem.*, 2005, **7**, 768.

75 S. Verma and S. L. Jain, *Inorg. Chem. Front.*, 2014, **1**, 534.

76 J. Kimling, M. Maier, B. Okenve, V. Kotaidis, H. Ballot and A. Plech, *J. Phys. Chem. B*, 2006, **110**, 15700–15707.

77 S. Christau, T. Möller, Z. Yenice, J. Genzer and R. Von Klitzing, *Langmuir*, 2014, **30**, 13033–13041.

78 P. M. Aneesh, K. A. Vanaja and M. K. Jayaraj, *Nanophotonic Mater. IV*, 2007, **6639**, 66390J.

79 C. Suryanarayana and M. G. Norton, *X-Ray Diffraction a Practical Approach*, Plenum Press, New York, 1998.

80 J. Gao, Y. Wang and H. Hao, *Front. Chem. Sci. Eng.*, 2012, **6**, 276.

81 V. . Fassel, *Science*, 1978, **202**, 183–191.

82 R. Kilaas, *J. Microsc.*, 1998, **190**, 45–51.

83 M. Rafailovich, J. Sokolov and A. Gedanken, *Langmuir*, 1999, **15**, 7111–7115.

84 P. Kim, S. C. Jones, P. J. Hotchkiss, J. N. Haddock, B. Kippelen, S. R. Marder and J. W. Perry, *Adv. Mater.*, 2007, **19**, 1001–1005.

85 J. Piella, N. G. Bastús and V. Puntes, *Chem. Mater.*, 2016, **28**, 1066–1075.

86 M. Rani, L. Moudgil, B. Singh, A. Kaushal, A. Mittal, G. S. S. Saini, S. K. Tripathi, G. Singh and A. Kaura, *RSC Adv.*, 2016, **6**, 17373–17383.

87 N. G. Bastús, J. Comenge and V. Puntes, *Langmuir*, 2011, **27**, 11098–11105.

88 S. Liufu, H. Xiao and Y. Li, *Powder Technol.*, 2004, **145**, 20–24.

89 S. C. Lee, H. W. Choi, H. J. Lee, K. J. Kim, J. H. Chang, S. Y. Kim, J. Choi, K.-S. Oh and Y.-K. Jeong, *J. Mater. Chem.*, 2007, **17**, 174–180.

90 D. R. Lide, *CRC Handbook of Chemistry and Physics*, CRC, Boca Raton, 1994.

91 Y. Du, M.-S. Zhang, J. Hong, Y. Shen, Q. Chen and Z. Yin, *Appl. Phys. A Mater. Sci. Process.*, 2003, **76**, 171–176.

92 R. F. Weiss, *Deep Sea Res. Oceanogr. Abstr.*, 1970, **17**, 721–735.

93 A. Bumajdad, J. Eastoe, M. I. Zaki, R. K. Heenan and L. Pasupulety, *J. Colloid Interface Sci.*, 2007, **312**, 68–75.

94 A. Bumajdad, M. I. Zaki, J. Eastoe and L. Pasupulety, *Langmuir*, 2004, **20**, 11223–33.

95 J. Cason, M. Miller, J. Thomson and C. B. Roberts, *J. Phys. Chem. B*, 2001, **105**, 2297–2302.

96 M. Maillard, S. Giorgio and M. P. Pileni, *J. Phys. Chem. B*, 2003, **107**, 2466–2470.

97 E. Odella, R. D. Falcone, J. J. Silber and N. M. Correa, *Phys. Chem. Chem. Phys.*, 2014, **16**, 15457–15468.

98 G. Zhou, G. Li and W. Chen, *Langmuir*, 2002, **18**, 4566–4571.

99 G. Onori and A. Santucci, *J. Phys. Chem.*, 1993, **97**, 5430–5434.

100 T. Thorstenson and M. Urban, *J. Appl. Polym. Sci.*, 1993, **47**, 1381–1386.

101 W. Bascom and Singleterry, *J. Phys. Chem.*, 1961, **65**, 1683–1689.

102 K. Pal, F. Chandra, S. Mallick and A. L. Koner, *New J. Chem.*, 2016, **40**, 6093–6100.

103 I. Damjanov, *Lab Invest*, 1987, **57**, 5–20.

104 Irwin J. Goldtein and R. D. Poretzt, *The Lectins: Properties, Functions, and Applications in Biology and Medicine*, 1986.

105 R. Schauer, C. Fischer, H. Lee, B.Ruch and S. Kelm, *Lectins and Glycoconjugates in Oncology*, 1988.

106 B. K. Brandley and R. L. Schnaar, *J. Leukoc. Biol.*, 1986, **40**, 97–111.

107 F. L. Harrison and C. J. Chesterton, *FEBS Lett.*, 1980, **122**, 157–165.

108 R. Mody, S. H. antaram Joshi and W. Chaney, *J. Pharmacol. Toxicol. Methods*, 1995, **33**, 1–10.

109 H. Lis and N. Sharon, *Annu. Rev. Biochem.*, 1986, **55**, 35–67.

110 K. Hardman and C. Ainsworth, *Biochemistry*, 1972, **11**, 4910–4919.

111 G. Reeke, J. Becker and G. Edelman, *J. Biol. Chem.*, 1975, **250**, 1525–1547.

112 J. L. Wang, B. a Cunningham and G. M. Edelman, *Proc. Natl. Acad. Sci. U. S. A.*, 1971, **68**, 1130–1134.

113 B. B. L. Agrawal and Irwin J. Goldtein, *Biochim. Biophys. Acta*, 1967, **147**, 262–271.

114 T. Li, H. B. Lee and K. Park, *J. Biomater. Sci. Polym. Ed.*, 1998, **9**, 327–344.

115 M. R. Duff, W. S. Fyvie, S. D. Markad, A. E. Frankel, C. V Kumar, J. a Gascón and M. W. Peczuh, *Org. Biomol. Chem.*, 2011, **9**, 154–164.

116 H. J. Gabius, S. André, J. Jiménez-Barbero, A. Romero and D. Solís, *Trends Biochem. Sci.*, 2011, **36**, 298–313.

117 C. Kamerke, M. Pattky, C. Huhn and L. Elling, *J. Mol. Catal. B Enzym.*, 2012, **79**, 27–34.

118 S. A. Sajadi, B. Song, F. Gregán and H. Sigel, *Inorg. Chem.*, 1999, **38**, 439–448.

119 W. Gao, L. Dickinson, C. Grozinger, F. G. Morin and L. Reven, *Langmuir*, 1996, **12**, 6429–6435.

120 W. Gao, L. Dickinson, C. Grozinger, F. F. G. Morin and L. Reven, *Langmuir*, 1997, **13**, 115–118.

121 J. P. Osegovic and R. S. Drago, *J. Phys. Chem. B*, 2000, **104**, 147–154.

122 G. M. Cook, *J. Cell Sci.*, 1986, **4**, 45–70.

123 N. Sharon and H. Lis, *Science (80-.)*., 1989, **246**, 227–234.

124 A. Salvati, C. Åberg, K. A. Dawson and M. P. Monopoli, *Nat. Nanotechnol.*, 2012, **7**, 779–786.

125 C. C. Lin, Y. C. Yeh, C. Y. Yang, G. F. Chen, Y. C. Chen, Y. C. Wu and C. C. Chen, *Chem. Commun.*, 2003, **9**, 2920–2921.

126 P. Rouge and B. Sousa-Cavada, *Plant Sci. Lett.*, 1984, **37**, 21–27.

127 R. D. Poretzt and I. J. Goldstein, *Biochemistry*, 1970, **9**, 2890–2896.

128 N. M. Oosterhuis and N. W. Kossen, *Biotechnol. Bioeng.*, 1984, **26**, 546–550.

129 J. O. Konz, J. King and C. L. Cooney, *Biotechnol. Prog.*, 1998, **14**, 393–409.

130 K. V. & O. R. B. Daniel E. Boehme, *Nature*, 1976, **262**, 418–420.

131 E. M. Gregory and I. Fridovich, *J. Bacteriol.*, 1973, **114**, 543–548.

132 E. M. Gregory, S. A. Goscin and I. Fridovich, *J. BACTEIOLOGY*, 1974, **117**, 456–460.

133 J. B. Harley, G. M. Santangelo, H. Rasmussen and H. Goldfine, *J. Bacteriol.*, 1978, **134**, 808–820.

134 A. Castan, A. Näsman and S.-O. Enfors, *Enzyme Microb. Technol.*, 2002, **30**, 847–854.

135 H. J. Johan J.P. Gille, Heleen M. Wortelboer, *Free Radic. Biol. Med.*, 1988, **4**, 85–91.

136 A. A. Lin and W. M. Millerh, *Ann. New York Acad. Sci.*, 1992, **665**, 117–126.

137 G. R. Marco A. Caccuittolo, Loc Trinh, Janice A. Lumpkin, *Free Radic. Biol. Med.*, 1993, **14**, 267–276.

138 B. Levine and N. Mizushima, *Nature*, 2011, **469**, 323–335.

139 Z. Li, Y. Yang, M. Ming and B. Liu, *Biochem. Biophys. Res. Commun.*, 2011, **414**, 5–8.

140 N. R. Love, Y. Chen, S. Ishibashi, P. Kritsiligkou, R. Lea, Y. Koh, J. L. Gallop, K. Dorey and E. Amaya, *Nat. Cell Biol.*, 2013, **15**, 222–228.

141 E. Merki, M. Zamora, A. Raya, Y. Kawakami, J. Wang, X. Zhang, J. Burch, S. W. Kubalak, P. Kaliman, J. C. Izpisua Belmonte, K. R. Chien and P. Ruiz-Lozano, *Proc. Natl. Acad. Sci. U. S. A.*, 2005, **102**, 18455–60.

142 T. Brade, S. Kumar, T. J. Cunningham, C. Chatzi, X. Zhao, S. Cavallero, P. Li, H. M. Sucov, P. Ruiz-Lozano and G. Duester, *Development*, 2011, **138**, 139–148.

143 K. Loh, H. Deng, A. Fukushima, X. Cai, B. Boivin, C. Bruce, B. J. Shields, B. Skiba, L. M. Ooms, N. Stepto, B. Wu, C. a Mitchell, N. K. Tonks, M. J. Watt, M. a Febbraio, P. J. Crack, S. Andrikopoulos and T. Tiganis, *Cell Metab.*, 2009, **10**, 260–272.

144 D. E. Morgenstern, M. a Gifford, L. L. Li, C. M. Doerschuk and M. C. Dinauer, *J. Exp.*

Med., 1997, **185**, 207–218.

145 J. D. Lambeth, *Nat. Rev. Immunol.*, 2004, **4**, 181–189.

146 A. Kanayama and Y. Miyamoto, *J. Leukoc. Biol.*, 2007, **82**, 1344–1352.

147 L. A. MacMillan-Crow, J. P. Crow and J. A. Thompson, *Biochemistry*, 1998, **37**, 1613–1622.

148 A. Baez and J. Shiloach, *Microb. Cell Fact.*, 2014, **13**, 181.

149 J. A. Imlay, *Nat.Rev.Microbiol.*, 2013, **11**, 443–454.

150 J. A. Imlay, *Annu.Rev.Biochem.*, 2008, **77**, 755–776.

151 C. A. McDonald, R. L. Fagan, F. Collard, V. M. Monnier and B. A. Palfey, *J. Am. Chem. Soc.*, 2011, **133**, 16809–16811.

152 J. F. Turrens, *J Physiol*, 2003, **522.2**, 335–344.

153 Y. Liu, G. Fiskum and D. Schubert, *J Neurochem*, 2002, **80**, 780–787.

154 M. D. Brand, *Exp. Gerontol.*, 2010, **45**, 466–472.

155 F. L. Muller, Y. Liu and H. Van Remmen, 2004, **279**, 49064–49073.

156 K. H. Muhvich, M. K. Park, R. A. M. Myers and L. Marzella, *Antimicrob. Agents Chemother.*, 1989, **33**, 1526–1530.

157 J. T. Mader, G. L. Brown, J. C. Guckian, C. H. Wells and J. A. Reinarz, *J. Infect Dis.*, 1980, **142**, 915–922.

158 T. K. Hunt, M. Linsey, H. Grislis, M. Sonne and E. Jawetz, *Ann. Surg.*, 1975, **181**, 35–39.

159 D. R. Knighton, B. Halliday and T. K. Hunt, *Arch Surg.*, 1986, **121**, 191–195.

160 D. R. Knighton, V. D. Fiegel, T. Halverson, S. Schneider, T. Brown and C. L. Wells, *Arch Surg.*, 1990, **125**, 97–100.

161 M. Cimşit, G. Uzun and S. Yildiz, *Expert Rev. Anti. Infect. Ther.*, 2009, **7**, 1015–1026.

162 M. K. Park, K. H. Muhvich, R. A. M. Myers and L. Marzella, *Hyperbaric Medicine Practice*, Whelan HT (Eds). Best Publishing, Flagstaff, 2004.

163 D. O. O. & L. J. V. P. Jessica M. A. Blair, Mark A. Webber, Alison J. Baylay, *Nat. Rev. Microbiol.*, 2015, **13**, 42–51.

164 E. Marti, E. Variatza and J. L. Balcazar, *Trends Microbiol.*, 2014, **22**, 36–41.

165 M. N. Alekshun and S. B. Levy, *Cell*, 2007, **128**, 1037–1050.

166 A. Giedraitienė, A. Vitkauskienė, R. Naginienė and A. Pavilonis, *Medicina (Kaunas).*, 2011, **47**, 137–46.

167 L. Fernandez and E. W. Hancock, *Clin. Microbiol. Rev.*, 2012, **25**, 661–681.

168 L. J. V Piddock, *Clin. Microbiol. Rev.*, 2006, **19**, 382–402.

169 G. De Pascale and G. D. Wright, *ChemBioChem*, 2010, **11**, 1325–1334.

170 S. Dzidic, J. Suskovic and B. Kos, *Food Technol. Biotechnol.*, 2008, **46**, 11–21.

171 R. M. Donlan, *Emerg. Infect. Dis.*, 2002, **8**, 881–890.

172 K. . Lewis, *Antimicrob. Agents Chemother.*, 2001, **45**, 999–1007.

173 R. M. Donlan and J. W. Costerton, *Clin.Microbiol. Rev.*, 2002, **15**, 167–19.

174 R. Patel, *Clin Orthop Relat Res.*, 2005, **437**, 41–47.

175 W. M. Dunne, *Clin. Microbiol. Rev.*, 2002, **15**, 155–166.

176 K. Driffield, K. Miller, J. M. Bostock, A. J. O'neill and I. Chopra, *J. Antimicrob. Chemother.*, 2008, **61**, 1053–1056.

177 S. Molin and T. Tolker-Nielsen, *Curr. Opin. Biotechnol.*, 2003, **14**, 255–261.

178 B. M. Peters, M. E. Shirtliff and M. A. Jabra-Rizk, *PLoS Pathog.*, 2010, **6**, 4–7.

179 L. Good, *Methods Mol Biol.*, 2002, **208**, 237–248.

180 N. K. Sahu, G. Shilakari, A. Nayak and D. V. Kohli, *Curr Pharm Biotechnol.*, 2007, **8**, 291–304.

181 P. Gilbert and L. E. Moore, *J. Appl. Microbiol.*, 2005, **99**, 703–715.

182 M. Kather, M. Skischus, P. Kandt, A. Pich, G. Conrads and S. Neuss, *Angew. Chemie Int. Ed.*, 2017, **56**, 1–7.

183 B. Ramalingam, T. Parandhaman and S. K. Das, *ACS Appl. Mater. Interfaces*, 2016, **8**, 4963–4976.

184 L. Rizzello and P. P. Pompa, *Chem. Soc. Rev.*, 2014, **43**, 1501–1518.

185 S. Chernousova and M. Epple, *Angew. Chemie - Int. Ed.*, 2013, **52**, 1636–1653.

186 O. Bondarenko, A. Ivask, A. Käkinen, I. Kurvet and A. Kahru, *PLoS One*, 2013, **8**.

187 W. R. Li, X. B. Xie, Q. S. Shi, H. Y. Zeng, Y. S. Ou-Yang and Y. Ben Chen, *Appl. Microbiol. Biotechnol.*, 2010, **85**, 1115–1122.

188 E. Amato, Y. a Diaz-Fernandez, A. Taglietti, P. Pallavicini, L. Pasotti, L. Cucca, C. Milanese, P. Grisoli, C. Dacarro, J. M. Fernandez-Hechavarria and V. Necchi, *Langmuir*, 2011, **27**, 9165–9173.

189 C. Carlson, S. M. Hussein, A. M. Schrand, L. K. Braydich-Stolle, K. L. Hess, R. L. Jones and J. J. Schlager, *J. Phys. Chem. B*, 2008, **112**, 13608–13619.

190 T. Tian, X. Shi, L. Cheng, Y. Luo, Z. Dong, H. Gong, L. Xu, Z. Zhong, R. Peng and Z. Liu, *ACS Appl. Mater. Interfaces*, 2014, **6**, 8542–8548.

191 J. Tang, Q. Chen, L. Xu, S. Zhang, L. Feng, L. Cheng, H. Xu and Z. Liu, *ACS Appl. Mater. Interfaces*, 2013, **5**, 3867–3874.

192 W.-P. Xu, L.-C. Zhang, J.-P. Li, Y. Lu, H.-H. Li, Y.-N. Ma, W.-D. Wang and S.-H. Yu, *J. Mater. Chem.*, 2011, **21**, 4593.

193 X. Shi, H. Gong, Y. Li, C. Wang, L. Cheng and Z. Liu, *Biomaterials*, 2013, **34**, 4786–4793.

194 K. Yang, L. Hu, X. Ma, S. Ye, L. Cheng, X. Shi, C. Li, Y. Li and Z. Liu, *Adv. Mater.*,

2012, **24**, 1868–1872.

195 K. Yang, S. Zhang, G. Zhang, X. Sun, S. T. Lee and Z. Liu, *Nano Lett.*, 2010, **10**, 3318–3323.

196 L. Zhang, Y. Jiang, Y. Ding, M. Povey and D. York, *J. Nanoparticle Res.*, 2007, **9**, 479–489.

197 X. Peng, S. Palma, N. S. Fisher and S. S. Wong, *Aquat. Toxicol.*, 2011, **102**, 186–196.

198 N. Padmavathy and R. Vijayaraghavan, *Sci. Technol. Adv. Mater.*, 2008, **9**, 35004.

199 N. Hao, K. W. Jayawardana, X. Chen and M. Yan, *ACS Appl. Mater. Interfaces*, 2015, **7**, 1040–1045.

200 D. L. Clemens, B. Y. Lee, M. Xue, C. R. Thomas, H. Meng, D. Ferris, A. E. Nel, J. I. Zink and M. A. Horwitz, *Antimicrob. Agents Chemother.*, 2012, **56**, 2535–2545.

201 J. S. Dickson, M. Koohmaraie and R. L. Hruska, *Appl. Environ. Microbiol.*, 1989, **55**, 832–836.

202 T. Chilton, S. Burnley and S. Nesaratnam, *Resour. Conserv. Recy.*, 2010, **54**, 1241.

203 C. Lorenzetti, P. Manaresi, C. Berti and G. Barbiroli, *J. Polym. Environ.*, 2006, **14**, 89–101.

204 D. Paszun and T. Spychaj, *Ind. Eng. Chem. Res.*, 1997, **36**, 1373–1382.

205 T. Spychaj, *Handbook of Thermoplastic Polyesters: Homopolymers, Copolymers, Blends, and Composites*, Wiley-VCH, Weinheim, 2002.

206 V. Sinha, M. R. Patel and J. V. Patel, *J. Polym. Env.*, 2008, **18**, 8.

207 S. N. Vouyiouka, E. K. Karakatsani and C. D. Papaspyrides, *Prog. Polym. Sci.*, 2005, **30**, 10–37.

208 F. Awaja and D. Pavel, *Eur. Polym. J.*, 2005, **41**, 1453.

209 C. Scheirs and G. Camino, *Effect of Contamination on the Recycling of Polymers, in: Recycling of PVC & Mixed Plastic Waste,* F. P. La Mantia, Palermo, 1996.

210 S. M. Aharoni, *Polym. Eng. Sci.*, 1998, **38**, 1039–1047.

211 J. Scheirs and T. E. Long, *Modern Polyesters: Chemistry and Technology of Polyesters and Copolyesters*, John Wiley & Sons Ltd, Chichester, 2005.

212 D. Berg, K. Schäfer, A. Korner, R. Kaufmann, W. Tillmann and M. Möller, *Macromol. Mater. Eng.*, 2016, **301**, 1454–1467.

213 Y. Yang, S. Yoon, Y. Hwang and B. Song, *Bull. Korean Chem. Soc.*, 2012, **33**, 3445–3447.

214 U. K. Thiele, *Chem. Fibers Int.*, 2004, **54**, 162.

215 F. Ahmadnian, F. Velasquez and K.-H. Reichert, *Macromol. React. Eng.*, 2008, **2**, 513.

216 G. Angerer, L. Erdmann, F. Marscheider-Weidemann, M. Scharp, A. Lüllman, V. Handke and M. Marwede, *Einfluss des branchenspezifischen Rohstoffbedarfs in rohstoffintensiven Zukunftstechnologien auf die zukünftige Rohstoffnachfrage,* Karlsruhe, 2009.

217 J. S. Chung, *J. Macromol. Sci. Chem*, 1990, **A27**, 479–490.

218 U. K. Thiele, *Int. J. Polym. Mater.*, 2001, **50**, 387.

219 R. Stevenson and H. Nettleton, *J. Polym. Sci.*, 1986, **6**, 889–900.

220 R. W. Stevenson, *J. Polym. Sci.*, 1969, **7**, 395–407.

221 U. K. Thiele, *Polyester Bottle Resins, Production, Processing, Properties and Recycling*, PETplanet Publisher GmbH, Heidelberg, 2007.

222 S. B. Maerov, *J. Polym. Sci. Polym. Chem. Ed.*, 1979, **17**, 4033–4040.

223 B. Duh, *Polymer (Guildf).*, 2002, **43**, 3147–3154.

224 P. M and F. P. La Mantia, *Polym. Degrad. Stabil.*, 1999, **63**, 11.

225 B. G. Ranby and J. F. Rabek, *Photodegradation, photo-oxidation, and photostabilization of polymers*, John Wiley & Sons Ltd, London, 1975.

226 M. Edge, N. S. Allen, R. Wiles, W. McDonald and S. V. Mortlock, *Polymer (Guildf).*, 1995, **36**, 227–234.

227 R. Pelton and T. Hoare, in *Microgel Suspensions: Fundamentals and Applications*, WILEY-VCH Verlag GmbH & Co. KGaA, 2011.

228 R. Pelton, *Adv. Colloid Interface Sci.*, 2000, **85**, 1–33.

229 M. A. Cohen Stuart, *Colloid Polym. Sci.*, 2008, **286**, 855–864.

230 W. Richtering, I. Berndt and J. S. Pedersen, in *Microgel Suspensions: Fundamentals and Applications*, WILEY-VCH Verlag GmbH & Co. KGaA, 2011.

231 M. Stieger, W. Richtering, J. S. Pedersen and P. Lindner, *J. Chem. Phys.,* 2004, **120**, 6197.

232 M. Reufer, P. Díaz-Leyva, I. Lynch and F. Scheffold, *Eur. Phys. J. E*, 2009, **28**, 165–171.

233 P. J. Flory and J. Rehner, *J. Chem. Phys.*, 1943, **11**, 521–526.

234 B. R. Saunders, H. M. Crowther and B. Vincent, *Macromolecules*, 1997, **30**, 482–487.

235 H. M. Crowther and B. Vincent, *Colloid Polym. Sci.*, 1998, **276**, 46–51.

236 J. D. Debord and L. A. Lyon, *Langmuir*, 2003, **19**, 7662–7664.

237 J. J. Lietor-Santos, B. Sierra-Martin, R. Vavrin, Z. Hu, U. Gasser and A. Fernandez-Nieves, *Macromolecules*, 2009, **42**, 6225–6230.

238 K. S. Oh and Y. C. Bae, *J. Appl. Polym. Sci.*, 1998, **69**, 109–114.

239 B. Sierra-Martin, J. J. Lietor-Santos, A. Fernandez-Barbero, T. T. Nguyen and A. Fernandez-Nieves, in *Microgel Suspensions: Fundamentals and Applications*, WILEY-VCH Verlag GmbH & Co. KGaA, 2011.

240 C. Wu, S. Zhou, S. C. F. Au-yeung and S. Jiang, *Die Angew. Makromol. Chemie*, 1996, **240**, 123–136.

241 C. Wu, *Polymer (Guildf).*, 1998, **39**, 4609–4619.

242 S. Sun and P. Wu, *J. Phys. Chem. B*, 2011, **115**, 11609–11618.

243 A. Pich, A. Tessier, V. Boyko, Y. Lu and H. J. P. Adler, *Macromolecules*, 2006, **39**, 7701–7707.

244 A. Pich and W. Richtering, *Chemical Design of Responsive Microgels*, Springer-Verlag Berlin Heidelberg, 2010.

245 W. H. Blackburn and L. A. Lyon, *Colloid Polym Sci.*, 2008, **286**, 563–569.

246 G. Agrawal, M. P. Schürings, P. van Rijn and A. Pich, *J. Mater. Chem. A*, 2013, **1**, 13244.

247 S. Ito, K. Ogawa, H. Suzuki, B. Wang, R. Yoshida and E. Kokufuta, *Langmuir*, 1999, **15**, 4289–4294.

248 I. Varga, T. Gilányi, R. Mészáros, G. Filipcsei and M. Zrínyi, *J. Phys. Chem. B*, 2001, **105**, 9071–9076.

249 H. Senff and W. Richtering, *Colloid Polym. Sci.*, 2000, **278**, 830–840.

250 R. H. Pelton and P. Chibante, *Colloids and Surfaces*, 1986, **20**, 247–256.

251 B. R. Saunders, N. Laajam, E. Daly, S. Teow, X. Hu and R. Stepto, *Adv. Colloid Interface Sci.*, 2009, **147**–**148**, 251–262.

252 A. Balaceanu, V. Mayorga, W. Lin, M. P. Schürings, D. E. Demco, A. Böker, M. A. Winnik and A. Pich, *Colloid Polym. Sci.*, 2013, **291**, 21–31.

253 N. A. Cortez-Lemus and A. Licea-Claverie, *Prog. Polym. Sci.*, 2016, **53**, 1–51.

254 J. Ramos, A. Imaz and J. Forcada, *Polym. Chem.*, 2012, **3**, 852–856.

255 J. Ramos, A. Imaz, J. Callejas-Fernández, L. Barbosa-Barros, J. Estelrich, M. Quesada-Pérez and J. Forcada, *Soft Matter*, 2011, **7**, 5067–5082.

256 V. Boyko, A. Pich, Y. Lu, S. Richter, K. F. Arndt and H. J. P. Adler, *Polymer (Guildf).*, 2003, **44**, 7821–7827.

257 G. Aguirre, J. Ramos, J. P. A. Heuts and J. Forcada, *Polym. Chem.*, 2014, **5**, 4569.

258 S. Bhattacharya, F. Eckert, V. Boyko and A. Pich, *Small*, 2007, **3**, 650–657.

259 H. Nur, V. T. Pinkrah, J. C. Mitchell, L. S. Benée and M. J. Snowden, *Adv. Colloid Interface Sci.*, 2010, **158**, 15–20.

260 M. Bradley and B. Vincent, *Langmuir*, 2008, **24**, 2421–2425.

261 W. Ma, Y. Zhang, L. Li, Y. Zhang, M. Yu, J. Guo, H. Lu and C. Wang, *Adv. Funct. Mater.*, 2013, **23**, 107–115.

262 S. Çavuş and E. Çakal, *Ind. Eng. Chem. Res.*, 2012, **51**, 1218–1226.

263 H. Peng, X. Huang, A. Oppermann, A. Melle, L. Weger, M. Karperien, D. Wöll and A. Pich, *J. Mater. Chem. B*, 2016, **4**, 7572–7583.

264 A. Melle, A. Balaceanu, M. Kather and Y. Wu, *J. Mater. Chem. B*, 2016, **4**, 5127–5137.

265 H. Vihola, A. Laukkanen, J. Hirvonen and H. Tenhu, *Eur. J. Pharm. Sci.*, 2002, **16**, 69–74.

266 T. Hoare and R. Pelton, *Langmuir*, 2008, **24**, 1005–1012.

267 P. Liu, Q. Luo, Y. Guan and Y. Zhang, *Polymer (Guildf).*, 2010, **51**, 2668–2675.

268 M. Karg and T. Hellweg, *J. Mater. Chem.*, 2009, **19**, 8714.

269 S. Chai, J. Zhang, T. Yang, J. Yuan and S. Cheng, *Colloids Surfaces A Physicochem. Eng. Asp.*, 2010, **356**, 32–39.

270 Y. Mei, Y. Lu, F. Polzer, M. Ballauff and M. Drechsler, *Chem. Mater.*, 2007, **19**, 1062–1069.

271 M. Agrawal, A. Pich, S. Gupta, N. E. Zafeiropoulos, J. Rubio-Retama, F. Simon and M. Stamm, *J. Mater. Chem.*, 2008, **18**, 2581–2586.

272 R. Fenger, E. Fertitta, H. Kirmse, a. F. Thünemann and K. Rademann, *Phys. Chem. Chem. Phys.*, 2012, **14**, 9343.

273 A. Gangula, R. Podila, R. M, L. Karanam, C. Janardhana and A. M. Rao, *Langmuir*, 2011, **27**, 15268–15274.

274 H. Koga, Y. Umemura and T. Kitaoka, *Catalysts*, 2011, **1**, 69–82.

275 M. J. Vaidya, S. M. Kulkarni and R. V. Chaudhari, *Org. Process Res. Dev.*, 2003, **7**, 202–208.

276 N. Häntzschel, F. Zhang, F. Eckert, A. Pich and M. A. Winnik, *Langmuir*, 2007, **23**, 10793–10800.

277 S. Christau, T. Möller, F. Brose, J. Genzer, O. Soltwedel and R. von Klitzing, *Polym. (United Kingdom)*, 2016, **98**, 454–463.